Advances in the characterization of inorganic solids using NMR correlation experiments

Andrew G. M. Rankin, Frédérique Pourpoint, Nghia Tuan Duong, Laurent Delevoye, Jean-Paul Amoureux, Olivier Lafon

Advances in the characterization of inorganic solids using NMR correlation experiments

Andrew G. M. Rankin[1], Frédérique Pourpoint[2], Nghia Tuan Duong[3], Laurent Delevoye[1], Jean-Paul Amoureux[2,4], Olivier Lafon[2,*]

[1] Univ. Lille, CNRS, INRAE, Centrale Lille, Univ. Artois, FR 2638 – IMEC – Fédération Chevreul, 59000 Lille, France

[2] Univ. Lille, CNRS, Centrale Lille, Univ. Artois, UMR 8181 – UCCS – Unité de Catalyse et Chimie du Solide, 59000 Lille, France.

[3] Aix Marseille Univ, CNRS, ICR, 13397 Marseille, France.

[4] Bruker Biospin, 34 rue de l'industrie, 67166 Wissembourg, France.

* corresponding author : olivier.lafon@univ-lille.fr

Keywords: solid-state NMR, correlation, homonuclear, heteronuclear, through-bond, through-space, INADEQUATE, HETCOR, HMQC, INEPT, microporous materials, catalysts, minerals, biomaterials

Abstract: As a local characterization technique endowed with atomic resolution, solid-state NMR spectroscopy provides unique insights on the atomic-level structure and dynamics of inorganic and hybrid materials. In particular, two-dimensional through-bond and through-space correlation experiments allow the observation of covalent bonds and proximities between identical or distinct isotopes, thus providing detailed information on the arrangement of atoms in the materials. Compared to biological and organic samples, inorganic and hybrid materials contain additional NMR-active nuclei, and notably quadrupolar isotopes with nuclear spin $I \geq 1$, such as ^{11}B, ^{27}Al and ^{71}Ga, which are often subject to large quadrupolar interaction. Therefore, specific NMR correlation experiments have been developed to probe the local environment of these quadrupolar isotopes. We provide here an in-depth overview of correlation experiments, which have been employed for the characterization of inorganic and hybrid materials. We present first the through-space and through-bond correlation experiments to probe connectivities and proximities between identical nuclei, and then their counterparts for distinct isotopes. In both cases, we describe the experiments employed for spin-1/2 and quadrupolar isotopes. We indicate the state-of-the-art technique and the isotopes, for which they have been applied. Finally we present how these correlation NMR experiments have provided essential information on the atomic-level structure of different classes of inorganic hybrid materials, including (i) microporous materials (aluminophosphates, zeolites, metal-organic frameworks (MOFs)), (ii) metal oxide catalysts, such as amorphous silica alumina as well as supported metal complexes on alumina or silica, (iii) minerals and biomaterials and (iv) glasses.

1. Introduction

Correlation NMR techniques are a given class of two-dimensional (2D) NMR experiments. They provide information on the through-bond connectivities and through-space proximities between nuclei in solids by coherence transfers during the mixing period through *J*- and dipolar couplings, respectively. The 2D correlation NMR spectra indicate between which spins the coherences are transferred. For improving resolution and sensitivity, these experiments are performed under magic-angle spinning (MAS) conditions. These experiments are classified into two types: the homo- and hetero-nuclear correlation NMR experiments, which probe the connectivities or proximities between

identical and distinct nuclei, respectively, which can be either spin-1/2 or quadrupolar isotopes (see Figure 1).

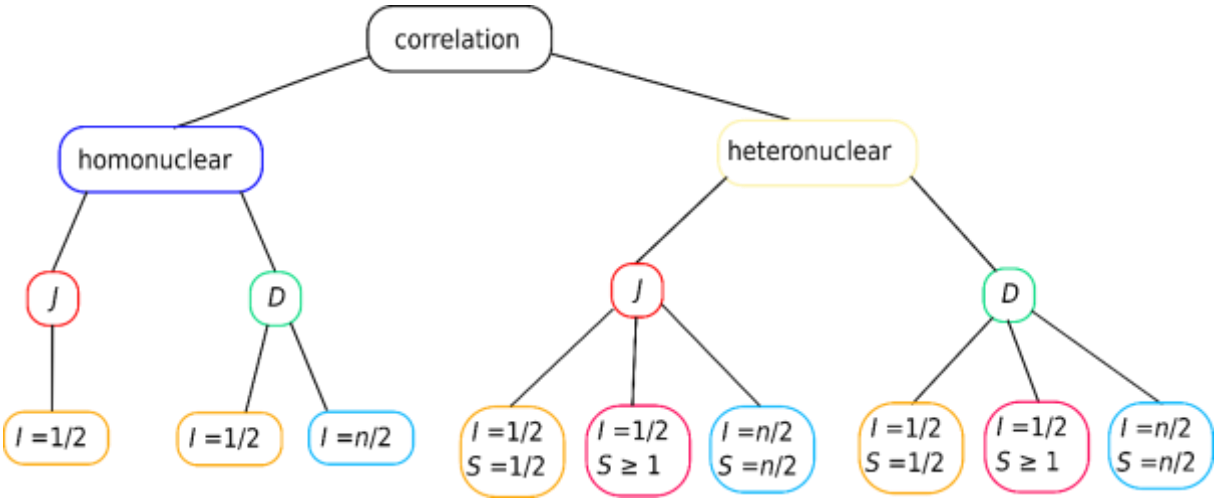

Figure 1. Schematic classification of 2D correlation NMR experiments, which can be employed to probe connectivities and proximities in solids under MAS conditions. $S \geq 1$ denotes the integer and half-integer spin quadrupolar isotopes, whereas I or $S = n/2$ with $n \geq 1$ denotes solely the half-integer quadrupolar nuclei. In the case of quadrupolar nuclei, the coherence transfer in 2D heteronuclear correlation experiment can be mediated by the sum of J-coupling and the second-order quadrupolar-dipolar cross terms, which are not average out by MAS [1,2].

Correlation NMR experiments, including correlation spectroscopy (COSY) [3] between identical nuclei and heteronuclear single-quantum coherence (HSQC) [4] scheme between distinct isotopes, have been initially introduced at the end of the 1970s to probe connectivities between spin-1/2 nuclei in isotropic solutions. In 1980s and 1990s, these correlation experiments were adapted for the study of spin-1/2 isotopes in solids under MAS conditions. Solid-state correlation experiments were first introduced to probe heteronuclear proximities in organic and inorganic solids [5,6]. Then they were applied to observe homonuclear connectivities in plastic crystals [7,8] and later in inorganic solids [9,10]. As regards covalent bonds between distinct isotopes, they have been detected using correlation experiments first in inorganic solids [11], before their observation in organic solids [12]. Correlation experiments to probe homonuclear proximities have been reported first for solid-state amino-acids [13], before their use for phosphate compounds [14].

The correlation solid-state NMR experiments, which are listed above, were first demonstrated for spin-1/2 isotopes. A further advance was their use for quadrupolar nuclei with spin $I \geq 1$, which was demonstrated in the 1990s and 2000s. Heteronuclear correlation experiments have been developed to probe proximities [15,16] and later connectivities [17] between spin-1/2 and half-integer quadrupolar nuclei, such as ^{31}P and ^{27}Al with $I = 5/2$. Then these experiments were also applied to observe proximities [18] and later connectivities [19] between distinct half-integer quadrupolar nuclei, such as ^{27}Al and ^{17}O with $I = 5/2$. These heteronuclear correlation experiments were also combined with the multiple-quantum MAS (MQMAS) scheme to refocus the second-order quadrupolar broadening and hence, allow the acquisition of high-resolution NMR spectra [20,21]. Homonuclear correlation experiments have also been introduced to detect proximities between identical half-integer quadrupolar nuclei, such as ^{23}Na and ^{11}B with $I = 3/2$ [22,23]. Conversely, to the best of our knowledge, these experiments have not yet been applied to detect connectivities between quadrupolar nuclei. Another major advance was the development of heteronuclear correlation for the indirect detection of ^{14}N nuclei, which does not exhibit a central transition (CT) contrary to half-integer quadrupolar nuclei, via spin-1/2 isotopes, such as ^{1}H [1,2]. This approach has more recently been applied for the indirect detection of spin-1/2 nuclei subject to large chemical shift anisotropy (CSA), such as ^{195}Pt [24].

The robustness of through-space correlation NMR experiments has also been improved by the development of more robust dipolar recoupling schemes designed using symmetry [25] and built from composite [26] or adiabatic pulses [27]. These experiments have also been modified so that they enable (i) the observation of longer-range proximities [28], (ii) are compatible with high MAS frequencies [29] and (iii) are less affected by the random fluctuations of MAS frequencies, which cause t_1-noise [30,31]. The sensitivity of these heteronuclear correlation experiments has notably been improved using indirect detection via protons at high MAS frequencies [32]. Several reviews about homo- and hetero-nuclear recoupling sequences, mainly for spin-1/2 nuclei, have been published [33–41]. Through-bond correlation experiments, primarily for spin-1/2 isotopes in organic solids, [42,43] as well as correlation experiments for quadrupolar nuclei[44–48] have also been surveyed. Furthermore, through-bond and through-space correlation experiments for both spin-1/2 and quadrupolar nuclei were presented in reviews about solid-state NMR of a specific class of inorganic materials, including oxide glasses [49–51], crystalline and amorphous aluminophosphates [52], heterogeneous catalysts [53–56], zeolites [57–59] and metal-organic frameworks [58,60].

We provide here an overview of correlation NMR experiments for inorganic solids. We notably highlight the state-of-the-art techniques to probe homo- and hetero-nuclear connectivities and proximities of spin-1/2 and quadrupolar nuclei. We also show how these techniques have provided new insights into the atomic-level structure of inorganic materials, including microporous materials, heterogeneous catalysts, minerals, biomaterials and glasses.

2. Correlation between identical nuclei

Connectivities and proximities between identical nuclei can be probed by homonuclear correlation experiments employing coherence transfers based on *J*- and dipolar-couplings, respectively. These experiments can be classified based on the coherences, which are selected during the indirect evolution period, t_1, and which can be either single-, double- or triple-quantum (1Q, 2Q or 3Q) coherences, whereas the 1Q coherences are always detected during the acquisition period, t_2 [35,61]. The sensitivity of these experiments decreases with increasing coherence order during the t_1 period. Nevertheless, 2Q-1Q correlation allows probing the connectivities or proximities between sites with close resonance frequencies, whereas 3Q-1Q correlation permits the observation of triplets of nuclei [61]. We present first the through-bond homonuclear correlation, before the discussion of through-space variants.

2.1 *Through-bond homonuclear correlations*

Connectivities between spin-1/2 nuclei in inorganic solids have been first probed using the COSY experiment, which is a 1Q-1Q correlation and is identical to the experiments used for liquids [8–10,62]. Nevertheless, the conventional COSY experiment suffers from disadvantages that (i) the diagonal and cross-peaks cannot be displayed simultaneously in double absorption mode, (ii) the intense diagonal peaks can obscure cross-peaks in 2D COSY spectra and (iii) the anti-phase components of the cross peaks reduce their overall intensity. The first and second of the above difficulties can be circumvented by the use of the double-quantum filtered COSY (DQF-COSY) experiment, for which the diagonal and cross peaks can be phased in double-adsorption mode [62]. Nevertheless, the DQF-COSY experiment is not optimal for the characterization of solids since it yields anti-phase line shapes, which reduces the intensity of the cross peaks for unresolved couplings. This limitation can be circumvented by using total through-bond correlation spectroscopy (TOBSY), in which radiofrequency (rf) irradiation synchronized with MAS removes the anisotropic interactions, such as dipolar interactions and CSA, as well as the isotropic chemical shifts and only allows the homonuclear *J*-couplings [63]. In particular, this selection of homonuclear *J*-coupling can be achieved using the symmetry-based $\mathrm{R}30_6^{14}$ scheme, which is highly

robust to offset and rf field inhomogeneity [64]. The TOBSY sequence has been used to record 2D ^{31}P 1Q-1Q through-bond homonuclear correlations and hence, to probe ^{31}P-O-^{31}P connectivities in phosphate crystalline phases [64,65]. Nevertheless, the 1Q-1Q correlations, such as DQF-COSY and TOBSY, do not allow the observation of connectivities between nuclei with close resonance frequencies, which is an important limitation for the use in inorganic solids, since these samples often contain nearby sites with similar resonance frequencies.

This limitation can be side-stepped by the use of 2Q-1Q correlation using the incredible natural abundance double quantum transfer experiment (INADEQUATE). The technique was originally introduced in 1980 by Freeman and co-workers in order to probe natural abundance ^{13}C-^{13}C *J*-couplings in the solution state [66–68]. Fyfe *et al*. were amongst the first to recognise the potential for the sequence to be used to study solid materials, reporting in the early 1990s the use of ^{29}Si INADEQUATE for the elucidation of the three-dimensional (3D) lattice structures of zeolites [69,70]. However, one difficulty in applying the INADEQUATE sequence used for liquids to the solid-state is that it yields anti-phase correlations, leading to reduced intensity for unresolved couplings. Hence, this sequence is only suited to solid samples that generate narrow spectral lineshapes, such as the well-defined framework structures studied in the aforementioned works.

In 1999, Lesage *et al*. proposed a modified version of the pulse sequence designed to overcome the limitations of the original technique [71]. This variant, termed “refocused INADEQUATE”, is displayed in Figure 2. The evolution under homonuclear dipolar interactions and CSA is suppressed by the synchronization with MAS, *i.e.* the delays between the centers of the rf pulses are equal to an integer multiple of rotor period, $\tau_R = 1/\nu_R$, where ν_R is the MAS frequency, whereas the 180° pulses in the middle of the first and second τ delays, termed defocusing and refocusing delays, respectively, refocus the evolution under isotropic chemical shifts. During the defocusing delay, the transverse magnetization evolves under homonuclear *J*-couplings into anti-phase 1Q coherences, which are converted into 2Q coherences by the second 90° pulse. In the absence of losses, the creation of 2Q coherences for an isolated S_2 spin pair is maximum for $\tau = 1/(2J_{SS})$, where J_{SS} denotes the *J*-coupling constant between the observed *S* spins. These coherences evolve at the sum of the isotropic chemical shifts of the correlated nuclei during the t_1 period and are converted back into anti-phase 1Q coherence by the third 90° pulse. In contrast with the original INADEQUATE sequence, the refocused INADEQUATE scheme includes a refocusing delay between the third 90° pulse and the acquisition to transform the anti-phase 1Q coherences into in-phase signal before the acquisition. This sequence is especially useful for the study of disordered solids exhibiting NMR signals broader than the strength of the homonuclear *J*-couplings [71,72].

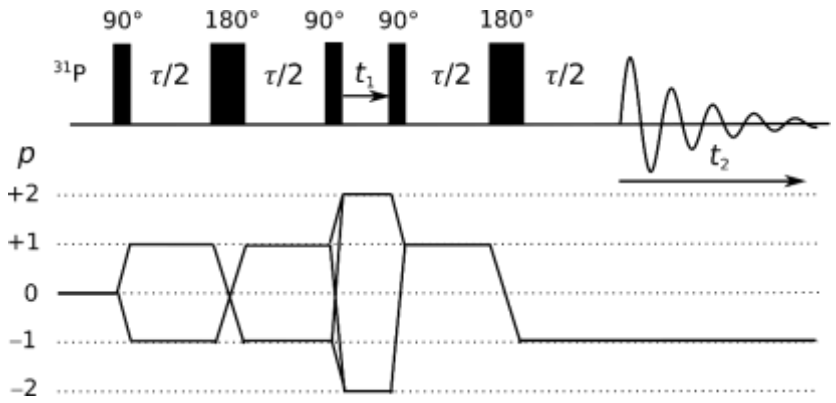

Figure 2. Pulse sequence of 2D ^{31}P refocused INADEQUATE experiment along with desired coherence transfer pathways. Figure adapted from ref. [73]. The initial 90° pulse can be replaced by ^{1}H→^{31}P cross-polarization (CP) transfer to enhance the sensitivity and/or to select the ^{31}P nuclei near protons.

If the refocused INADEQUATE sequence was first applied for the observation of connectivities between ^{13}C nuclei in organic solids, its utility to detect *J*-coupling between ^{31}P nuclei, which has a 100% natural isotopic abundance, has been later demonstrated in phosphorus-containing crystalline and amorphous solids, notably by the solid-state NMR group at CNRS Orléans, France. Several publications have demonstrated the use of 2D ^{31}P refocused INADEQUATE for the structural characterisation of P-O-P connectivities in $Zn_2P_2O_7$ [74] and SnP_2O_7 crystalline powders (see Figure 3) [75] as well as lead phosphate glasses [74,76]. The *J*-coupling constants between ^{31}P nuclei through P-O-P linkage typically range from 16 to 34 Hz [75,77]. It has also been shown that the 2D INADEQUATE spectrum can exhibit diagonal peaks in the absence of *J*-coupling between ^{31}P nuclei with the same isotropic chemical shift but distinct magnitude or orientation of their CSA tensors since the n = 0 rotational resonance (R^2) reintroduces the dipolar interaction between them [73]. The intensity of these anomalous diagonal peaks decreases at higher MAS frequency and lower static magnetic field. 2D ^{31}P 3Q-1Q homonuclear correlation spectra have also been recorded for $Pb_3P_4O_{13}$ crystalline compound and

phosphate glasses using the same sequence as refocused INADEQUATE but distinct phase cycling [61]. These spectra allow for the observation of P-O-P-O-P trimers.

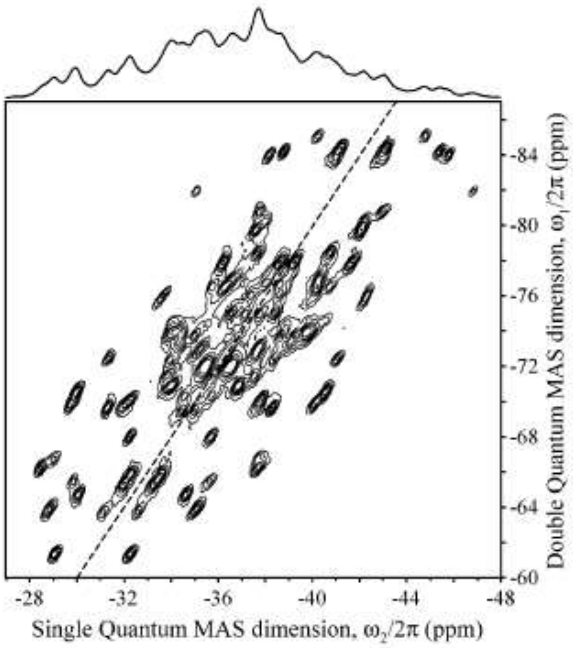

Figure 3. 2D ^{31}P refocused INADEQUATE spectrum of SnP_2O_7 crystalline powder acquired at a static magnetic field B_0 = 7 T with ν_R = 10 kHz. This spectrum shows 46 pairs of cross-correlation peaks resulting from P-O-P connections. Reprinted with permission from reference [75]. Copyright 2003, American Chemical Society.

As mentioned above, INADEQUATE experiments have also been used to probe connectivities between ^{29}Si nuclei in solids. The two-bond *J*-coupling constant, $^2J_{SiOSi}$, between ^{29}Si nuclei of Si–O–Si linkages is typically lower than 15 Hz in silicate materials [78]. Furthermore, the natural abundance of the ^{29}Si isotope is only 4.68% and hence, the probability of having two sites containing ^{29}Si isotope is as low as 0.2%. Therefore, the first reported 2D ^{29}Si INADEQUATE experiments on isotopically unmodified zeolites lasted several days [69]. The sensitivity of this experiment has been improved by ^{29}Si isotopic enrichment [79] and/or dynamic nuclear polarization (DNP) under MAS (see Figure 4) [80–82]. This latter technique enhances the NMR signal by transferring the polarization of unpaired electrons to the nuclear spins through microwave irradiation [83]. The unpaired electrons can be exogenous biradicals, which are incorporated into the sample by impregnation with a solution of biradicals. In these conditions, DNP primarily enhances the NMR signals of nuclei located near surfaces [84,85]. Therefore, DNP-enhanced 2D ^{29}Si INADEQUATE experiments have been mainly applied to probe the ^{29}Si-^{29}Si connectivities near the surface of particles [80,81]. Nevertheless, unpaired electrons in the bulk region of the materials, such as oxygen vacancies in γ-irradiated fused quartz, can also be used as a source of polarization for DNP to enhance the sensitivity of ^{29}Si INADEQUATE experiment [86]. Furthermore, the use of the 2D ^{29}Si refocused INADEQUATE sequence allows the observation of ^{29}Si-^{29}Si connectivities in disordered and amorphous materials, for which the linewidths exceed the ^{29}Si-^{29}Si *J*-coupling constants [87,88]. In addition, a variant of the 2D ^{29}Si refocused INADEQUATE sequence incorporating a z-filter between the refocusing delay and the acquisition period has been employed to eliminate undesired antiphase contributions due to multiple couplings [88,89]. Finally the sensitivity of 2D ^{29}Si INADEQUATE experiments can be improved by the Carr-Purcell Meiboom-Gill (CPMG) scheme, *i.e.* the acquisition of a train of echoes during the acquisition period by applying a train of 180° pulse [90].

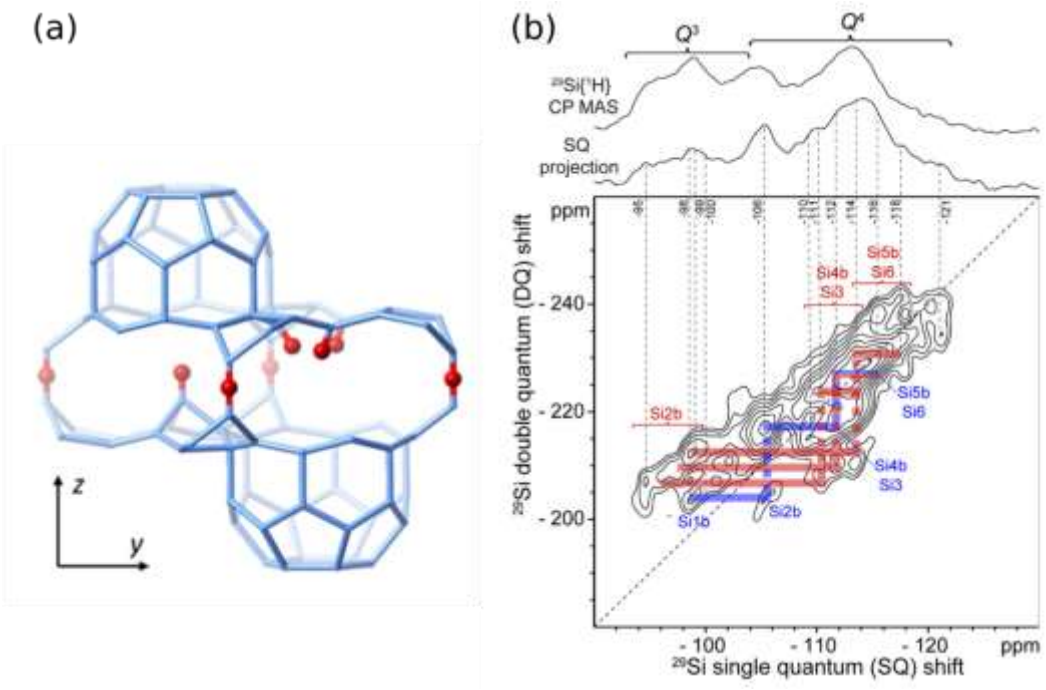

Figure 4. (a) Schematic structure of the interlayer region of the calcined form of the zeolite SSZ-70. The terminal and interlayer-bridging O atoms are shown in red, whereas the others have been omitted. (b) DNP-enhanced ^{29}Si refocused INADEQUATE 2D spectrum of isotopically unmodified SSZ-70 zeolite at 9.4 T and ~100 K with ν_R = 8 kHz. The DNP-enhanced ^{1}H→^{29}Si CPMAS 1D spectrum acquired under the same conditions is shown along the 1Q dimension. The blue and red lines indicate the connectivity paths to isolated silanol (on the left of subfigure a) and nested silanol groups (on the right of subfigure b), respectively. Figure adapted from ref. [82]. Copyright 2017, American Chemical Society.

More recently, a DNP-enhanced refocused INADEQUATE scheme has been applied to probe the connectivities between surface and core ^{113}Cd nuclei of CdS quantum dots [91]. This experiment relies on ^{113}Cd–S–^{113}Cd *J*-coupling constants, which are approximately equal to 100 Hz.

To the best of our knowledge, 2D homonuclear correlation between quadrupolar nuclei via homonuclear *J*-couplings has not been reported. Conversely, connectivities between ^{27}Al nuclei connected via O bridges to the same ^{31}P nucleus in microporous crystalline $AlPO_4$-14 compounds have been probed using relay via two-bond ^{31}P-^{27}Al *J*-couplings and 2D through-bond homonuclear correlation experiment derived from heteronuclear single-quantum correlation (HSQC) sequence [92].

2.2 *Through-space homonuclear correlations*

Through-space homonuclear correlations, which rely on coherence transfer via homonuclear dipolar couplings, allow the observation of proximities between identical nuclei and hence, complement through-bond homonuclear correlations. For isotopes in the first periods of the periodic table, the homonuclear dipolar couplings are usually larger than the *J*-couplings and yields faster coherence transfers. As a result, through-space homonuclear correlation experiments are usually more efficient than their through-bond counterparts. These experiments can be classified based on the order of the Hamiltonian governing the through-space coherence transfer as well as the coherence order during t_1 period. Through-space homonuclear correlation experiments have been applied to both spin-1/2 and half-integer quadrupolar nuclei.

2.2.1 Between spin-1/2 nuclei

Through-space homonuclear correlations can be achieved through either the first- or second-order Hamiltonian involving the homonuclear dipolar interaction.

First-order recoupling. The contribution of dipolar interactions to the first-order Hamiltonian is averaged out by MAS. Nevertheless, this interaction is reintroduced between spins having isotropic chemical shifts differing by a multiple of the MAS frequency, *i.e.* the R^2 condition [93–95]. This approach has been recently applied to record 2D ^{89}Y 1Q-1Q through-space homonuclear correlation spectrum of yttrium-doped ceria [96]. To compensate the long longitudinal relaxation time of the ^{89}Y isotope, which typically reaches hundreds of seconds, and its low gyromagnetic ratio ($|\gamma(^{89}Y)/\gamma(^{1}H)| = 4.92\%$), the sensitivity of this 2D ^{89}Y homonuclear correlation was enhanced using DNP transfer from paramagnetic Gd(III) dopants. Nevertheless, the R^2 approach is a frequency-selective recoupling, which reintroduces the dipolar couplings only between specific sites at a given MAS frequency.

A more broadband and versatile approach to reintroduce the homonuclear dipolar couplings under MAS in the first-order Hamiltonian relies on the application of rf pulses, which prevents its refocusing by MAS. In particular, some first-order homonuclear dipolar recoupling schemes have been developed, which selectively restore the homonuclear dipolar coupling, while removing the unwanted interactions, such as isotropic and anisotropic chemical shifts as well as heteronuclear *J*- and dipolar couplings. The first-order recoupling schemes allow the detection of proximities between the nearest neighbors. Weak cross-peaks are observed for nuclei further apart owing to the dipolar truncation, *i.e*. the large homonuclear recoupled dipolar interactions between nearby nuclei attenuates the coherence transfers between distant nuclei [97].

A widely used first-order homonuclear dipolar recoupling to acquire 2D 1Q-1Q correlation is the radio-frequency driven-recoupling (RFDR), where one 180° pulse is applied every rotor period [13]. This recoupling is robust, easy to set-up and works at all MAS frequencies. Nevertheless, when the pulse length represents a significant fraction of the rotor period, the amplitude of the recoupled dipolar interaction depends on the rf field strength. This variant has been called finite-pulse RFDR (fp-RFDR) [98]. The RFDR scheme has notably been employed to acquire 2D 1Q-1Q through-space correlation spectra of ^{31}P, ^{29}Si and ^{1}H nuclei of inorganic and hybrid materials [99–101].

Nevertheless, the 1Q-1Q through-space correlation does not allow the observation of proximities between nuclei with close resonance frequencies. This limitation can be circumvented by the acquisition of 2Q-1Q through-space correlation spectra. Various first-order homonuclear dipolar recoupling have been designed to excite and reconvert the 2Q coherences between identical nuclei, including back-to-back (BaBa) scheme [14,102], RFDR bracketed by 90° pulses (denoted [fp-RFDR]) [103,104], and symmetry-based sequences, such as POST-C7 [26], SPC5 [105], $SR26_4^{11}$ [106,107] and $R20_2^9$ [108]. The choice of the recoupling sequence depends on the MAS frequency and the strength of the spin interactions. The 2D ^{31}P and ^{29}Si 2Q-1Q through-space correlation spectra are usually acquired at moderate MAS frequencies, $\nu_R \approx 10$ kHz, which are compatible with the use of POST-C7 and $SR26_4^{11}$ sequences, which require nutation frequencies, $\nu_1 = 7\nu_R$ and $6.5\nu_R$, respectively [107,109]. In particular, the $SR26_4^{11}$ recoupling benefits from high robustness and hence, is especially beneficial to observe the small ^{29}Si-^{29}Si dipolar couplings. Conversely, 2D ^{1}H 2Q-1Q through-space correlation experiments are carried out at high MAS frequencies, $\nu_R \geq 50$ kHz, to improve the spectral resolution by averaging out the ^{1}H-^{1}H dipolar interactions. For that purpose, symmetry-based first-order homonuclear dipolar recoupling schemes, such as $R12_2^5$, with short cycle time and low rf field requirement ($\nu_1 = 3\nu_R$) have been introduced [110]. Besides organic solids, these recoupling sequences have been used to probe ^{1}H-^{1}H proximities in hybrid solids, including metal-organic frameworks , as seen in Figure 6 [111].

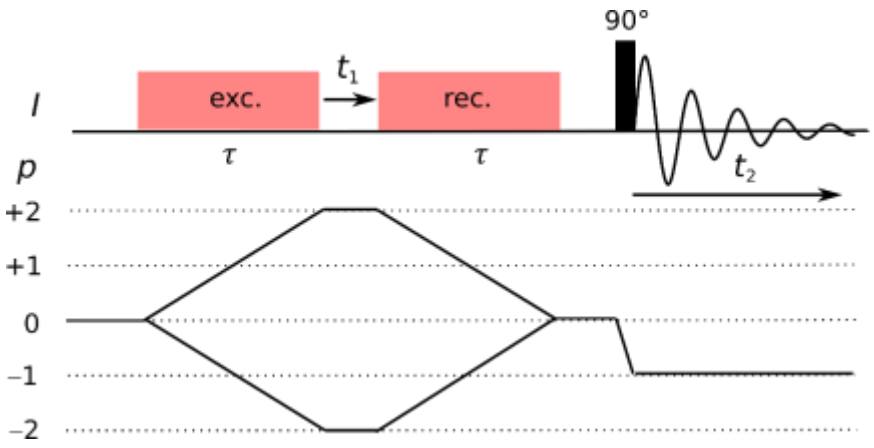

Figure 5. Pulse sequence of 2D 2Q-1Q through-space homonuclear correlation for isotope *I* along with desired coherence transfer pathways. During the excitation (exc.) and reconversion (rec.) blocks, the *I*-*I* dipolar interaction are reintroduced in the first-order Hamiltonian by recoupling schemes, such as BaBa, [fp-RFDR], POST-C7, SPC5, $SR26_4^{11}$ or $R12_2^5$. The initial longitudinal magnetization can be created by ^{1}H→*I* CP transfer followed by a flip-back 90° pulse on the *I* channel.

The pulse sequence and the coherence transfer pathway of 2D 2Q-1Q through-space homonuclear correlation are displayed in Figure 5. The first recoupling scheme transforms the longitudinal magnetization into 2Q coherences, which evolve during the t_1 period. The second recoupling scheme reconverts these coherences into longitudinal magnetization, which is transformed into observable transverse magnetization by the 90° pulse. Signals passing through 2Q coherences during the t_1 period are selected by a four-step phase cycle of the recoupling scheme used either for excitation or reconversion. Like for through-bond correlation, the sensitivity of ^{29}Si through-space correlation can be enhanced by CPMG [112] as well as DNP to detect ^{29}Si-^{29}Si proximities near surfaces [80,113]. Similarly the sensitivity gain provided by DNP has been leveraged to observe proximities between ^{31}P sites near the surface of nanoparticles [114]. 2D 2Q-1Q through-space homonuclear correlation experiments have also been employed to probe ^{19}F-^{19}F proximities in inorganic fluorides [115–118]. These experiments require robust first-order homonuclear dipolar recoupling since ^{19}F nuclei often exhibit large isotropic and anisotropic chemical shifts. Note also that the proximities between three protons have also been probed using 2D 3Q-1Q through-space homonuclear correlation experiments [119–121].

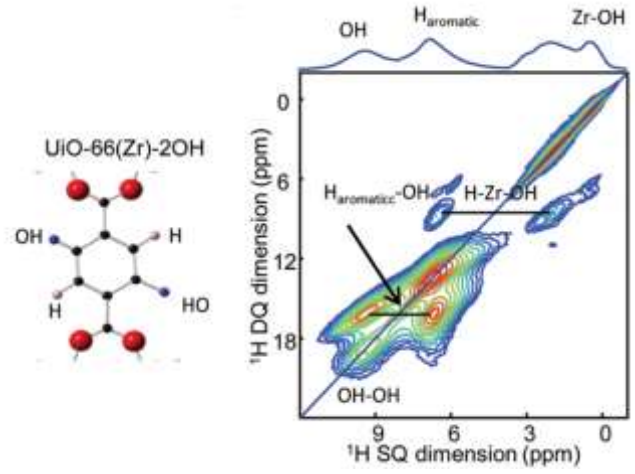

Figure 6. 2D ^{1}H 2Q-1Q through-space homonuclear correlation of Zr-based metal-organic framework (MOF) functionalized with OH groups acquired using $R12_2^5$ recoupling at B_0 = 18.8 T with ν_R = 62.5 kHz. Figure adapted from ref. [111]. Copyright 2012, American Chemical Society.

Second-order recoupling. These schemes rely on cross-terms between distinct homonuclear dipolar interactions or homo- and hetero-nuclear dipolar interactions in the second-order Hamiltonian. Hence, these cross-terms contain products of operators of three distinct spins. These recoupling schemes are less susceptible to dipolar truncation than first-order recoupling and they allow probing longer-range distance. Nevertheless, the magnitude of the second-order Hamiltonian is inversely proportional to the MAS frequency and hence, these second-order recoupling are less efficient at high MAS frequency.

In the case of nuclei subject to several large homonuclear dipolar interactions, such as protons and ^{19}F nuclei, proximities can also be probed using spin diffusion experiments, which have been first introduced for polymer blends [122] and then have been applied for organic molecules adsorbed in zeolites [123,124] and later inorganic fluorides [125,126]. The pulse scheme used for these spin diffusion experiments is identical to NOESY sequence and is shown in Figure 7a. The 1Q coherences excited by the first 90° pulse evolve during the t_1 period. The second 90° pulse stores the magnetization along the direction of the B_0 field during a mixing time, τ. During this delay, spin diffusion can exchange magnetization between distinct sites. The last 90° pulse converts the longitudinal magnetization into transverse magnetization, which is detected during the acquisition period, t_2. After 2D Fourier transform, we obtain a 2D 1Q-1Q through-space correlation spectrum, as seen in Figure 7b.

Nevertheless, these 2D 1Q-1Q correlation experiments do not allow the observation of proximities between nuclei with close resonance frequencies. This limitation can be circumvented by the use of 2D 2Q-1Q through-space correlation relying on cross-terms between homonuclear dipolar couplings, such as the dipolar homonuclear homogeneous Hamiltonian (DH^3) scheme [127], which has notably been employed to probe proximities between ^{19}F nuclei in inorganic fluorides and fluorinated aluminophosphates [128].

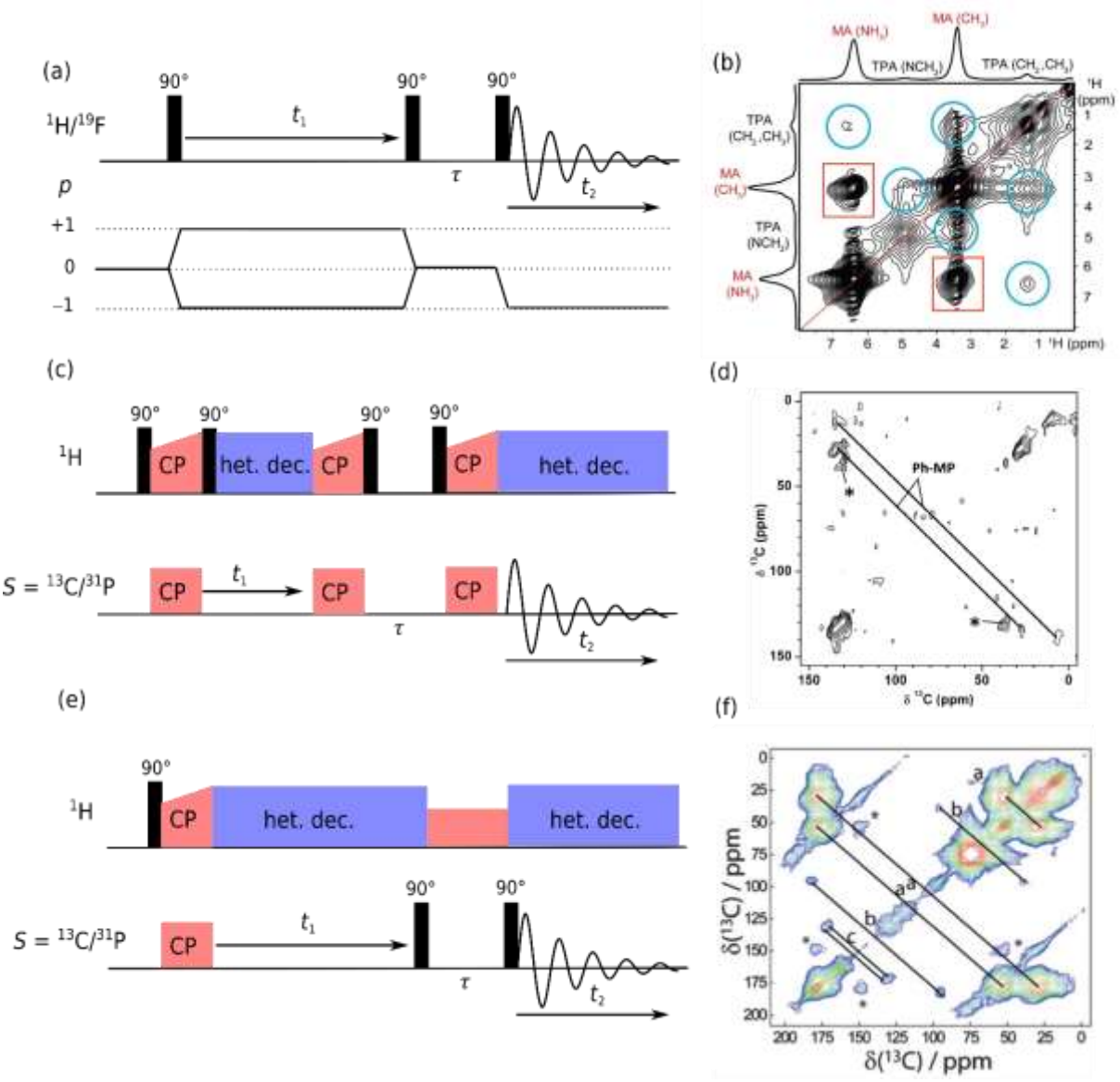

Figure 7. (a) Pulse sequence of 2D ^{1}H or ^{19}F spin diffusion experiment along with desired coherence transfer pathways. (b) 2D ^{1}H spin diffusion spectrum of methyl ammonium lead iodide containing 4% tetrapropylammonium at B_0 = 18.8 T with ν_R = 35 kHz. (c) Pulse sequence of 2D 1Q-1Q *S*HH*S* experiment. (d) DNP-enhanced 2D ^{13}C CHHC spectrum of bifunctionalized mesoporous silica nanoparticles. (e) Pulse sequence of 2D 1Q-1Q homonuclear correlation experiments, such as PDSD, DARR and PARIS, between *S* = ^{13}C or ^{31}P nuclei. These experiments differ by the rf irradiation applied on ^{1}H channel during the mixing time τ. (f) DNP-enhanced 2D ^{13}C DARR spectrum of ^{13}C-enriched methionine adsorbed on Pd nanoparticles supported on γ-alumina and impregnated with a TEKPol solution in 1,1,2,2-tetrachloroethane (TCE) at B_0 = 9.4 T and 105 K with ν_R = 12 kHz. Figures b, d and f adapted from refs. [129–131], respectively. Copyright 2020, Wiley, 2017, American Chemical Society, 2016, Royal Society of Chemistry.

Nuclei other than ^{1}H and ^{19}F, such as ^{13}C or ^{31}P, are subject to smaller homonuclear dipolar couplings and spin diffusion due to cross-terms between homonuclear dipolar couplings is quenched under MAS. A first possibility to circumvent this issue is to 2D 1Q-1Q *S*HH*S* sequence, in which the *S*-edited ^{1}H longitudinal magnetization is exchanged by ^{1}H-^{1}H spin diffusion during a mixing period placed between two CP transfers (see Figure 7c). This experiment has been applied to probe the proximities between organic functional groups bound to silica surface (see Figure 7d)[113]. Nevertheless, cross-terms between homonuclear dipolar interactions and heteronuclear dipolar interaction with protons can transfer magnetization between nuclei with different frequencies. This process is referred to as proton-driven spin diffusion (PDSD) [132]. The corresponding pulse sequence is shown in Figure 7e and is identical to that of spin diffusion experiment for the detected nucleus, *I*, except that the initial 90° pulse is replaced

by a $^{1}H \rightarrow I$ CP transfer and heteronuclear dipolar decoupling schemes are applied on ^{1}H channel during the t_1 and t_2 periods to suppress ^{1}H-*I* dipolar couplings. Conversely, during the mixing time, τ, no irradiation is applied in the case of PDSD sequence so that the cross-terms between ^{1}H-*I* and *I*-*I* dipolar couplings transfer magnetization between *I* spins. Nevertheless, the efficiency of this transfer decreases for MAS frequency and B_0 field strength above 20 kHz and 14.1 T (^{1}H Larmor frequency of 600 MHz). Irradiation on the ^{1}H channel can be applied during the mixing time, τ, to restore these cross-terms under fast MAS and at high magnetic field. For instance, the sequences called dipolar-assisted rotational resonance (DARR) [133] or radio frequency assisted diffusion (RAD) [134] employ continuous wave rf irradiation with nutation frequency equal to 1 or 2 times the MAS frequency during the mixing time, whereas phase-alternated irradiation, such as phase-alternated recoupling irradiation scheme (PARIS) [135,136], improves the magnetization transfer at high MAS frequencies. The 1Q-1Q correlation techniques have been widely employed for the observation of ^{13}C-^{13}C proximities in biomolecules [41]. Nevertheless, they have also been recently applied to probe proximities between C sites of ^{13}C-enriched organic molecules adsorbed at the surface of nanoparticles or in zeolites (see Figure 7f) [131,137]. Homonuclear correlation experiments for ^{31}P nuclei have also been applied to probe the proximities between Lewis and Brønsted acid sites in zeolites using P-containing probe molecules [138].

2.2.2 Between half-integer quadrupolar nuclei

Like for spin-1/2 nuclei, through-space homonuclear correlation experiments have been developed to probe proximities between identical half-integer quadrupolar nuclei, including ^{11}B, ^{17}O, ^{23}Na and ^{27}Al [44,47,139]. Nevertheless, these experiments are more challenging for these isotopes than for spin-1/2 nuclei owing to the larger size of the density matrix, equal to $(2I+1)^2$ for a spin-*I* nucleus, and the presence of large anisotropic quadrupolar interaction. This interaction has a magnitude much larger than the rf irradiation and the MAS frequency, resulting in complicated spin dynamics during rf irradiation under MAS conditions. Therefore, 2D through-space homonuclear correlation experiments were initially achieved using recoupling techniques, which do not involve rf irradiation, such as (i) cross-terms between homonuclear dipolar couplings and either first-order quadrupolar interaction [140,141] or heteronuclear dipolar couplings to protons [142,143] in the second-order Hamiltonian, (ii) R^2 condition [144] or (iii) off-magic-angle spinning [23,145,146]. Nevertheless, this latter approach reintroduces other unwanted interactions and hence, decreases the spectral resolution, whereas R^2 method requires MAS frequency matching the difference in isotropic chemical shifts between the recoupled spins and the transfer efficiency of second-order recoupling decreases at higher MAS frequencies.

Dipolar couplings between identical half-integer quadrupolar nuclei have also been restored by the rf irradiation of the CT between energy levels $m_I = -1/2$ and $+1/2$ with m_I the magnetic quantum number [147,148]. This approach has the advantage to be more versatile than those without rf irradiation. Nevertheless, the applied rf field should be weak to avoid the excitation of satellite transitions (STs) and the related signal losses. In particular, efficient recoupling has been achieved using homonuclear rotary recoupling (HORROR) condition, $\nu_{\mathrm{nut}}^{\mathrm{CT}} = (I + 1/2)\nu_1 = \nu_R/2$, where $\nu_{\mathrm{nut}}^{\mathrm{CT}}$ is the nutation frequency of the CT and ν_1 is the rf field strength [149]. The robustness to offset and rf field inhomogeneity has been improved by the use of $\mathrm{R}N_n^{\nu}$ symmetry-based recoupling and supercycling [150–155]. Zero-quantum (0Q) dipolar recoupling, such as $\mathrm{SR}2_2^1$, can be employed to acquire 2D 1Q-1Q correlation spectra [150,153,154], whereas 2Q recoupling, such as $\mathrm{BR}2_2^1$, can be applied to record 2D 2Q-1Q correlation experiments [151,152,155]. The 1Q-1Q correlation pulse sequence is identical to that shown in Figure 7a, except that the 90° pulse are selective of the CT and 0Q recoupling scheme is applied during the τ delay. The 2Q-1Q correlation spectra between half-integer quadrupolar nuclei are acquired using the pulse sequence of Figure 5. Nevertheless, a CT-selective 180° pulse must be applied during the t_1 period

to eliminate 2Q coherences between energy levels m_I and m_I+2 of a single *I*-spin nucleus [149]. The 2Q-1Q variant has the advantage to allow the observation of proximities between nuclei with close resonance frequencies. Furthermore, the $\mathrm{BR}2_2^1$ recoupling benefits from high robustness to offset, which contributes to the reintroduction of the homonuclear dipolar couplings [155]. Nevertheless, the efficiency of this recoupling drops on resonance and hence, the carrier frequency must be carefully chosen. The intensity of these homonuclear correlation experiments between CTs of half-integer quadrupolar nuclei can be enhanced by the irradiation of the STs at the beginning of the pulse sequence, in such way that the population difference across the CT is enhanced [150–152]. Note that 3D ^{14}N/^{14}N/^{1}H through-space correlation has been developed to probe proximities between ^{14}N nuclei since their lack of CT prevents the application of the above correlation experiments based on the selective irradiation of the CT [156]. Nevertheless, they have only been applied so far to solid-state peptides.

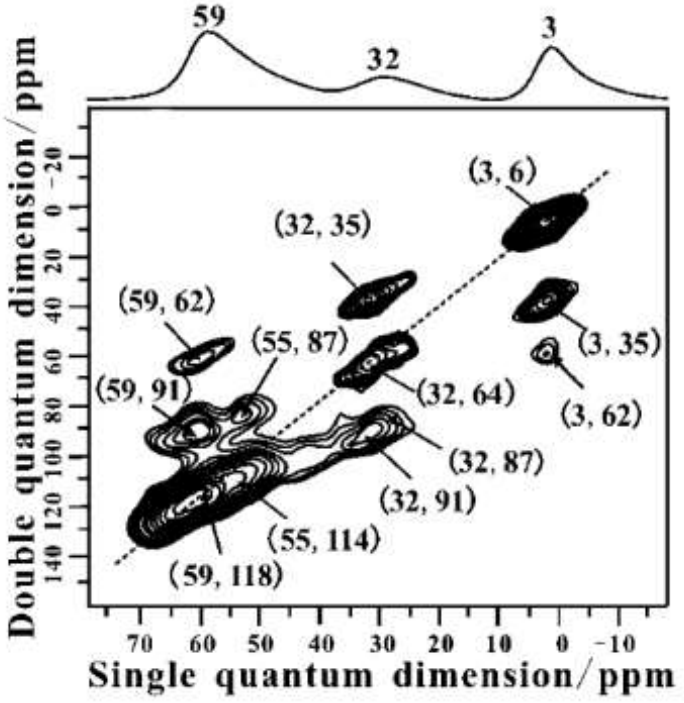

Figure 8. 2D ^{27}Al 2Q-1Q through-space correlation spectrum of HY zeolite calcined at 700 °C. The isotropic shifts are indicated near the peaks. The peak resonating at 59 ppm is assigned to framework AlO_4 species of Brønsted acid sites SiOHAl, whereas those at 32 and 3 ppm stem from extra-framework AlO_5 and AlO_6 sites, respectively, acting as Lewis acid sites. The auto-correlation peaks on the diagonal indicate proximities between identical sites, whereas the cross peaks outside the diagonal reveal proximities between distinct Al sites. Figure adapted from ref. [157]. Copyright, 2010, Wiley.

3. Correlation between distinct nuclei

Connectivities and proximities between distinct isotopes, *I* and *S*, can be observed using heteronuclear correlation experiments based on coherence transfers through *J*- and dipolar couplings, respectively. These experiments rely on either a single coherence transfer $I \rightarrow S$, when the excited and detected isotopes differ, or two successive coherence transfers $S \rightarrow I \rightarrow S$, when the excited isotope is identical to that detected. The relative sensitivity of these two approaches depends on the gyromagnetic ratios, longitudinal relaxation times, T_1, coherence lifetimes and line widths of the correlated nuclei [32]. The heteronuclear correlation experiment, in which the *S* spin is detected and the *I* spin is indirectly observed, is denoted *S*{*I*} hereafter.

3.1 *Through-bond heteronuclear correlations*

The connectivities between distinct isotopes in inorganic solids have been probed using through-bond heteronuclear correlation experiments [11] similar to those used in isotropic solution, including the refocused insensitive nuclei enhanced by polarization transfer (*J*-RINEPT) based on a single transfer $I \rightarrow S$ [17,158,159] as well as the heteronuclear multiple-quantum coherence (*J*-HMQC) scheme relying on a double transfer $I \rightarrow S \rightarrow I$ [12,160,161]. These experiments are carried out under MAS to average out anisotropic interactions and hence, to improve the resolution. Furthermore, the *J*-coupling constants between nuclei separated by two or more covalent bonds usually do not exceed a few tens of hertz. Hence, these coherence transfers are only efficient when at least one of the correlated isotope exhibits sufficiently long time constant, T_2', for the decay of transverse magnetization, which is not refocused by a 180° pulse.

3.1.1 Between spin-1/2 isotopes

The *J*-RINEPT pulse sequence is displayed in Figure 9. The first 90° pulse on the *I* channel excites the *I*-spin transverse magnetization, which is encoded by the isotropic chemical shift during the t_1 period since the 180° pulse applied to the *S* channel in the middle of the t_1 period refocuses the evolution under *I*-*S* *J*-couplings. During the defocusing delay, τ, the simultaneous 180° pulses on *I* and *S* channels refocus the evolution under the isotropic chemical shifts but not that under *I*-*S* *J*-couplings. This evolution converts the in-phase transverse magnetization of the *I* nuclei into antiphase magnetization with respect to the *I*-*S* *J*-couplings. The simultaneous 90° pulses on *I* and *S* channels convert this antiphase magnetization of the *I* spin into antiphase magnetization of the *S* spin, which is subsequently converted into in-phase magnetization of the *S* spin during the refocusing delay, τ'. This in-phase magnetization is detected during the t_2 period. For an isolated *I*-*S* pair and in the absence of losses, the optimal τ and τ' delays are equal to $1/(2J_{IS})$.

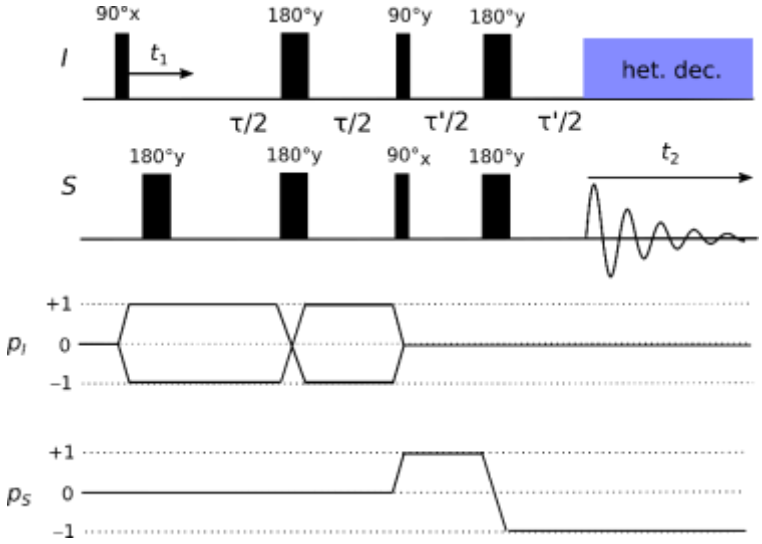

Figure 9. Pulse sequence along with desired coherence transfer pathways of 2D *S*{*I*} through-bond heteronuclear correlation using $I \rightarrow S$ *J*-RINEPT transfer. The evolution under *I*-*S* *J*-couplings is refocused during t_1 and t_2 periods.

The *J*-coupling constants between covalently bonded ^{1}H-^{13}C nuclei, $^1J_{CH}$, are typically equal to 140 Hz and the ^{13}C{^{1}H} *J*-RINEPT sequence based on these coupling has been employed to observe H–C bonds of organic molecules, such as surfactants, in mesoporous silica [162]. It has been shown that the transfer efficiency of ^{1}H-^{13}C *J*-RINEPT scheme can be improved by reducing the coherence losses due to ^{1}H-^{1}H dipolar couplings during τ and τ' delays using ^{1}H homonuclear dipolar decoupling [163] or fast MAS [164]. In particular, the T_2' time constants of ^{1}H and ^{13}C nuclei are proportional to the MAS frequency [164]. Furthermore, a three-fold enhancement in sensitivity of 2D ^{1}H-^{13}C *J*-RINEPT experiment, which

corresponds to a time saving by almost an order of magnitude, has been achieved using indirect detection of ^{13}C nuclei via protons ($^{1}H\{^{13}C\}$) under fast MAS (see Figure 10) [164].

Similarly the H–Si bonds in poly(cyclosilane) have been observed using $^{29}Si\{^{1}H\}$ *J*-RINEPT scheme incorporating ^{1}H homonuclear dipolar decoupling and based on coherence transfer via $^{1}J_{SiH}$ coupling constants, which are typically equal to 170 Hz [108]. The sensitivity of this experiment has been improved using DNP to detect silicon hydride sites (SiH) at the surface of silicon nanoparticles [91]. The strength of the *J*-coupling constant decreases for increasing number of bonds between the coupled spins. Nevertheless, geminal couplings through two covalent bonds can be large enough to achieve *J*-RINEPT transfer. For instance, the geminal ^{29}Si-O-^{31}P *J*-coupling constants typically range from 4 to 15 Hz and have been leveraged to correlate the ^{29}Si and ^{31}P signals of a mixture of silicophosphate crystalline phases [159].

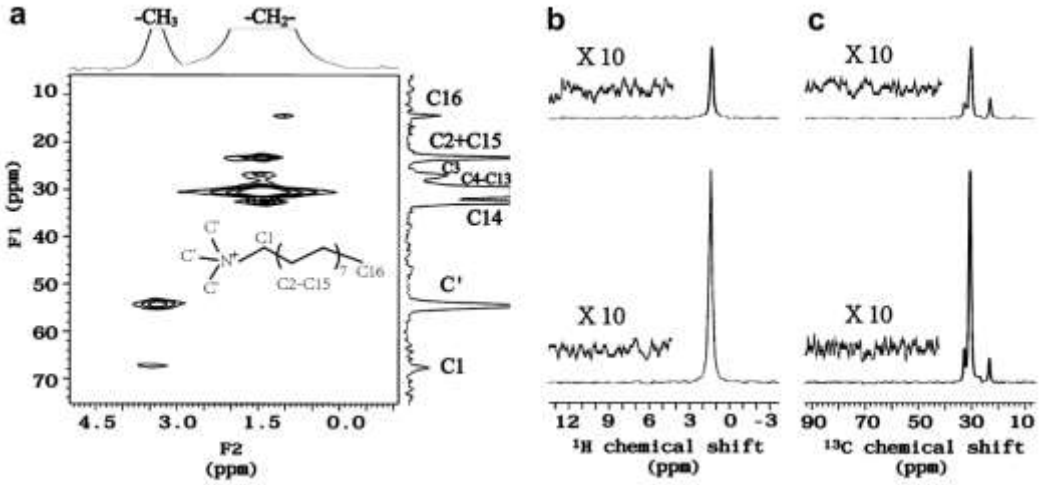

Figure 10. (a) 2D $^{1}H\{^{13}C\}$ *J*-RINEPT spectrum of cetyltrimethyl ammonium bromide (CTAB) surfactant in mesoporous silica recorded in 50 min at B_0 = 14.1 T with ν_R = 40 kHz. The initial 90° pulse on *I* = ^{13}C channel is replaced by $^{1}H \rightarrow {}^{13}C$ CP transfer. Furthermore, the residual initial ^{1}H magnetization, which is not transferred to ^{13}C nuclei, is eliminated by the application of purge pulses. (b-c) Selected cross sections along the (b) ^{1}H and (c) ^{13}C dimensions of the 2D $^{13}C\{^{1}H\}$ (top traces) and $^{1}H\{^{13}C\}$ (bottom traces) *J*-RINEPT spectra acquired under the same experimental conditions. The noise level is shown as an inset with a vertical expansion by a factor of 10. Figure adapted from ref. [164]. Copyright, 2009, Elsevier.

Figure 11 shows the pulse sequence of *J*-HMQC experiment. The first 90° pulse on *S* channel creates transverse magnetization of *S* nuclei, which evolves under J_{IS} coupling into antiphase magnetization during the first τ delay and then is converted into heteronuclear multiple-quantum coherences by the 90° pulse on *I* channel. These coherences are encoded during t_1 period by the isotropic chemical shift of *I* nuclei before being converted back into antiphase magnetization of *S* nuclei by the second 90° pulse on *I* channel. For an isolated *I*-*S* pair and in the absence of losses, the optimal τ delays are equal to $1/(2J_{IS})$. The *J*-HMQC experiment has notably been employed to correlate the ^{29}Si and ^{31}P signals of a mixture of silicophosphate crystalline phases (see Figure 12) [161] as well as to probe ^{19}F-^{207}Pb and ^{19}F-^{31}P covalent bonds in β-Pb_2ZnF_6 [165] and oxyfluoride glass-ceramics[166], respectively. More recently, as shown in Figure 13, the sensitivity of $^{77}Se\{^{113}Cd\}$ *J*-HMQC experiment has been enhanced by DNP to probe the ^{77}Se-^{113}Cd covalent bonds near the surface of CdSe nanocrystals [167].

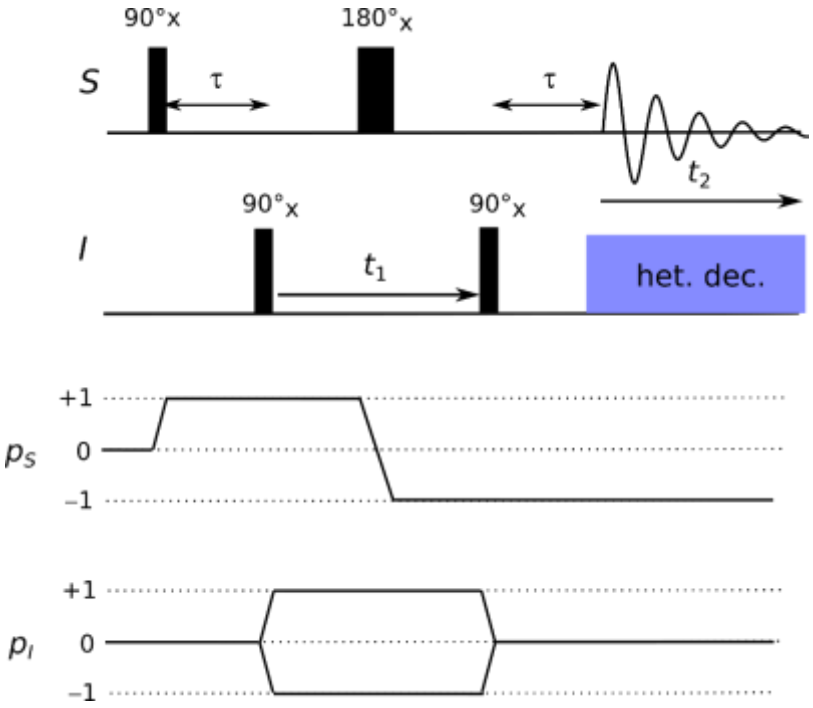

Figure 11. Pulse sequence along with desired coherence transfer pathways of 2D *S*{*I*} *J*-HMQC experiment.

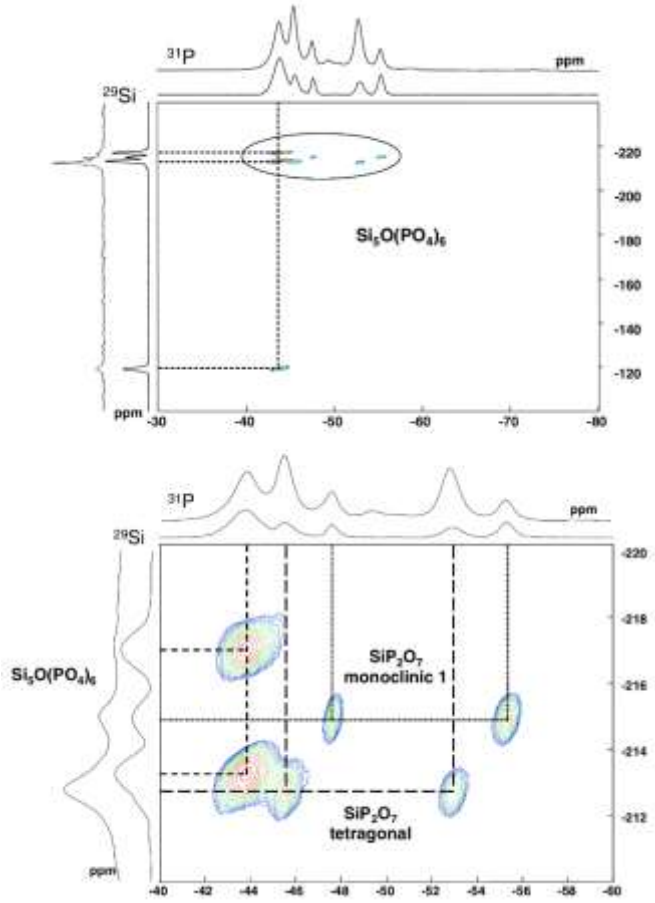

Figure 12. 2D ^{31}P{^{29}Si} *J*-HMQC spectrum of a mixture of $Si_5O(PO_4)_6$ and SiP_2O_7 polymorphs acquired at B_0 = 7 T with ν_R = 14 kHz. The 1D ^{29}Si and ^{31}P MAS NMR spectra are displayed along the ^{29}Si and ^{31}P dimensions of the 2D spectra, beside the projections. The bottom spectrum displays an expansion of the circled region in the top spectrum. Figure adapted from ref. [161]. Copyright, 2009, Elsevier.

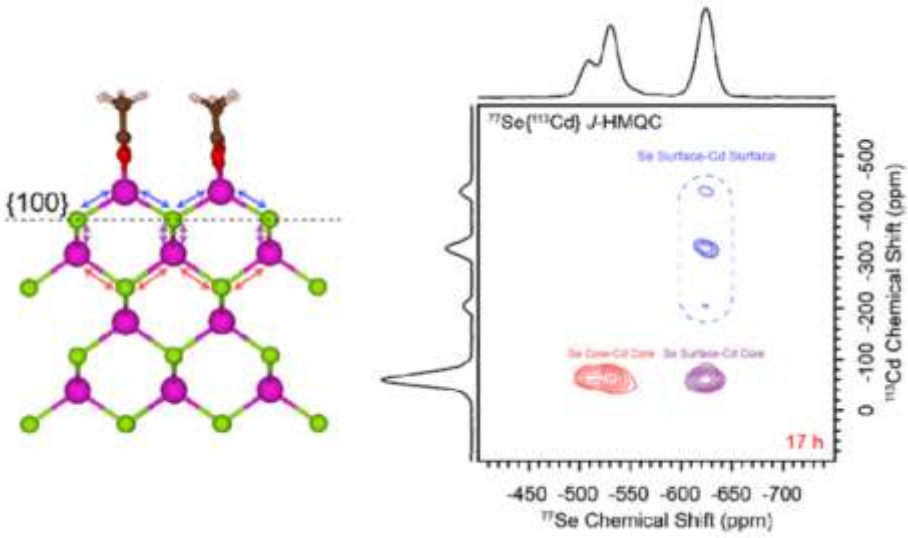

Figure 13. DNP-enhanced 2D ^{77}Se{^{113}Cd} *J*-HMQC spectrum of CdSe nanoplatelets mixed with hexagonal boron nitride and impregnated with 16 mM TEKPol solution in TCE. The ^{77}Se transverse magnetization is excited using ^{1}H→^{77}Se CPMAS transfer. A structural model of the surface of CdSe nanoplatelets along with the observed connectivities is shown on the left of the figure. Figure adapted from ref. [167]. Copyright, 2021, American Chemical Society.

3.1.2 Between spin-1/2 and half-integer quadrupolar isotopes

3.1.2.1 *Without high-resolution*

J-RINEPT and *J*-HMQC experiments have also been used to probe connectivities between spin-1/2 and half-integer quadrupolar isotopes in inorganic solids. The employed pulse sequences are identical to those used to correlate the signals of spin-1/2 isotopes, except that CT-selective pulses are applied to the quadrupolar nuclei. Furthermore, when the excited nucleus is half-integer quadrupolar nucleus, the signal intensity can be enhanced by irradiating the STs at the beginning of the sequence, in such way that the population difference across the CT is increased [168]. When the T_2' time constant is much longer than that of the apparent decay of the transverse magnetization, T_2^*, the signal intensity can be enhanced by the acquisition of a train of echoes using CPMG scheme for spin-1/2 nuclei or the quadrupolar CPMG (QCPMG) variant for half-integer quadrupolar nuclei, in which 180° pulses are CT-selective [169,170]. When half-integer quadrupolar nuclei are indirectly detected using *J*-HMQC sequence, the losses can be reduced by accelerating the coherence transfer through the irradiation of STs during the τ delays [171,172]. DNP has been recently employed to enhance the sensitivity of *J*-RINEPT experiments in order to probe connectivities of surface sites [81].

As seen in Table 1 and Table *2*, the *J*-RINEPT and *J*-HMQC experiments have been applied for several spin-1/2 isotopes, including ^{1}H, ^{13}C, ^{19}F, ^{29}Si, ^{31}P and ^{77}Se, as well as a few half-integer quadrupolar nuclei, such as ^{11}B, ^{17}O, ^{27}Al, ^{51}V and ^{71}Ga. An example of 2D ^{19}F{^{27}Al} *J*-HMQC spectrum allowing the observation of ^{19}F-^{27}Al covalent bonds is shown in Figure 14. These experiments have been demonstrated for isotopes with high or moderate gyromagnetic ratio, since the strength of the *J*-coupling increases with increasing gyromagnetic ratios. Furthermore, the *J*-coupling constants usually decrease when the number of bonds between the coupled nuclei increases. Isotopic enrichment and/or DNP are often required to detect connectivities of isotopes with low natural abundance, such as ^{17}O (0.0373%) and ^{29}Si (4.67%). Heteronuclear correlation experiments between isotopes exhibiting close Larmor frequencies, such as ^{13}C and ^{27}Al, for which these frequencies are only 3.6% apart, are not possible with conventional MAS NMR probes and require the use of a frequency splitter [173,174].

Table 1. List of the pairs of spin-1/2 and quadrupolar isotopes, between which covalent bonds have been probed by 2D *J*-RINEPT or *J*-HMQC experiments in hybrid or inorganic solids.

$I = 1/2^a$	$S \geq 1/2^a$	$^1J_{IS}$ /Hz	2D experiments	Sample	Ref.
^{1}H	^{27}Al	376	*J*-HMQC	Al hydride on γ-Al_2O_3	175
^{13}C	^{27}Al	71	*J*-HMQC	alkylaluminium	174
^{19}F	^{11}B	-[b]	*J*-HMQC	fluoroborosilicate glass	176
^{19}F	^{27}Al	-[b]	*J*-HMQC	fluorinated aluminophosphate	128
^{29}Si	^{17}O	23-34	*J*-HMQC	silica	168
^{31}P	^{17}O	120-130	*J*-HMQC	$Na_5P_3O_{10}$ crystals	177
^{77}Se	^{71}Ga	500-800	*J*-RINEPT	gallium selenide crystal and glass	170
			J-HMQC		

[a] In this table, the *I* and *S* symbols do not denote the indirectly detected and spy isotopes, contrary to Figure 9 and Figure 11. [b] Not measured.

Table 2. List of the pairs of spin-1/2 and quadrupolar isotopes, between which two-bond connectivities have been probed by 2D *J*-RINEPT or *J*-HMQC experiments in hybrid or inorganic solids.

$I = 1/2^a$	$S \geq 1/2^a$	$^2J_{IS}$ /Hz	2D experiments	Sample	Ref.
^{29}Si	^{11}B	-[b]	*J*-HMQC	layered borosilicates	178
^{29}Si	^{27}Al	1-6	DNP+*J*-RINEPT	silicated alumina	81
			J-HMQC	aluminosilicate glasses	179
^{31}P	^{11}B	-[b]	*J*-HMQC	borophosphate glass	180
^{31}P	^{27}Al	15-25	*J*-RINEPT	aluminophoshate crystals	17
			J-HMQC	aluminophoshate crystals	160
^{31}P	^{51}V	40	*J*-HMQC	$Pb_4(VO_2)(PO_4)_3$	181
^{31}P	^{71}Ga	12	*J*-HMQC	gallophosphate crystal	182

[a] In this table, the *I* and *S* symbols do not denote the indirectly detected and spy isotopes, contrary to Figure 9 and Figure 11. [b] Not measured.

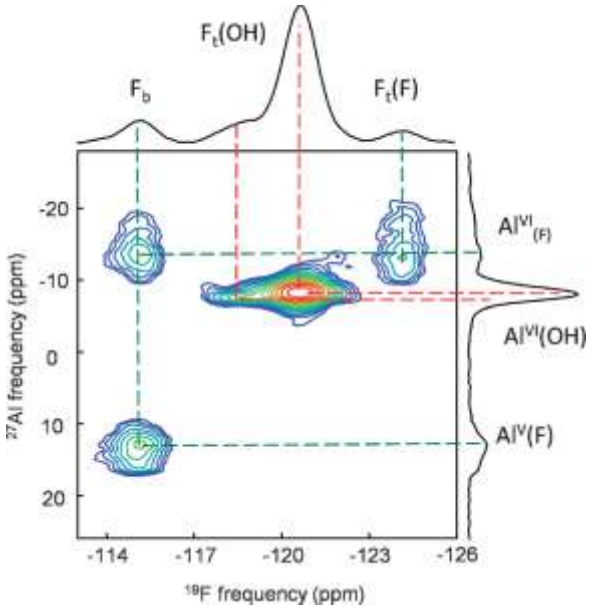

Figure 14. 2D ^{19}F{^{27}Al} *J*-HMQC spectrum of crystalline fluorinated aluminophosphate $AlPO_4$-CJ2 at B_0 = 9.4 T with ν_R = 10 kHz. This spectrum allows probing ^{19}F-^{27}Al covalent bonds and hence, the local OH/F distribution in this material. Figure adapted from ref. [128]. Copyright, 2011, Royal Society of Chemistry.

3.1.2.2 *With high-resolution*

In 2D *J*-RINEPT and *J*-HMQC spectra, the signals of quadrupolar nuclei are broadened by second-order quadrupolar interaction [183,184]. This broadening, which can mask differences in isotropic chemical shifts, can be removed using 2D MQMAS scheme, which combines the evolution of multiple-quantum and 1Q coherences [185,186]. These 1Q coherences of the quadrupolar isotope at the end of the MQMAS block can be transferred to spin-1/2 nucleus via *J*-coupling using *J*-RINEPT sequence, as shown in Figure 15, which displays the sequence of 3Q-*J*-RINEPT experiment [21,187]. The sensitivity of this experiment can be enhanced by the use of soft pulse added mixing (SPAM), i.e. the insertion of a 90° CT-selective pulse after the reconversion pulse of the MQMAS block [187]. The 3Q-*J*-RINEPT sequence has been applied to acquire 2D ^{31}P{^{27}Al} and ^{29}Si{^{27}Al} through-bond correlation spectra of aluminophosphate and aluminosilicate materials, respectively, with high-resolution along the ^{27}Al dimension (see Figure 16). High-resolution *J*-HMQC spectra can also be acquired by substituting the initial CT-selective 90° pulse on the *S* channel (see Figure 11) by a MQMAS block exciting 3Q coherences of the detected quadrupolar isotope [188]. Nevertheless, this experiment requires a 3D acquisition, instead of a 2D one for 3Q-*J*-RINEPT technique.

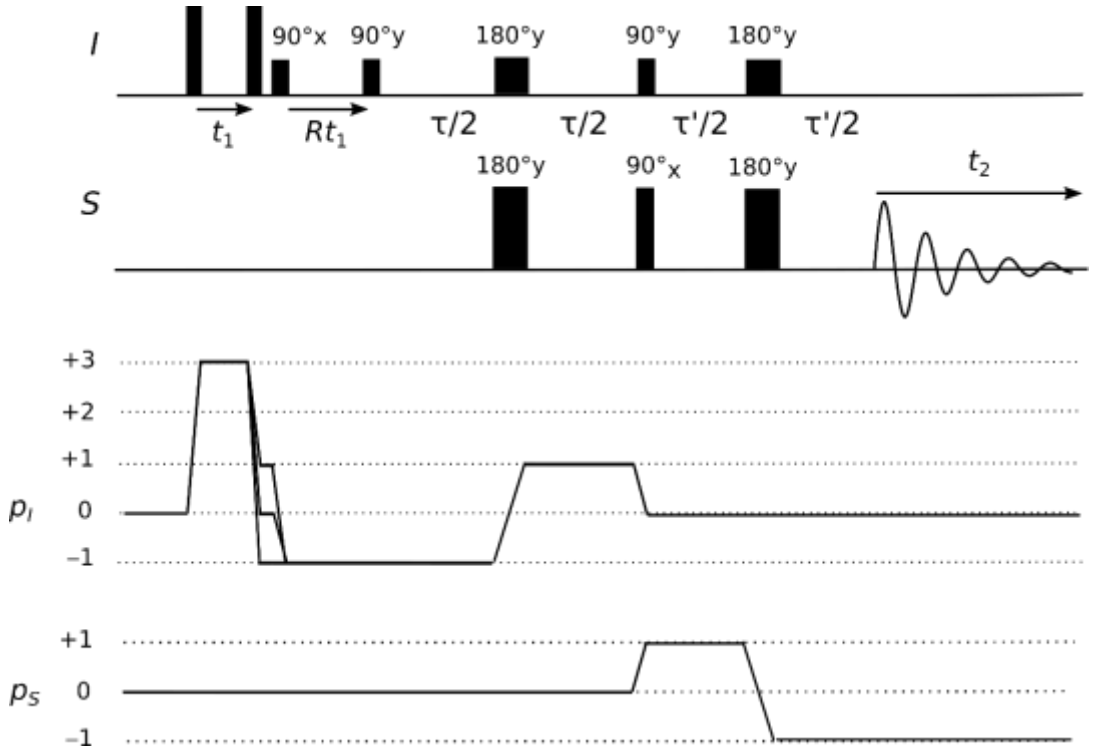

Figure 15. Pulse sequence along with desired coherence transfer pathways of 2D *S*{*I*} 3Q-*J*-RINEPT experiment for $I \geq 5/2$. The first pulse on *I* channel employs high rf power to excite the 3Q coherences. The second and third pulses on this channel corresponds to the SPAM block, whereas the other pulses are selective of the CT.

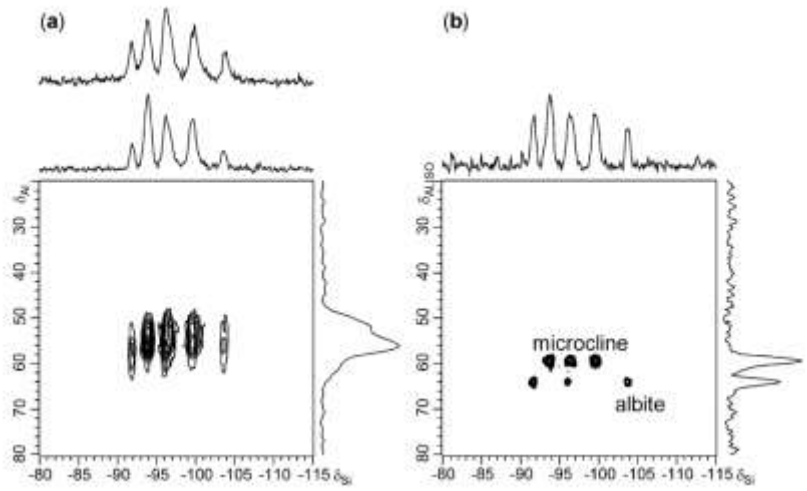

Figure 16. Comparison of 2D ^{29}Si{^{27}Al} (a) *J*-RINEPT and (b) 3Q-*J*-RINEPT spectra of a mixture of microcline and albite aluminosilicate minerals acquired at B_0 = 9.4 T with ν_R = 10 kHz. Figure reprinted from ref. [187]. Copyright, 2006, Royal Society of Chemistry.

3.1.3 Between two half-integer quadrupolar isotopes

The ^{27}Al-^{17}O covalent bonds in ^{17}O-enriched aluminate glass and alumina have been observed using 2D ^{27}Al{^{17}O} *J*-HMQC experiment based on one-bond ^{17}O-^{27}Al *J*-couplings, as seen in *Figure 17*[19,172]. The sensitivity of this experiment has been improved by the irradiation of ^{27}Al STs at the beginning of the sequence to enhance the population difference across the CT, but also the irradiation of ^{17}O STs during the defocusing and refocusing delays to accelerate the coherence transfers, and hence, to reduce the losses during this delay [172]. These losses can also be limited by spinning slightly off the magic angle, which lengthens the T_2' time constant of the ^{27}Al and ^{17}O nuclei [189].

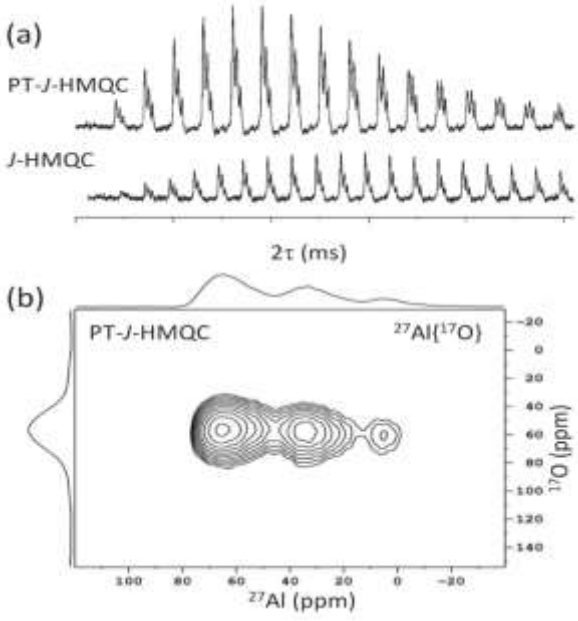

Figure 17. (a) Build-up of the signal of 1D ^{27}Al{^{17}O} population transfer (PT)-*J*-HMQC and *J*-HMQC experiment of ^{17}O-enriched γ-Al_2O_3 sample. In PT-*J*-HMQC variant, the ^{17}O STs are irradiated during the defocusing and refocusing delays, τ, which accelerates the coherence transfer by approximately a factor of 2 and hence, reduces the losses. (b) 2D ^{27}Al{^{17}O} PT-*J*-HMQC of the same sample. The spectra are acquired at B_0 = 18.8 T with ν_R = 20 kHz. Figure reprinted from ref. [172]. Copyright, 2015, American Institute of Physics.

3.2 *Through-space heteronuclear correlations*

Coherence transfers based on heteronuclear dipolar couplings can be used to acquire 2D heteronuclear correlation spectra. These through-space heteronuclear correlation complement their through-bond counterparts. Furthermore, for isotopes in the first periods of the periodic table, the heteronuclear dipolar couplings are usually larger than the *J*-couplings, which results in faster coherence transfers and hence, higher sensitivity. Like the through-bond heteronuclear correlation, the through-space variants have been applied for pairs of spin-1/2 isotopes, pairs of spin-1/2 and quadrupolar isotopes as well as pairs of half-integer quadrupolar nuclei.

3.2.1 Between spin-1/2 isotopes

The NMR signals of distinct spin-1/2 nuclei distant by a few angstroms have been mainly correlated using 2D heteronuclear correlation (HETCOR) sequence based on CP transfer [5]. This CP-HETCOR sequence shown in Figure 19 is a direct detection method employing a single $I \rightarrow S$ polarization transfer. The 90° pulse on the *I* channel creates transverse magnetization of the *I* nuclei, which is encoded by the isotropic chemical shift during the t_1 period. This magnetization is then transferred to the *S* spin by CP during the contact time, τ_{CP}. This CP transfer relies on the simultaneous rf irradiation of *I* and *S* isotopes. These rf fields lock the transverse magnetization of the two isotopes along a particular direction in the rotating frame. The CP transfer is effective provided the nutation frequencies of the *I* and *S* isotopes, denoted ν_{1I} and ν_{1S} hereafter, fulfill the Hartmann-Hahn conditions under MAS conditions:

$$\nu_{1I} + \varepsilon\nu_{1S} = n\nu_R \quad (1)$$

where the coefficient ε is equal −1 for the 0Q-CP and +1 for 2Q-CP and $n = \pm 1$ or ± 2 [190,191]. The terms 0Q-CP and 2Q-CP are related to the rank of the spin operator in the Hamiltonian of the recoupled dipolar interaction [191,192]. At slow MAS, the 0Q-CP condition is preferred, whereas at fast MAS, both 0Q-CP and 2Q-CP can be employed. The most efficient CP transfer is usually achieved for $n = \pm 1$. As most NMR coils produce inhomogeneous rf field, the Hartmann-Hahn condition is only fulfilled in a limited region of the sample volume. Hence, the rf field applied to *I* or *S* isotope is usually linearly swept so that the different regions of the sample contribute to the detected signal and hence, the signal intensity is enhanced. The optimal τ_{CP} time depends on the *I*-*S* dipolar coupling and the relaxation during the spin locks. After the CP transfer, the free-induction decay (FID) of the *S* nuclei is detected during the t_2 period. If necessary, notably when *I* = ^{1}H, the broadening of NMR signals of *S* nuclei due to residual dipolar couplings with *I* spin can be removed by applying heteronuclear dipolar decoupling sequence during the t_2 period. The sensitivity of CP-HETCOR experiments can be enhanced by using CPMG detection, when $T_2'(S) >> T_2^*(S)$, notably for *S* = ^{29}Si [193], and DNP [84]. Table 3 lists pairs of spin-1/2 isotopes, for which 2D HETCOR spectra have been recorded using direct detection.

Table 3. List of the pairs of distinct spin-1/2 isotopes, for which their signals have been correlated using direct detection methods. Except 2D ^{13}C{^{29}Si} HETCOR spectrum, for which TEDOR transfer was employed, other HETCOR experiments were recorded using CP transfer.

I	*S*	DNP	Sample	Ref.
^{1}H	^{13}C	no	mesoporous aluminosilicates	194
^{1}H	^{15}N	no	silica-supported Ta complexes	195
^{1}H	^{19}F	no	fluorohectorite	196
^{1}H	^{29}Si	no	amorphous hydrogenated silicon	6
^{1}H	^{31}P	no	phosphate crystals and glasses	197,198
^{1}H	^{89}Y	yes	Y-doped $BaZrO_3$	199
^{1}H	^{113}Cd	yes[a]	CdS nanoparticles	200

^{1}H	^{119}Sn	yes	Sn/SnOx nanoparticles	201
^{19}F	^{29}Si	no[a]	functionalized mesoporous silica	202
^{19}F	^{31}P	no	fluorinated aluminophosphate	203
^{29}Si	^{13}C	yes[b]	organically functionalized silicon nanoparticles	91
^{31}P	^{13}C	yes	zirconium phosphate nanoparticles	204
^{31}P	^{29}Si	no	silicophosphate	205

[a] Using CPMG detection. [b] Using TEDOR-HETCOR.

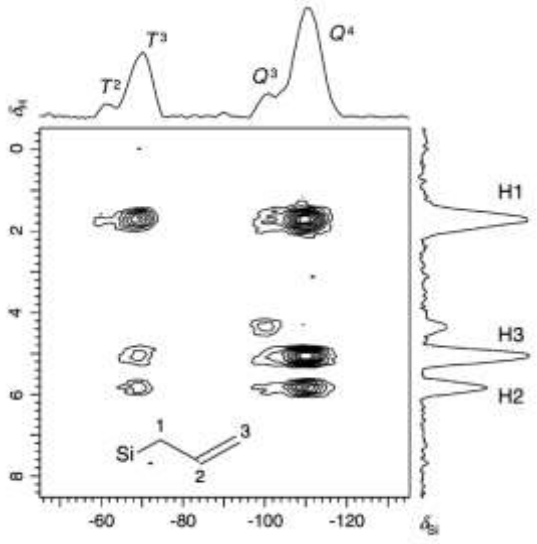

Figure 18. 2D ^{29}Si{^{1}H} CP-HETCOR-CPMG spectrum of mesoporous silica nanoparticles functionalized with allyl groups acquired at B_0 = 14.1 T with ν_R = 40 kHz. Because of the CPMG detection, this direct detection experiment is more sensitive than indirect detection via protons. Figure adapted from ref. [90]. Copyright, 2008, Elsevier.

Nevertheless, CP transfer has some limitations. In the case of CP-HETCOR experiment with protons, a first drawback is that ^{1}H spin diffusion during τ_{CP} can exchange transverse magnetization between protons, which results in relayed correlation and may prevent the observation of proximities between a given nucleus and its nearest protons. This issue is particularly acute for long τ_{CP} delay and hence, notably for small heteronuclear dipolar couplings. It can be circumvented using Lee-Goldburg CP (LG-CP), which averages out ^{1}H-^{1}H dipolar interaction during the CP transfer and hence, the ^{1}H spin diffusion [206,207]. This technique has been first introduced to record ^{13}C{^{1}H} CP-HETCOR spectra of organic solids, and then has been applied to acquire ^{31}P{^{1}H} CP-HETCOR spectra of phosphate materials [208,209].

Another drawback of CP transfer is the requirement to fulfill the Hartmann-Hahn condition. These conditions are narrower for small hetero- and homo-nuclear dipolar interactions as well as at high MAS frequencies. In particular, CP transfer involving isotopes other than ^{1}H and ^{19}F exhibits narrow Hartmann-Hahn conditions. Furthermore, the optimization of the rf field strength to fulfill the Hartmann-Hahn condition is only feasible in the case of sensitive CPMAS experiment. Therefore, for HETCOR experiments, which do not involve protons or ^{19}F, an alternative to CPMAS is the use of transferred-echo, double-resonance (TEDOR) scheme, which derives from RINEPT transfer [210]. In TEDOR scheme, a rotational-echo, double-resonance (REDOR) recoupling [211] is applied to one of the two isotopes during the defocusing and refocusing delays to reintroduce the *I-S* dipolar couplings. The REDOR recoupling consists of a train of 180° pulses and hence, is easier to optimize than CPMAS transfer. Furthermore, contrary to CP, TEDOR recoupling is not affected by dipolar truncation and hence, is more efficient for long-range polarization transfer [36,212]. For instance, DNP-enhanced TEDOR

experiment has been employed to acquire 2D $^{13}C\{^{29}Si\}$ through-space HETCOR spectrum of functionalized silicon nanoparticles [91].

For HETCOR experiments between protons and another isotope, the resolution along the ^{1}H dimension is improved by fast MAS, with $\nu_R \geq 40$ kHz [193]. Under lower MAS frequencies, the resolution of ^{1}H signals can also be increased by the application of homonuclear dipolar decoupling sequences, such as frequency-switched Lee-Goldburg (FSLG), on the ^{1}H channel during the t_1 period [213]. Nevertheless, fast MAS is more robust and is easier to set up.

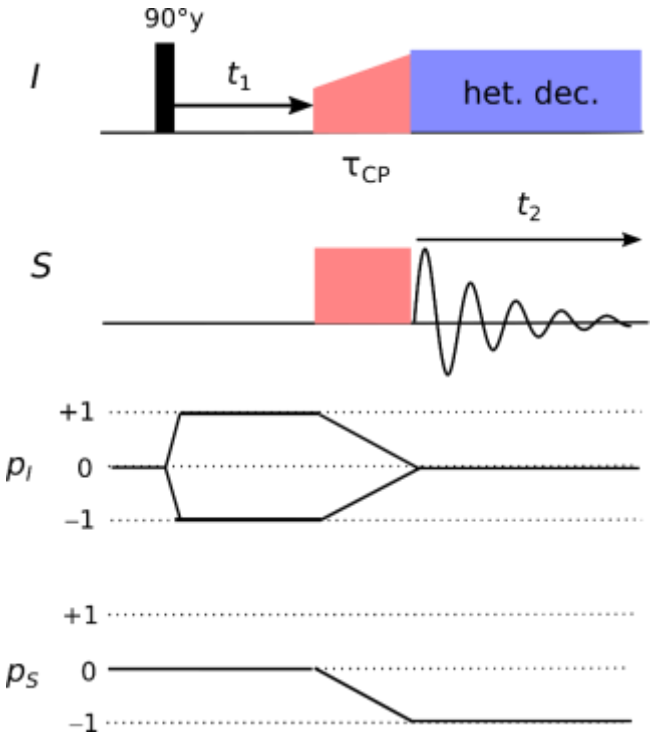

Figure 19. Pulse sequence along with desired coherence transfer pathways of $S\{I\}$ CP-HETCOR experiment. During the CP transfer, the rf field applied to the I isotope is linearly ramped.

In addition, under fast MAS, indirect detection via nuclei with high gyromagnetic ratio, such as ^{1}H or ^{19}F, usually improves the sensitivity, in spite of the lower sample volume of rotors with small diameter [32,214]. Pairs of distinct spin-1/2 isotopes, for which their NMR signals have been correlated using indirect detection methods, are listed in Table 4. For instance, it has been shown that the sensitivity for the detection of ^{13}C nuclei at the surface of organically functionalized mesoporous silica can be enhanced by a factor of 3 through the indirect detection nuclei via protons using double CP (DCP) scheme displayed in

Figure 20a [164,215]. In this scheme, the transverse magnetization of the excited nuclei, S, is transferred to the I isotope using a first CP transfer. Then a 90° pulse stores the generated transverse magnetization of the I nuclei along the B_0 field direction, while the remaining S magnetization is destroyed by saturation blocks. For $S = {}^{1}H$ or ^{19}F, an efficient saturation can be achieved by rf irradiation with $\nu_1 = \nu_R/2$ corresponding to the HORROR condition, which reintroduces the S-S dipolar interaction [214]. The second 90° pulse on the I channel converts the longitudinal magnetization of I nuclei into transverse magnetization, which is encoded by the isotropic chemical shift during the t_1 period. Finally a second $I \rightarrow S$ CP transfer reconverts the transverse magnetization of the I nuclei into transverse magnetization of S nuclei, which is detected during the t_2 period. The DCP scheme has been applied for the indirect detection of ^{13}C and ^{15}N nuclei via protons at the surface of organically functionalized mesoporous silica (see Figure 21) [164,215,216]. The ^{19}F nuclei have also been used as spy spin for the

indirect detection of ^{13}C nuclei using DCP scheme in the case of mesoporous silica functionalized with fluorinated organic moieties [202]. More recently, DCP sequence has been employed for the indirect detection via protons of low-γ spin-1/2 isotopes, including ^{89}Y, ^{103}Rh and ^{183}W, in inorganic and hybrid materials [217] as well as ^{31}P nuclei in phosphane/borane [218]. The sensitivity of DCP experiment with ^{1}H detection has also been enhanced using DNP [200].

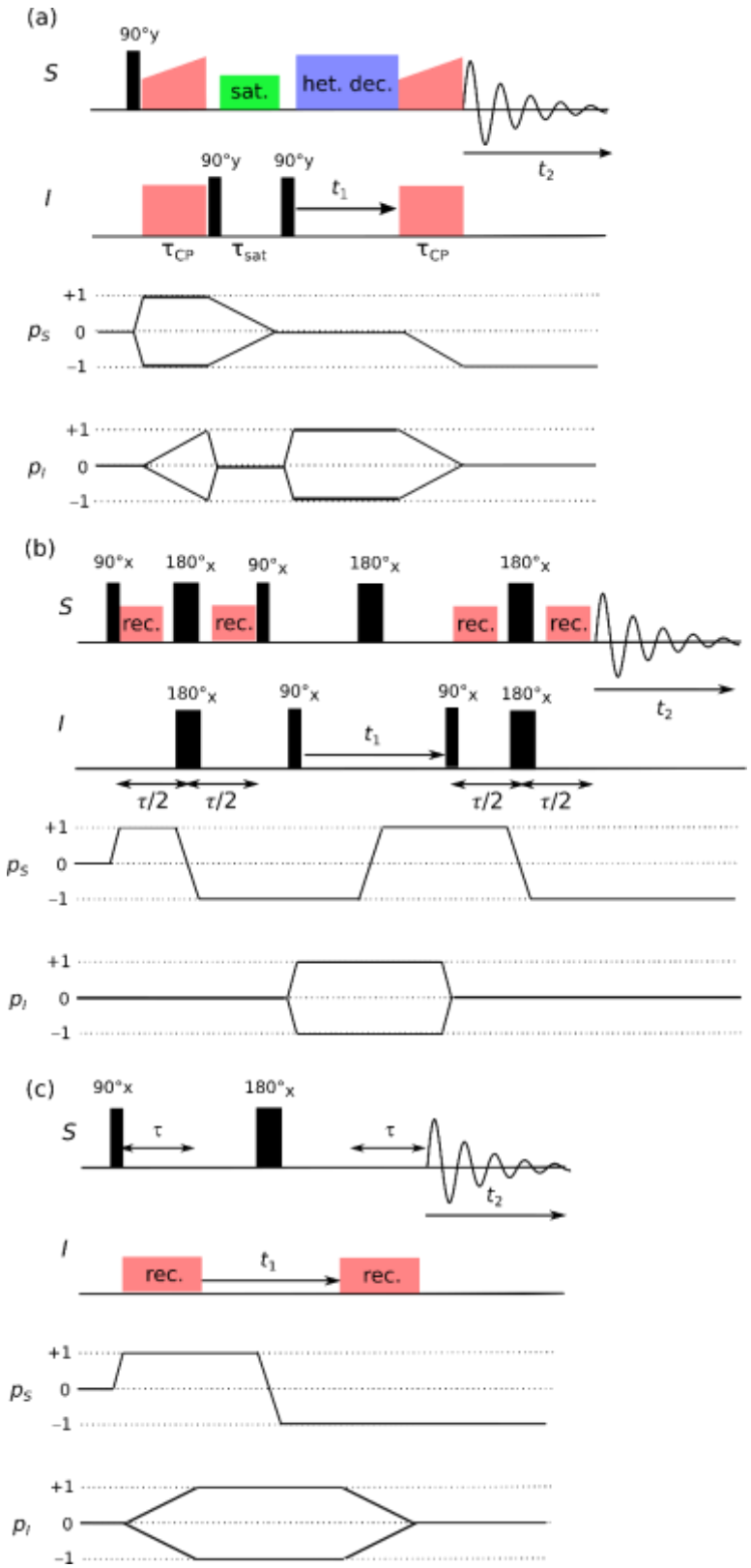

Figure 20. Pulse sequences along with desired coherence transfer pathways for the indirect detection of *I* nuclei via *S* spins: *S*{*I*} (a) DCP, (b) TONE-2-*D*-HMQC and (c) T-HMQC schemes.

Like the 2D CP-HETCOR spectra, 2D DCP ones with $S = {}^{1}H$ can exhibit relayed correlations owing to ^{1}H spin diffusion during the second CP transfer. This problem is more pronounced for long contact times, like in the case of low-γ *I* isotopes subject to small dipolar couplings with protons. Therefore, DCP variant using LG-CP scheme during the $I \rightarrow {}^{1}H$ transfer has been introduced to suppress ^{1}H spin diffusion and relayed correlation [219]. As mentioned above, a limitation of CP transfer is the need to optimize the rf field amplitudes in order to fulfill one of the Hartmann-Hahn condition. This issue can be circumvented by substituting in DCP sequence the CP transfers by $^{1}H \rightarrow I$ and $I \rightarrow {}^{1}H$ dipolar-mediated RINEPT (*D*-RINEPT) schemes, which derive from *J*-RINEPT sequences shown in Figure 9 but heteronuclear dipolar recoupling blocks are applied on ^{1}H channel during the τ delays to reintroduce the ^{1}H-*S* dipolar couplings [217]. Nevertheless, the efficiency of this double *D*-RINEPT sequence was still lower than that of DCP for the employed $SR4_1^2$ heteronuclear dipolar recoupling [220].

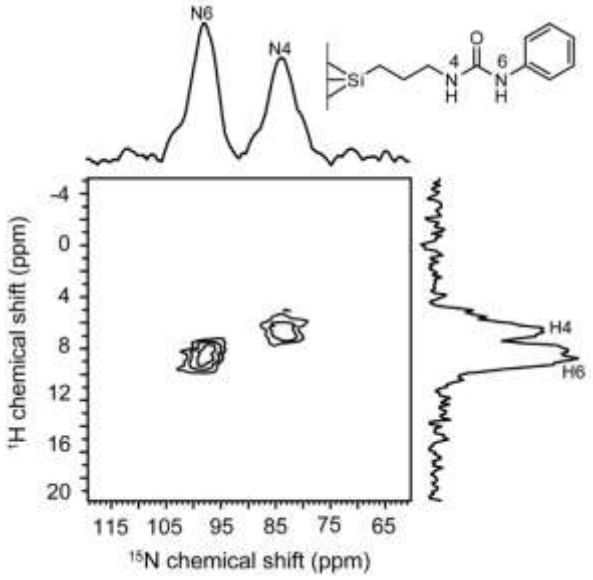

Figure 21. 2D $^{1}H\{^{15}N\}$ DCP spectrum of isotopically unmodified mesoporous silica nanoparticles functionalized with 3-(3-phenyl ureido)propyl groups (see the structure displayed as an inset) acquired at $B_0 = 14.1$ T with $\nu_R = 40$ kHz in 46 h. Figure adapted from ref. [216]. Copyright, 2014, Elsevier.

Another drawback of DCP technique is the limited excitation bandwidth of the CP transfer owing to the use of long spin-lock irradiation. As a result, DCP sequence is not applicable for isotopes subject to large CSA, such as ^{113}Cd or ^{195}Pt. For instance, the CSA of ^{195}Pt nuclei can exceed 7000 ppm, leading to spectral breadth of 500 kHz at $B_0 = 9.4$ T [221]. An alternative for the indirect detection of ^{195}Pt nuclei via protons relies on the use of dipolar-mediated HMQC (*D*-HMQC) sequence, which derives from the *J*-HMQC scheme shown in Figure 11 but ^{1}H-^{195}Pt dipolar couplings are reintroduced during the τ delays by the application of heteronuclear dipolar recoupling schemes, such as $SR4_1^2$, on the *I* channel [24,222]. The *D*-HMQC sequence has been combined with magic-angle turning (MAT) scheme to refocus ^{195}Pt CSA during the t_1 period and correlate the ^{1}H signal with ^{195}Pt centerband [223]. The *D*-HMQC experiment has also been used for the indirect detection of ^{111}Cd and ^{113}Cd nuclei via ^{13}C and ^{31}P isotopes near the surface of CdSe and Cd_3P_2 nanoparticles [91,224].

Nevertheless, a limitation of the basic *D*-HMQC scheme is the t_1-noise, which produces spurious streaks along the indirect spectral dimension and hence, reduces the sensitivity. These artefacts stem from the random fluctuations of the MAS frequencies, which prevent a correct refocusing of the ^{1}H

CSA reintroduced by the $SR4_1^2$ blocks at the end of the defocusing delay, and result in signal amplitude variation from scan to scan [225]. As a result, the uncorrelated signal is not perfectly canceled by the phase cycling, which leads to t_1-noise. It has been shown that the t_1-noise can be decreased by refocusing the ^{1}H CSA during the τ delays by inserting two simultaneous 180° pulses on the ^{1}H and *I* channels in the middle of these delays. For *I* = ^{195}Pt, short high-powered adiabatic (SHAP) pulses can be employed as 180° pulses [226,227]. Hence, these t_1-noise-eliminated (TONE) *D*-HMQC experiments must be preferred for the indirect detection via protons of spin-1/2 isotopes subject to large CSA. Furthermore, in the TONE-2-*D*-HMQC variant shown in

Figure *20*b, a 90° pulse at the end of the defocusing delay flips back the uncorrelated ^{1}H magnetization along the B_0 field direction, thus reducing the intensity of the uncorrelated signal and that of the t_1-noise. The TONE-*D*-HMQC experiments have been applied for the indirect detection via protons of ^{195}Pt nuclei of platinum complexes grafted on silica surfaces [227,228]. This sequence has also been combined with MAT to suppress the spinning sidebands of ^{195}Pt nuclei and to correlate the ^{1}H NMR signal only with its centerband [228]. Furthermore, we recently showed that ^{195}Pt nuclei can be indirectly detected via protons in solids using T-HMQC sequence shown in

Figure 20c, in which the ^{1}H-^{195}Pt dipolar interactions are reintroduced during the τ delay by the application of long rf pulses on ^{195}Pt channel [229]. These long pulses also excite and reconvert ^{195}Pt 1Q coherences, which are encoded by the isotropic chemical shifts during the t_1 period. Since the long pulses are applied to the ^{195}Pt channel, they do not reintroduce the ^{1}H CSA and hence, the 2D ^{1}H{^{195}Pt} T-HMQC spectra exhibit low t_1-noise (see Figure 22).

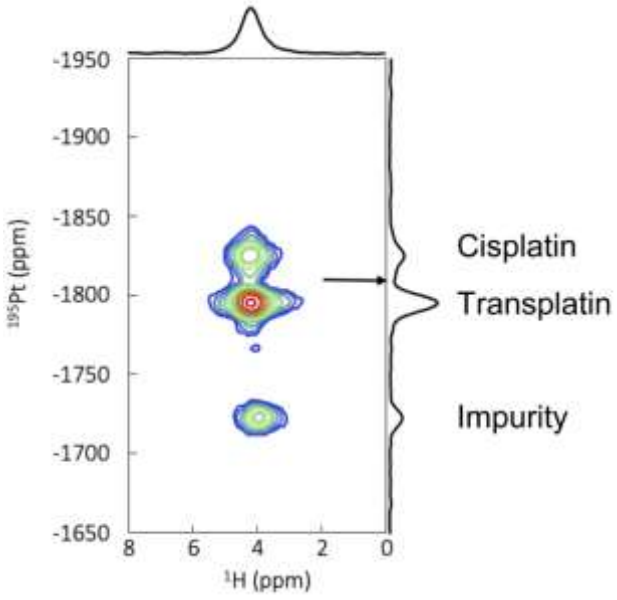

Figure 22. 2D ^{1}H{^{195}Pt} T-HMQC spectrum of an aged mixture of trans- and cis-platin acquired at B_0 = 18.8 T with ν_R = 64 kHz. Figure adapted from ref. [229]. Copyright, 2022, American Institute of Physics.

Table 4. List of the pairs of distinct spin-1/2 isotopes, for which their signals have been correlated using indirect detection methods employing two consecutive coherence transfers $S \rightarrow I \rightarrow S$.

S	*I*	Sequence	Sample	Ref.
^{1}H	^{13}C	DCP	organically functionalized mesoporous silica	215
^{1}H	^{15}N	DCP	organically functionalized mesoporous silica	216
^{1}H	^{31}P	DCP	phosphane/borane	218
^{1}H	^{89}Y	DCP	yttrium complex	217

^{1}H	^{89}Y	DNP+DCP	Y_2O_3 nanoparticles	200
^{1}H	^{103}Rh	DCP	Rh complex	217
^{1}H	^{103}Rh	double *D*-RINEPT	Rh complex	217
^{1}H	^{113}Cd	DNP+DCP	CdS nanoparticles	200
^{1}H	^{119}Sn	*D*-HMQC	Sn-β zeolite	230
^{1}H	^{183}W	DCP	$(NH_4)_2WS_4$	217
^{1}H	^{183}W	double *D*-RINEPT	$(NH_4)_2WS_4$	217
^{1}H	^{195}Pt	*D*-HMQC	cisplatin and transplatin	24,222
		TONE-*D*-HMQC	silica-supported Pt complexes	227,228
		T-HMQC	cisplatin and transplatin	229
^{19}F	^{13}C	DCP	functionalized mesoporous silica	202
^{31}P	^{113}Cd	*D*-HMQC	Cd_3P_2 nanoparticles	91

3.2.2 Between spin-1/2 and quadrupolar isotopes

3.2.2.1 *Without high-resolution*

Through-space heteronuclear correlation experiments relying on one ($I \rightarrow S$) or two ($S \rightarrow I \rightarrow S$) coherence transfers have also been applied to probe proximities between spin-1/2 and quadrupolar isotopes in solids [44–46,48]. In the case of half-integer quadrupolar isotopes, this correlation has been achieved first using CP-HETCOR experiment [15] and later TEDOR sequence [16], which derives from RINEPT method. Table 5 lists pairs of spin-1/2 and half-integer spin quadrupolar isotopes, which have been correlated using a single coherence transfer. The CP-HETCOR sequence is identical to that employed for spin-1/2 isotopes (see Figure 19). Nevertheless, it requires the spin locking of the magnetization of the quadrupolar isotope, which is difficult to achieve under MAS [231,232]. During the spin lock, the modulation of the quadrupolar interaction by MAS results in crossing of energy levels. Adiabatic crossings are usually difficult to achieve since they require large rf fields, which are not compatible with the rf power specifications of most NMR probes. An alternative is to spin lock the magnetization of the CT using low rf field, which results in sudden-passage energy level crossings. Nevertheless, even under these conditions, some losses often occur during the energy level crossings, which decreases the efficiency of CPMAS transfer, and the magnetization of quadrupolar nuclei cannot be spin locked for some crystallite orientations, which results in line-shape distortions [142,233,234]. Furthermore, the low rf field used to spin lock the magnetization of the CT leads to a high sensitivity to offset and CSA [232,235,236]. In addition, the CPMAS experiment requires a careful adjustment of the rf field applied to the quadrupolar isotope to fulfill the Hartmann-Hahn conditions under MAS conditions:

$$\nu_{1I} + \varepsilon\left(S + \frac{1}{2}\right)\nu_{1S} = n\nu_R \tag{2}$$

assuming the *S* spin is the quadrupolar isotope, while avoiding the rotary resonance recoupling (R^3) condition

$$\nu_{1S} = \frac{k\nu_R}{\left(S+\frac{1}{2}\right)} \tag{3}$$

with k = 0, 1, 2 or 3 [232,235].

These issues are circumvented by the use of magnetization transfer, which do not employ spin lock of the quadrupolar isotope but instead two or three CT-selective pulses. These sequences include the dipolar-mediated RINEPT (*D*-RINEPT) techniques [16,237–239], such as TEDOR, and phase-shifted recoupling effects a smooth transfer of order (PRESTO) [240–243]. In these sequences, the heteronuclear dipolar interactions are reintroduced by applying heteronuclear recoupling to the spin-1/2 isotope. In the case of spin-1/2 nuclei other than ^{1}H and ^{19}F, which are subject to small homonuclear dipolar couplings,

heteronuclear recoupling schemes, such as REDOR or R^3 with $\nu_{1I} = \nu_R$, reintroducing the $|m| = 1$ space component of the heteronuclear dipolar interaction must be employed since they result in larger recoupled dipolar interaction and hence, faster magnetization transfer [237,238]. The R^3 scheme has the advantage to be γ-encoded, which limits the t_1 noise [238].

Conversely when the spin-1/2 nuclei are subject to large homonuclear dipolar interactions, like in the case of protons, recoupling reintroducing the $|m| = 2$ space component of the heteronuclear dipolar interaction, such as those based on $SR4_1^2$ symmetry [220], are required since they suppress the contribution of homonuclear dipolar interactions to the first-order average Hamiltonian [239,244,245]. Furthermore, we have recently demonstrated that the efficiency of the *D*-RINEPT transfer from protons to half-integer quadrupolar nuclei can be improved by employing $SR4_1^2$ recoupling built from composite or adiabatic tanh/tan inversion pulses, continuous wave irradiation during the windows and composite 90° and 180° pulses on the ^{1}H channel [245–247]. These modifications limit the losses due to ^{1}H-^{1}H dipolar interactions and improve the robustness to rf field inhomogeneity. The corresponding sequence termed *D*-RINEPT-CWc is shown in Figure 23a. The use of adiabatic pulses as basic inversion element of $SR4_1^2$ recoupling provides the highest transfer efficiency and robustness at low MAS frequencies, $\nu_R \leq 15$ kHz, whereas at higher MAS frequencies, $270°_x90°_y$ composite pulse must be employed since the rf requirement of adiabatic pulses is not compatible with the specifications of MAS probes. The *D*-RINEPT sequence using $SR4_1^2$ recoupling is not affected by dipolar truncation and hence, allows the observation of both short- and long-range proximities. The $SR4_1^2$ recoupling also reintroduces the ^{1}H CSA but this term commutes with the recoupled ^{1}H-*I* dipolar interactions, and hence, does not affect the magnetization transfer.

The PRESTO sequence is an alternative to the *D*-RINEPT sequence for the transfer of magnetization from protons to half-integer quadrupolar nuclei. This sequence displayed in Figure 23b employs a symmetry-based recoupling, RN_n^ν which reintroduces the $|m| = 2$ space component and the 1Q terms of the heteronuclear dipolar interaction. $R22_2^7$ recoupling built from single 180° pulses results in good transfer efficiency and robustness at low MAS frequencies, $\nu_R \leq 20$ kHz, whereas at high MAS frequencies ($\nu_R \approx 60$ kHz), $R16_6^7$ recoupling using $270°_x90°_y$ composite pulse as a basic inversion element must be employed [244,245]. These recoupling schemes are affected by dipolar truncation and hence, PRESTO experiment complements *D*-RINEPT by allowing the selective observation of short-range proximities. These recoupling sequences also reintroduce the ^{1}H CSA, which does not commute with the recoupled ^{1}H-*I* dipolar interactions and hence, can interfere with the magnetization transfer. In the case of large ^{1}H-*I* dipolar interactions, e.g. for covalently bonded ^{1}H and *I* nuclei, and moderate ^{1}H CSA, notably at low B_0 fields, the PRESTO-II sequence with only two pulses applied to the quadrupolar isotope is generally the most efficient variant of PRESTO. Conversely the PRESTO-III scheme shown in Figure 23b results in higher efficiency in the case of small ^{1}H-*I* dipolar interactions and large ^{1}H CSA because the interference of ^{1}H CSA are limited by the application of CT-selective 180° pulse to the quadrupolar isotope and the simultaneous overall phase shift of the recoupling applied to ^{1}H channel, which refocus partly the ^{1}H CSA while preserving the recoupled ^{1}H-*I* dipolar interactions [242]. In the PRESTO sequence, the first 90° pulse excites ^{1}H transverse magnetization, which is encoded by the isotropic chemical shift during the t_1 period. The second 90° pulse flips back this transverse magnetization along the B_0 field direction. The RN_n^ν 1Q heteronuclear recoupling converts the ^{1}H longitudinal magnetization into ^{1}H 1Q coherences antiphase with respect to the quadrupolar isotope, which is transformed into 1Q coherences of the quadrupolar isotope antiphase with respect to the protons by the 90° pulse on the *S* channel. These antiphase 1Q coherences of *S* spins evolves during the refocusing delay into in-phase transverse magnetization, which is detected during the t_2 period.

The sensitivity of 2D PRESTO experiments has been improved using DNP and QCPMG detection to correlate the signals of ^{1}H and ^{17}O isotopes in natural abundance (see Figure 24) [240,248].

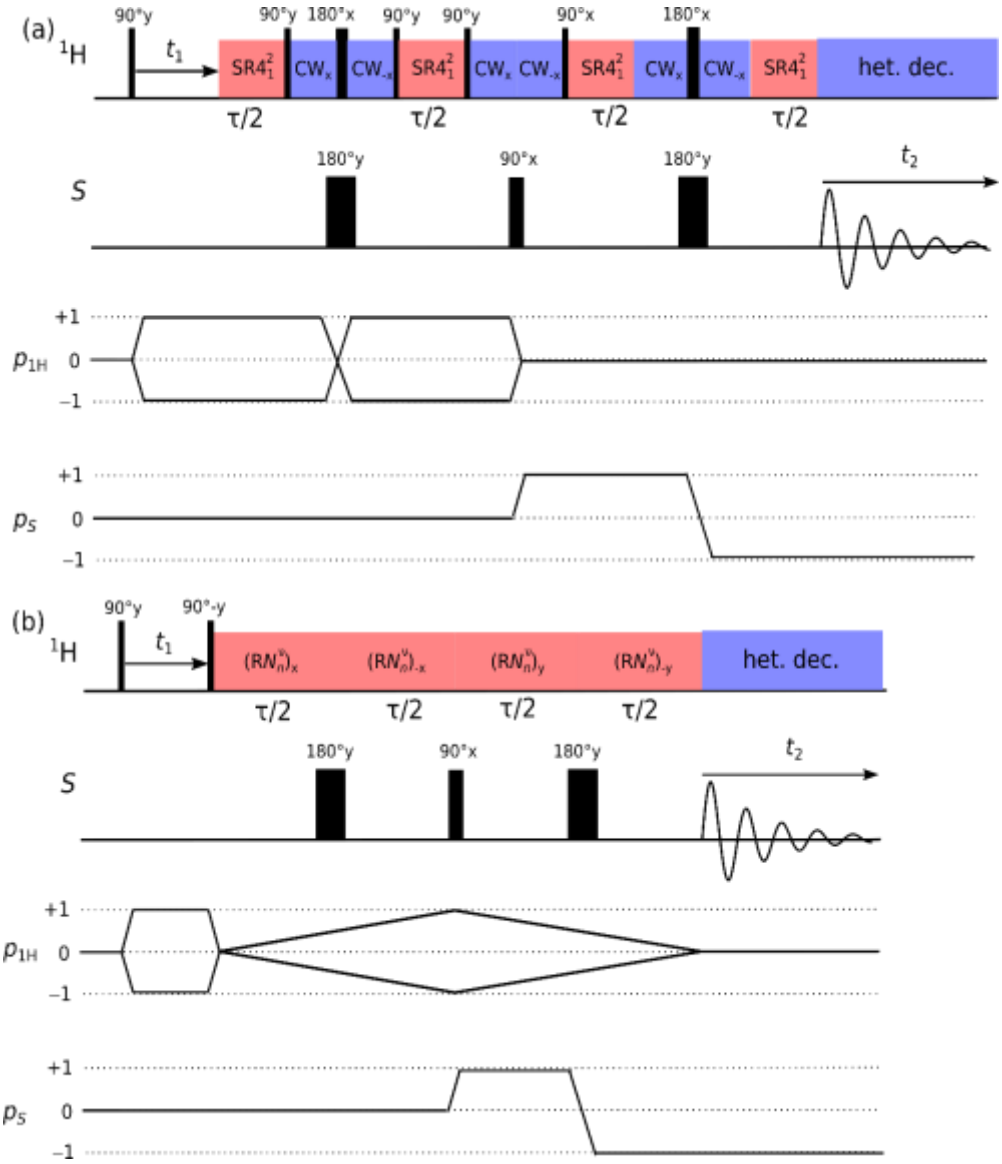

Figure 23. Pulse sequences along with desired coherence transfer pathways for (a) *D*-RINEPT-CWc using $SR4_1^2$ recoupling and (b) PRESTO-III using RN_n^ν recoupling.

The ^{1}H resolution of heteronuclear correlation spectra between protons and quadrupolar isotopes is improved at high MAS frequencies ($\nu_R \geq 40$ kHz) [245]. At lower MAS frequencies, the resolution can be enhanced by the application of homonuclear dipolar decoupling, such as FSLG, on ^{1}H channel during the t_1 period [240]. However, fast MAS is easier to set up and more robust than the homonuclear decoupling.

Table 5. List of the pairs of spin-1/2 and half-integer quadrupolar isotopes, which have been correlated using single coherence transfer $I \rightarrow S$.

I	*S*	Sequence	Sample	Ref.
^{1}H	^{17}O	CP-HETCOR	zeolites	249
		DNP+PRESTO-II	$Mg(OH)_2$ and $Ca(OH)_2$	240
^{1}H	^{43}Ca	DNP+CPMAS	hydroxyapatite nanoparticles	250
^{11}B	^{1}H	CP-HETCOR	borosilicate zeolite	251

^{11}B	^{29}Si	CP-HETCOR	borosilicate glass	252
^{11}B	^{31}P	CP-HETCOR	borophosphate glass	253
^{17}O	^{29}Si	CP-HETCOR	^{17}O-enriched silicate glass	254
^{19}F	^{27}Al	CP-HETCOR	fluorinated aluminophosphate	203
^{27}Al	^{1}H	CP-HETCOR	mesoporous aluminosilicate	194
		D-RINEPT-R^3	crystalline aluminophosphate $AlPO_4$-14	237
		D-RINEPT- $SR4_1^2$	γ-alumina	239
^{27}Al	^{23}Na	*D*-RINEPT-R^3	crystalline aluminophosphate	237
^{27}Al	^{29}Si	TEDOR	zeolites	255
^{27}Al	^{31}P	CP-HETCOR	crystalline aluminophosphate VPI-5	16
		CP-HETCOR	aluminophosphate glass	256
		D-RINEPT-R^3	crystalline aluminophosphate $AlPO_4$-14	237

As mentioned above, the choice of the excited and detected isotopes in heteronuclear correlation depend on the gyromagnetic ratios, longitudinal relaxation times, T_1, coherence lifetimes and line widths of the correlated nuclei [32,239]. In the case of heteronuclear correlation experiment between spin-1/2 and half-integer quadrupolar isotopes relying on a single coherence transfer, the highest sensitivity is often achieved by exciting the quadrupolar isotope, which exhibits faster longitudinal relaxation than spin-1/2 nuclei. Furthermore, the sensitivity can be further improved by irradiating the STs at the beginning of the sequence to enhance the population difference across the CT [257]. Nevertheless, in the case of DNP experiments, higher sensitivity is usually achieved by exciting the protons since the ^{1}H-^{1}H spin diffusion efficiently transports the DNP-enhanced ^{1}H polarization into the sample [258,259].

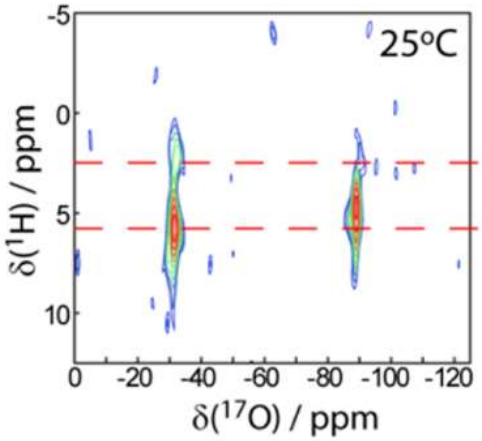

Figure 24. 2D ^{17}O{^{1}H} DNP-enhanced PRESTO-II-QCPMG spectrum of isotopically unmodified mesoporous silica nanoparticles with pore diameter of 3.4 nm dried *in vacuo* at 25 °C and impregnated with 16 mM TEKPol solution in TCE. This spectrum was acquired at B_0 = 9.4 T with ν_R = 12.5 kHz. FSLG homonuclear decoupling was applied to the protons during the t_1 period to improve the spectral resolution of the ^{1}H dimension. Figure adapted from ref. [248]. Copyright, 2016, American Chemical Society.

Nevertheless, the above heteronuclear correlation experiments relying on a single coherence transfer cannot correlate the signals of protons and the 1Q coherences of ^{14}N nuclei, which are broadened over several megahertz by first-order quadrupolar interaction for this spin-1 isotope and hence, are difficult to spin lock or to invert by 180° pulse. CP-HETCOR and PRESTO-II sequences have been applied to correlate the signals of protons and ^{14}N 2Q coherences between energy levels $m_I = \pm 1$ since these coherences are only broadened by second-order quadrupolar interaction [260,261]. However, the overtone excitation and detection at twice the Larmor frequency are less efficient than those of ^{14}N 1Q coherences at the ^{14}N Larmor frequency. Therefore, through-space HMQC (*D*-HMQC) experiments have been proposed for the indirect detection of ^{14}N coherences via ^{13}C nuclei [1,2] and later protons [262]. These experiments, which derive from the *J*-HMQC scheme shown in Figure 11, are advantageous since they do not employ any spin lock or inversion pulse on ^{14}N channel. They have

been applied for the indirect detection of ^{14}N 1Q and 2Q coherences. The indirect detection of ^{14}N 1Q coherences requires an accurate adjustment of the magic angle with an accuracy better than ±0.002° and fluctuations of the MAS frequency smaller than a few hertz to refocus the first-order quadrupolar interaction. The indirect detection of ^{14}N 2Q coherences is less demanding in terms of accuracy and stability of the MAS but is often less efficient [263–266]. Coherence transfers have been mediated by first residual dipolar splitting [1,2,262], which is the sum of the *J*-coupling and the second-order quadrupole-dipole cross term. Nevertheless, it has been shown that more efficient coherence transfers can be achieved by reintroducing *S*-^{14}N dipolar couplings through the application of heteronuclear recoupling on *S* channel during the defocusing and refocusing delays [263,267,268]. When *S* = ^{1}H, the $SR4_1^2$ recoupling built from single 180° pulse is generally used [269]. Furthermore, the through-space HSQC sequence has also been employed for the indirect detection of ^{14}N coherences via protons but is less efficient than *D*-HMQC [270]. An additional challenge for these experiments is the excitation of ^{14}N coherences using rf field with amplitude of few tens of kilohertz, which is two orders of magnitude lower than the first-order quadrupolar interaction. Various schemes have been proposed but sideband selective long pulses combine good efficiency, high robustness and easy set up [266]. The indirect detection via protons of ^{14}N 1Q coherence using *D*-HMQC sequence has notably been employed to investigate host-guest interactions in MOFs [271] as well as the structure of layered aluminophosphate containing amine structure directing agents [272] (see Figure 25a). It has also been shown that the resolution along the ^{14}N dimension can be improved by applying homonuclear decoupling schemes on ^{1}H channel during t_1 period [273].

As mentioned in the section 3.2.1, a limitation of *D*-HMQC sequence is the t_1-noise produced by the random fluctuation of MAS frequency, which prevents the correct refocusing of ^{1}H CSA and results in random signal amplitude modulation. In the case of the indirect detection of ^{14}N nuclei, this issue cannot be circumvented by the use of TONE *D*-HMQC sequence, since this scheme includes 180° pulses, which are difficult to achieve for spin-1 nuclei. An alternative consists in reintroducing the ^{1}H-^{14}N dipolar interactions by applying two identical long pulses, similar to those used in transfer of population in double resonance (TRAPDOR) [274,275], during the defocusing and refocusing delays on ^{14}N channel instead of ^{1}H channel [276–279]. These pulses do not reintroduce the ^{1}H CSA, which limits the t_1-noise. We have recently shown that this combination of TRAPDOR and HMQC schemes, called T-HMQC, can allow the indirect detection of either ^{14}N 1Q or 2Q coherences with similar efficiency [229]. Furthermore, the 2Q variant benefits from slightly higher resolution. Nevertheless, to the best of our knowledge, T-HMQC experiment has so far only been applied for the indirect detection of ^{14}N nuclei in organic solids but not yet for inorganic or hybrid solids.

The *D*-HMQC experiment has also been applied to correlate the signals of spin-1/2 and half-integer quadrupolar nuclei in solids [46,236,237,280] since depending on the correlated isotopes and the sample, the $S \rightarrow I \rightarrow S$ consecutive transfers can be more sensitive than the $S \rightarrow I$ single transfer. Table 6 lists pairs of spin-1/2 and half-integer quadrupolar nuclei, which have been correlated using *D*-HMQC sequence. In that case, the recoupling scheme is applied to the spin-1/2 isotope to minimize the number of pulses applied to quadrupolar nuclei and the associated losses. The pulses applied to the quadrupolar isotope are selective of the CT. It is often preferable to detect indirectly the spin-1/2 nuclei via the quadrupolar isotope since the longitudinal relaxation of quadrupolar nuclei is often faster and the application of the recoupling on the indirect channel limits the t_1-noise. The recoupling employed in *D*-HMQC sequence reintroduces longitudinal two-spin order term (S_zI_z) of the heteronuclear dipolar interaction. Hence, the *D*-HMQC sequence is not affected by dipolar truncation and CSA interference [280]. Furthermore, it has been shown that the *D*-HMQC sequence is more efficient than the *D*-HSQC variant [281].

When the spin-1/2 isotope is not subject to large homonuclear dipolar interaction, the heteronuclear dipolar interaction can be reintroduced by the recoupling scheme with simultaneous

amplitude and frequency modulations equal to the MAS frequency (SFAM-1) [282] (see Figure 25b). This recoupling reintroduces the $|m| = 1$ space component of the heteronuclear dipolar interaction and hence, results in fast coherence transfer [280,283]. Furthermore, because of the amplitude and frequency modulations, it is more robust to offset, CSA and rf field inhomogeneity than REDOR and R^3 schemes. At low MAS frequencies, $\nu_R \leq 15$ kHz, the symmetry-based recoupling built from adiabatic tanh/tan (tt) pulses, such as $R2_1^{-1}(tt)$, benefits from higher robustness than SFAM-1 and has been applied to correlate quadrupolar nuclei with spin-1/2 nuclei subject to large CSA, such as ^{207}Pb [284].

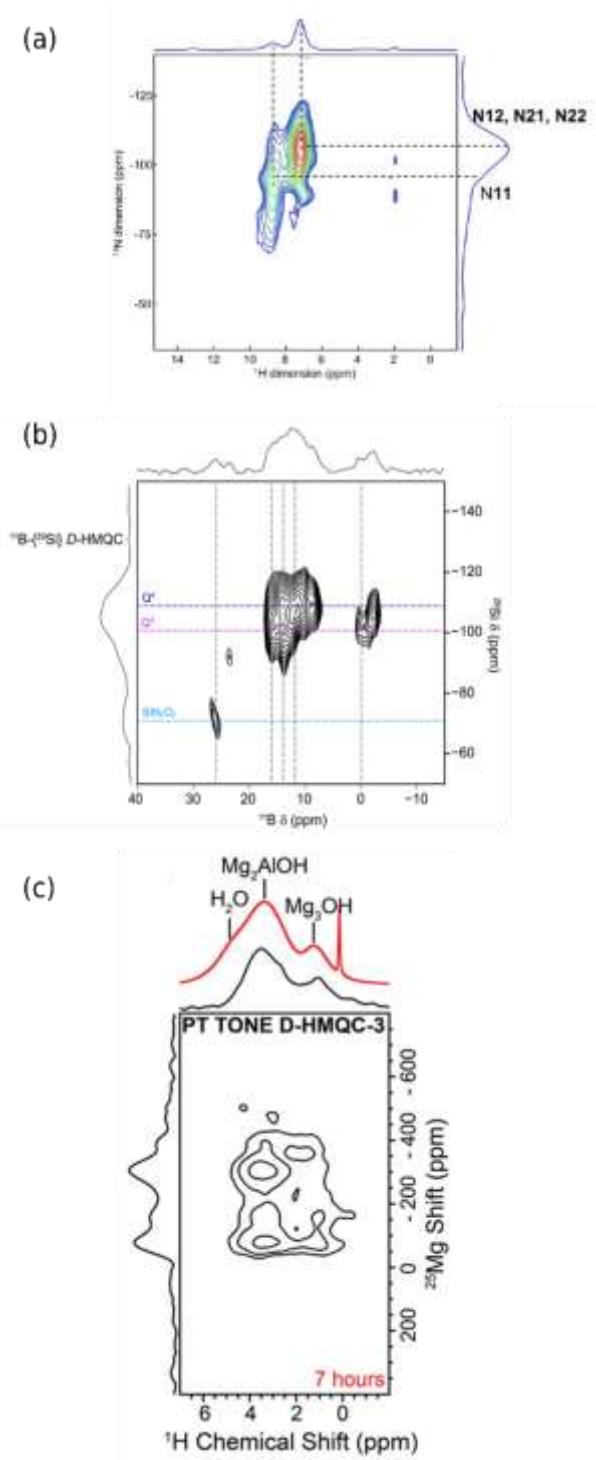

Figure 25. (a) 2D $^1H\{^{14}N\}$ *D*-HMQC-SR4_1^2 spectrum of layered aluminophosphate containing amine structure directing agents acquired at B_0 = 18.8 T with ν_R = 62.5 kHz. Figure adapted from ref. [272]. Copyright, 2013, American Chemical Society. (b) 2D $^{11}B\{^{29}Si\}$ *D*-HMQC-SFAM-1 spectrum of boron nitride supported on dendritic fibrous silica nanoparticles acquired at B_0 = 18.8

T with ν_R = 14.286 kHz. Figure adapted from ref. [285]. Copyright, 2020, American Chemical Society. (c) 2D ^{1}H{^{25}Mg} TONE *D*-HMQC-SR4_1^2 spectrum of Mg-Al double layered hydroxides acquired at B_0 = 9.4 T with ν_R = 60 kHz. Figure adapted from ref. [225]. Copyright, 2020, Royal Society of Chemistry.

When the spy isotope is subject to large homonuclear dipolar interactions, like ^{1}H, a recoupling reintroducing the $|m|$ = 2 space component of the heteronuclear dipolar interaction, such as SR4_1^2, must be employed since they eliminate the contribution of homonuclear dipolar interactions to the first-order average Hamiltonian [220,280]. Furthermore, the resolution along the ^{1}H dimension of proton-detected *D*-HMQC experiment can be improved by applying homonuclear decoupling schemes on ^{1}H channel during t_1 period [281]. The *D*-HMQC sequence allows the indirect detection of half-integer quadrupolar nuclei via protons, which can enhance the sensitivity, notably at high MAS frequencies, $\nu_R \geq 40$ kHz [239]. Nevertheless, this experiment exhibits t_1-noise, as already mentioned in section 3.2.1. When the indirectly detected isotope is a half-integer quadrupolar nucleus, TONE *D*-HMQC sequence, shown in Figure 20b, can be employed by applying CT-selective 180° pulses during the defocusing and refocusing delays [225]. This technique has been used for indirect detection via protons of ^{27}Al and ^{25}Mg quadrupolar nuclei (see Figure 25c). For I = 3/2, an alternative consists in the use of T-HMQC scheme, which has been recently applied for the indirect detection via protons of ^{35}Cl 1Q, 2Q and 3Q coherences [229,286]. Nevertheless, to the best of your knowledge, it has not yet been employed for inorganic or hybrid materials.

Table 6. List of the pairs of spin-1/2 and half-integer quadrupolar isotopes, for which their signals have been correlated using *D*-HMQC sequence in inorganic or hybrid materials.

S	*I*	Sequence	Sample	Ref.
^{1}H	^{14}N	*D*-HMQC- SR4_1^2	layered aluminophosphate	272
^{1}H	^{23}Na	*D*-HMQC- SR4_1^2	NaH_2PO_4	281
^{1}H	^{25}Mg	TONE *D*-HMQC	layered double hydroxide	225
^{1}H	^{27}Al	*D*-HMQC-R^3	crystalline aluminophosphate $AlPO_4$-14	237
		TONE *D*-HMQC	layered double hydroxide	225
^{1}H	^{43}Ca	*D*-HMQC-R^3	hydroxyapatite	287
^{1}H	^{71}Ga	*D*-HMQC- SR4_1^2	gallium complex	239
^{11}B	^{1}H	*D*-HMQC- SR4_1^2	B_2O_3/BN supported on silica	285
^{11}B	^{29}Si	*D*-HMQC- SR4_1^2	borosilicate glass	46
^{11}B	^{31}P	*D*-HMQC-SFAM-1	borophosphate glass	236
^{11}B	^{207}Pb	*D*-HMQC- R2_1^{-1}(tt)	crystalline lead borate	284
^{13}C	^{7}Li	*D*-HMQC-SFAM-1	alkylaluminium	174
^{13}C	^{27}Al	*D*-HMQC-SFAM-1	alkylaluminium	174
^{17}O	^{1}H	*D*-HMQC- SR4_1^2	silica-supported catalysts	288
^{17}O	^{29}Si	*D*-HMQC- SR4_1^2	zeolites	289
^{23}Na	^{29}Si	*D*-HMQC- SR4_1^2	crystalline sodium phosphate	290
^{23}Na	^{31}P	*D*-HMQC-R^3	crystalline aluminophosphate	237
^{29}Si	^{17}O	DNP+ *D*-HMQC- SR4_1^2	silica and silica alumina	291
^{27}Al	^{1}H	*D*-HMQC- SR4_1^2	γ-alumina	292
^{27}Al	^{13}C	*D*-HMQC-SFAM-1	alkylaluminium	174
^{27}Al	^{29}Si	*D*-HMQC- SR4_1^2	montmorillonite clay	293
^{27}Al	^{31}P	*D*-HMQC-SFAM-1	aluminophosphate glass	237
^{51}V	^{31}P	*D*-HMQC-SFAM-1	vanadophosphate glass	236
^{71}Ga	^{31}P	*D*-HMQC-R^3	gallium-doped calcium phosphate ceramics	294

3.2.2.2 *With high-resolution*

As for through-bond HETCOR experiments, high-resolution version of through-space HETCOR sequence between spin-1/2 and half-integer quadrupolar isotopes have been developed. These high-resolution spectra have been first acquired using sequences deriving from 3Q-*J*-RINEPT scheme, in which the *J*-RINEPT block is substituted by CPMAS [20,295], *D*-RINEPT [238] or PRESTO [296] transfer. As explained above, the *D*-RINEPT and PRESTO transfer are more robust than CPMAS. Furthermore, the sensitivity of these experiments is enhanced using soft pulse added mixing (SPAM), which increases the efficiency of the reconversion of 3Q coherences into 1Q ones of the quadrupolar isotope [187,296]. The sensitivity of these high-resolution HETCOR experiments can be further improved by a factor of 2 at least by substituting the 3QMAS block by a satellite transition MAS (STMAS) scheme, which correlates the satellite transition and the CT to remove the second-order quadrupolar broadening [297,298]. Nevertheless, this STMAS version requires the adjustment of the magic angle with an accuracy of 0.001° and a very stable MAS frequency. Therefore, its implementation is usually more difficult than that of 3QMAS version. These sequences have been employed to correlate the high-resolution spectra of half-integer quadrupolar nuclei, such as ^{23}Na and ^{27}Al, with the spectra of spin-1/2 isotopes, such as ^{1}H and ^{31}P (see Figure 26). Note also that in the case of spin I = 3/2, STMAS technique can also be combined with *D*-HMQC scheme [299].

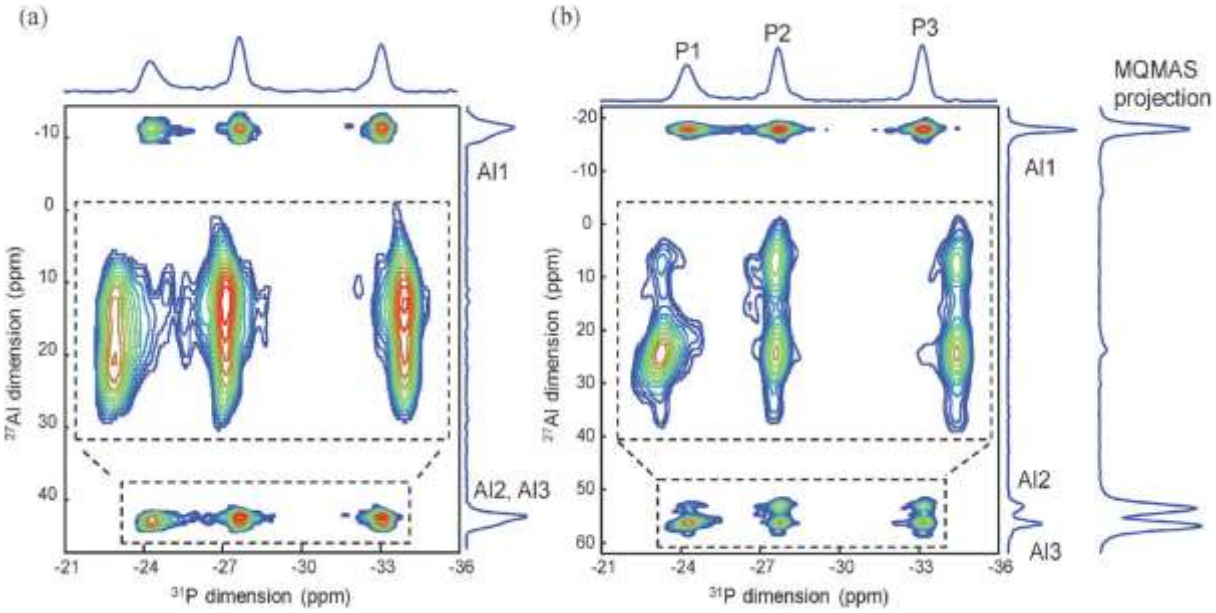

Figure 26. Comparison of 2D ^{31}P{^{27}Al} (a) *D*-RINEPT and (b) 3Q-*D*-RINEPT spectra of layered aluminophosphate acquired at B_0 = 18.8 T with ν_R = 22.222 kHz. Figure reprinted from ref. [238]. Copyright, 2012, Royal Society of Chemistry.

3.2.3 Between two half-integer quadrupolar isotopes

Proximities between distinct half-integer quadrupolar isotopes, such as ^{11}B and ^{27}Al, have been probed using CP-HETCOR using either continuous wave (CW) irradiation [18,300] or train of rotor-synchronized pulses [301]. However, the spin-lock and the CPMAS transfer lack robustness in the case of quadrupolar nuclei. This issue has been circumvented by the use of *D*-HMQC and *D*-RINEPT sequences [302,303]. For these sequences, the highest robustness has been achieved using synchronous phase inversion R^3 (SPI-R^3) scheme, which corresponds to the $C2_2^1$ symmetry [302]. Furthermore, we have shown that this recoupling scheme must be applied to the dephaser isotope with magnetization parallel to B_0 field to minimize the losses during the transfer [303].

4. Applications

In this section, we review how correlation experiments have been employed for the characterization of different classes of materials: microporous materials, heterogeneous catalysts, minerals, biomaterials and glasses.

4.1 *Microporous materials*

Correlation experiments have provided unique insights into the structure of microporous materials (with pore diameters < 2 nm), including crystalline aluminophosphates (AlPOs), zeolites and MOFs.

4.1.1 AlPOs

Microporous crystalline aluminophosphates have been used for various applications, such as adsorption, gas separation and catalysis. These aluminophosphate materials are built from alternating aluminium polyhedra and phosphorus tetrahedra connected through bridging oxygen atoms. They are usually synthesized using a quaternary amine as structure-directing agents. The charge of these cations is balanced by F^- and HO^- anions coordinated to the Al atoms. Water can also be present in the pores for as-prepared or rehydrated AlPOs. In addition, it is possible to substitute the P atoms by Si ones and the Al atoms by di- or tri-valent metal atoms, including Mg or Zn. Solid-state NMR complements diffraction studies for the characterization of AlPOs and provides unique information on the defects, such as substitution, the interaction between AlPO framework and the host molecules as well as the motions of guest within the pores. Several reviews about solid-state NMR of crystalline AlPOs have been published [52,304–306]. As AlPOs contains several NMR active isotopes, such as ^{31}P, ^{27}Al, ^{1}H, ^{19}F, ^{14}N, and ^{17}O, 2D homo- and hetero-nuclear correlation experiments have been extensively employed to assign their NMR spectra and to probe their medium-range (0.3-1 nm) structure.

Through-space homonuclear 2Q-1Q experiments using POST-C7 and BaBa recoupling have been employed to probe ^{31}P-^{31}P [209,307–309] and ^{1}H-^{1}H [308] proximities, respectively, in AlPOs, whereas similar experiment using $\mathrm{BR}2_2^1$ recoupling have been used to observe proximities between ^{27}Al nuclei [149,151,152].

The connectivities between Al and P sites in AlPOs have been probed using $^{27}Al\{^{31}P\}$ *J*-HMQC experiment [160] but also $^{31}P\{^{27}Al\}$ 3Q-*J*-RINEPT variant featuring high-resolution along the ^{27}Al dimension [310–312]. Furthermore, $^{27}Al\{^{19}F\}$ *J*-HMQC experiment has been employed to investigate the F^-/HO^- distribution in fluorinated AlPOs (see Figure 14) [128].

Similarly proximities between Al and P sites have been observed using $^{31}P\{^{27}Al\}$ CP-HETCOR experiment [308], its variant with 3Q filter to suppress the second-order quadrupolar broadening of the ^{27}Al NMR spectra [187,307,313,314] and more recently the 3Q-*D*-RINEPT version [238,272,309,315]. The location of F^- anions in fluorinated aluminophosphates has been investigated using 2D $^{31}P\{^{19}F\}$ and $^{27}Al\{^{19}F\}$ CP-HETCOR spectra (see Figure 27) [308,309]. Proximities between protons and half-integer quadrupolar isotopes, such as ^{23}Na and ^{27}Al, in AlPOs have also been probed using high-resolution ST-CP-HETCOR experiments [297].

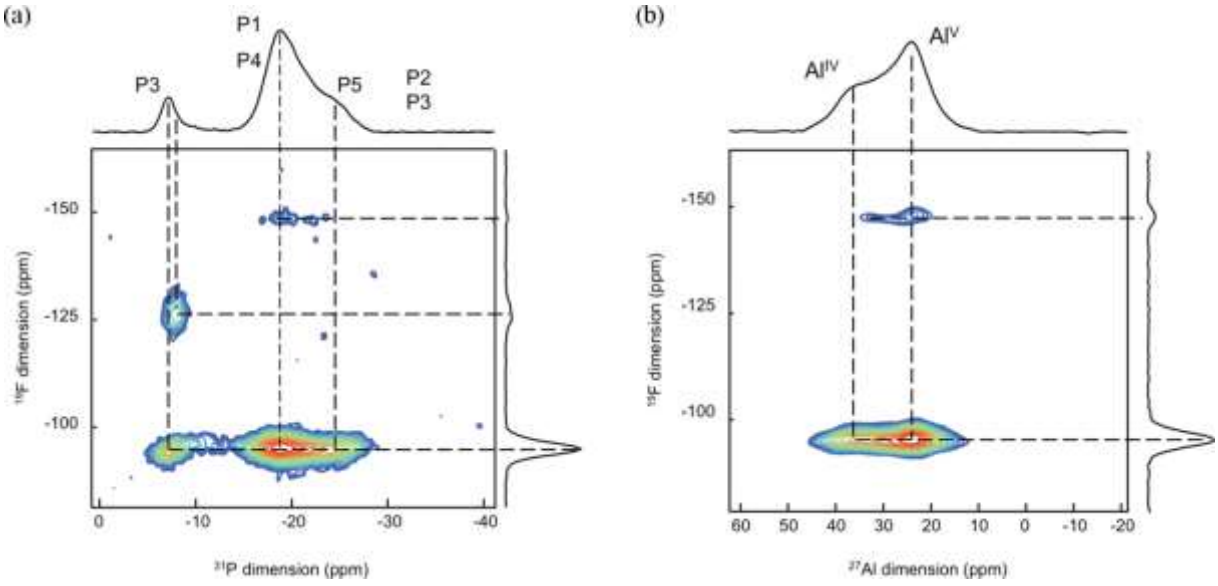

Figure 27. 2D (a) ^{31}P{^{19}F} and (b) ^{27}Al{^{19}F} CP-HETCOR spectra of fluorinated aluminophosphate DNL-1 at acquired at B_0 = 11.7 T with ν_R = 28 kHz. Figure reprinted from ref. [308]. Copyright, 2011, American Chemical Society.

4.1.2 Zeolites

Aluminosilicate zeolites are microporous materials made of a 3D network of corner-sharing SiO_4 and AlO_4 tetrahedra. Furthermore, metals, such as Sn, Mo, Zn or Ga, can be introduced in the zeolites. They are widely employed for various applications, such as catalysis, ion exchange and separations. They contain several NMR active isotopes, such as ^{27}Al, ^{29}Si, ^{17}O, ^{1}H and ^{23}Na and hence, solid-state NMR provides detailed information on the structure of the framework and notably the presence of defects, the extra-framework species, the host-guest interactions and the catalytic reactions within the zeolite pores [57–59,304,305]. In particular, homo- and hetero-nuclear correlation NMR experiments are essential tools for the characterization of these materials.

The Si−O−Si connectivities can be identified by 2D ^{29}Si INADEQUATE experiments [69,79,82,88,316,317]. Owing to the low natural abundance of ^{29}Si isotope (4.7%), the sensitivity of these experiments has been enhanced using ^{29}Si isotopic enrichment [79,88,317] or DNP (see Figure 4) [82]. The observation of proximities between ^{29}Si nuclei using ^{29}Si 2Q-1Q through-space homonuclear correlation also provides useful information on the structure of the zeolite framework [107,112,318]. Proton 2Q-1Q through-space homonuclear correlations have been employed to probe the proximities between Lewis and Brønsted acid sites [319,320] and more recently the location of $SiO^{-}\cdots HOSi$ defects in zeolites and their interaction with structure-directing agent [321,322], whereas the presence of clusters of three silanol groups was demonstrated using the 3Q-1Q counterpart [121,323]. The ^{13}C PDSD experiment has been employed to observe adsorbed species and probe intermolecular interactions between cyclopentenyl cation intermediates and hydrocarbons during methane to olefins reaction over zeolite [324–328]. The incorporation of Al atoms in the zeolite frameworks results in the formation of Brønsted acid sites made of bridging silanol SiOHAl. The dealumination converts some of these Brønsted acid sites into extra-framework Al sites, which act as Lewis acid sites, and hence, enhances the catalytic activity and the selectivity of zeolites. This process has been investigated by probing proximities between Al atoms using ^{27}Al 2Q-1Q through-space homonuclear correlation, which show the proximity between Lewis and Brønsted acid sites (see Figure 8) [157].

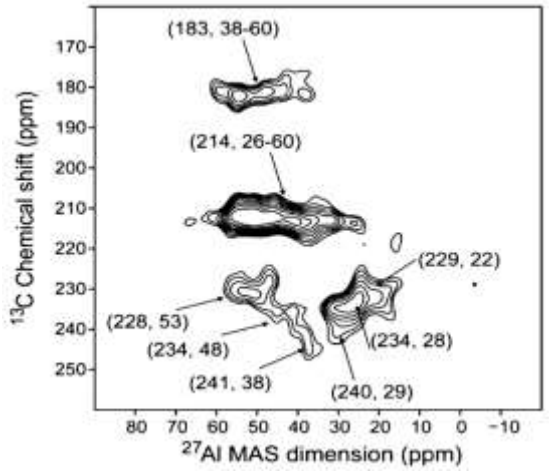

Figure 28. 2D ^{27}Al{^{13}C} D-HMQC spectrum of 2-^{13}C-acetone loaded on dealuminated HY zeolite acquired B_0 = 18.8 T with ν_R = 20 kHz. Figure adapted from ref. [329]. Copyright, 2014, American Chemical Society.

Furthermore, the position of Al atoms within the framework strongly influences the Brønsted acidity of zeolites. It has been investigated using ^{27}Al{^{29}Si} *J*- and *D*-HMQC experiments [330–335]. Brønsted acid sites have also been observed using ^{27}Al{^{1}H} CP-HETCOR [331] and *D*-HMQC experiments [332,334,336,337]. In particular, the acquisition of 2D ^{27}Al{^{1}H} *D*-HMQC spectrum at 35.2 T revealed the presence of partially hydrolyzed Brønsted acid sites and provided unprecedented information on the distribution of Al atoms in the zeolites [334,337]. Tri-coordinated framework Al atoms (Al(OSi)$_3$) acting as Lewis acid sites have also been revealed using trimethylphosphine oxide (TMPO) as a base probe molecules and ^{31}P{^{1}H} CP-HETCOR as well as ^{31}P{^{27}Al} PT-*D*-HMQC experiments [338]. The ^{17}O{^{29}Si} *D*-HMQC experiment on doubly ^{17}O- and ^{29}Si-enriched zeolites has demonstrated the hydrolytic rearrangements occurring during the preparation of these zeolites [289]. The acid sites created by the incorporation of Sn atoms into zeolite framework have also been observed using ^{1}H{^{119}Sn} *D*-HMQC experiments [230]. Similarly ^{11}B{^{1}H} CP-HETCOR [251], ^{1}H{^{11}B} *D*-RINEPT [339] and ^{11}B{^{29}Si} *J*-HMQC [178] experiments have been used to probe the location of B atoms in zeolite substituted with boron. The ^{27}Al{^{13}C} *D*-HMQC experiment was also applied to probe the interactions between adsorbed ^{13}C-enriched acetone molecules and the Lewis and Brønsted acid sites of dealuminated HY zeolite (see Figure 28) [329]. This double-resonance ^{13}C-^{27}Al NMR experiment requires a frequency splitter owing to the close Larmor frequencies of these isotopes.

4.1.3 MOFs

Metal-organic frameworks are crystallized hybrids materials with promising applications in the field of gas storage, chemical separation, catalysis, depollution, sensing and drug delivery. They are built from an inorganic cluster and an organic ligand yielding to a porous framework. They contain a wide range of NMR-active isotopes, such as ^{1}H, ^{13}C, ^{27}Al or ^{45}Sc.

Correlation NMR experiments are essential techniques to probe the structure of MOFs, and notably the location of defects, as well as the host-guest interactions in these materials. For instance, 2D ^{1}H 2Q-1Q homonuclear correlation at high MAS frequency has been used to assign the ^{1}H signals of MOFs (see Figure 6) and probe the interactions of caffeine with UiO-66(Zr) MOFs [111,340,341], whereas 2D ^{1}H spin diffusion measurements have been employed to probe the spatial arrangement of linkers in MOFs made of different linkers [342,343] as well as the host-guest interactions and ethane/ethylene separation mechanism on zeolitic imidazolate frameworks [344,345].

The $^{13}C\{^{1}H\}$ CP-HETCOR, $^{1}H\{^{13}C\}$ *J*-HMQC experiments and their combination with ^{1}H spin diffusion experiments have been applied to probe the host-guest interactions in MOFs [345–349], and notably the adsorption of CO_2 in MOFs functionalized with diamine or alcohol amine [349,350]. The proximities between ^{13}C and ^{27}Al nuclei in MIL-100(Al) MOF have also been probed using DNP-enhanced $^{13}C\{^{27}Al\}$ and $^{27}Al\{^{13}C\}$ *D*-HMQC experiments [351]. Similarly, $^{45}Sc\{^{1}H\}$ *D*-HMQC experiments were carried out to monitor the structural modification of the MIL-100(Sc) during thermal treatment (see Figure 29) [352].

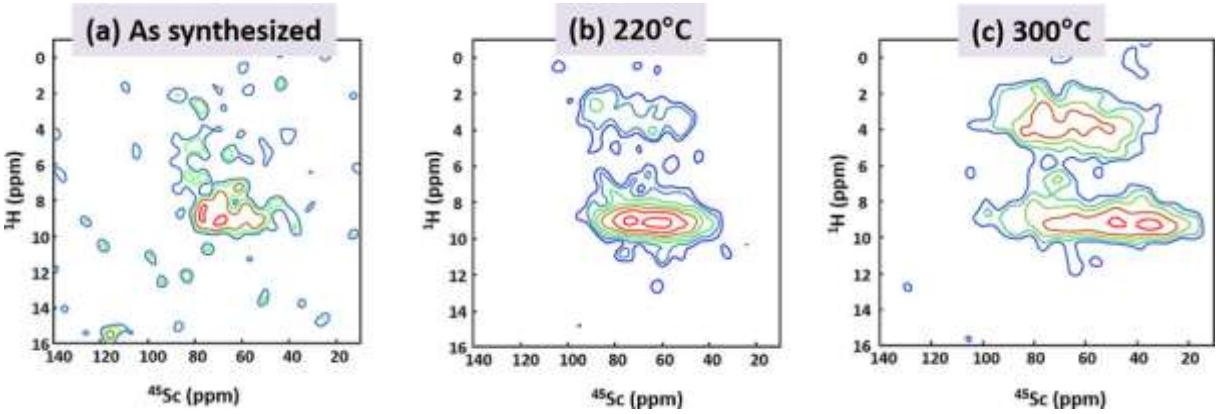

Figure 29. $^{45}Sc\{^{1}H\}$ *D*-HMQC 2D spectra of (a) as-synthesized MIL-100(Sc), and after thermal treatment at (b) 220, and (c) 300 °C. The 2D spectra were recorded at B_0 = 18.8 T with ν_R = 20 kHz. Figure reprinted from ref. [352]. Copyright, 2017, Wiley.

4.2 *Metal oxide catalysts*

Beside microporous materials, solid-state NMR can provide precious insights into the atomic-level structure and dynamics of other heterogeneous catalysts, including notably metal oxides and supported single-site catalysts [53–56,353–355]. These materials contain several NMR-active isotopes, such as ^{1}H, ^{13}C, ^{17}O, ^{19}F, ^{29}Si and ^{27}Al. Through-bond and through-space correlation NMR experiments provide detailed information about the arrangement of atoms near the surface of the catalysts. Nevertheless, a difficulty is that the nuclei of the surface represent only a small fraction of the total amount of nuclei in the case of nanoparticles and mesoporous materials with surface area ranging from 10 to 100 $m^2.g^{-1}$ [356]. Furthermore, several of the NMR active isotopes, such as ^{13}C, ^{17}O and ^{29}Si, in these materials exhibit low natural abundance.

Therefore, 2D correlation on metal oxide catalysts were first demonstrated for sensitive spins, such as ^{1}H, ^{19}F or ^{27}Al, or using isotope enrichment for isotopes, such as ^{13}C and ^{17}O. In particular, ^{1}H 1Q-1Q, 2Q-1Q and 3Q-1Q through-space correlation experiments have been applied to probe the spatial distribution of organic functional groups as well as hydroxyl groups on surfaces as well as the ordering of mixed surfactants in mesoporous silica [55,195,292,357–359]. The 3Q-1Q variant has the advantage to allow the unambiguous observation of proximities between CH_2 groups provided their ^{1}H resonances are resolved. Similarly, ^{19}F 1Q-1Q and 2Q-1Q through-space correlation spectra have been used to assign the signals of BF_4^- and free F^- anions for BF_4^- salt of Pd(II) complex immobilized on silica [116]. Furthermore, 2Q-1Q through-space correlation techniques have been applied to probe proximities between ^{27}Al nuclei in amorphous silica alumina[360] and more recently between ^{17}O sites in ^{17}O-labeled γ-alumina (see Figure 30)[361].

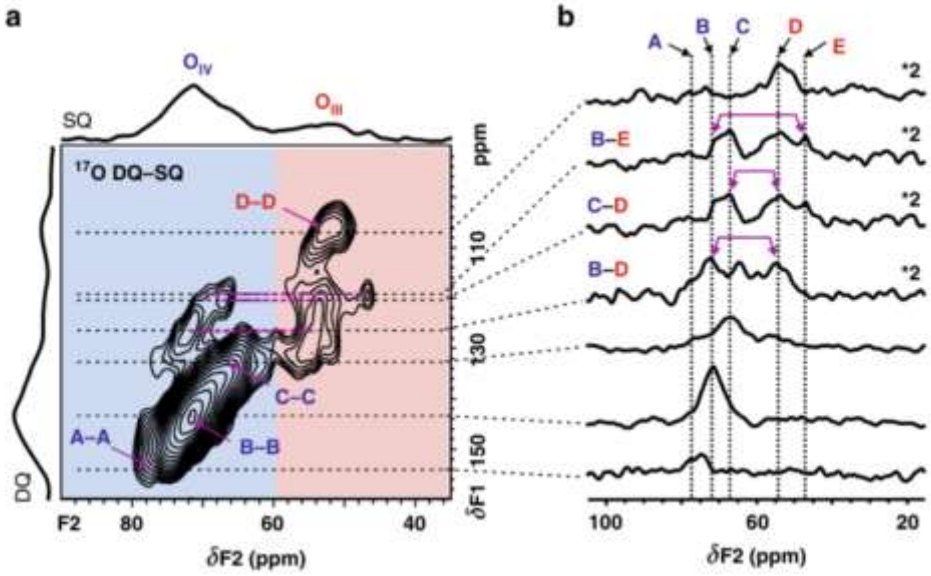

Figure 30. (a) ^{17}O 2Q-1Q homonuclear correlation NMR spectrum of γ-Al_2O_3 recorded at B_0 = 35.2 T with ν_R = 16 kHz and (b) extracted slices along F_2 dimension. This spectrum allows resolving five oxygens sites (3 OAl_4 also denoted O_{IV} and 2 OAl_3, denoted O_{III}). The sites A, C and D were assigned to surface sites with proximity to surface hydroxyl groups or water molecules, whereas sites B and E are identified as bulk oxygen sites. Figure adapted from ref. [361]. Copyright, 2020, Nature Portfolio.

Moreover, metal oxide catalysts have also been characterized using conventional 2D heteronuclear correlation experiments. For instance, *J*-HMQC sequence has allowed the selective of observation AlH species on the surface of γ-alumina[175] and OH groups on ^{17}O-labeled silica and alumina[288,361]. Through-bond and through-space heteronuclear correlation experiments have also been employed to probe ^{1}H-^{13}C connectivities and proximities in supported metal complexes and organic functional groups as well as surfactants (see Figure 10)[164,215,362–364]. These experiments were initially recorded for ^{13}C-labeled samples[362,363]. Nevertheless, it was later demonstrated that the sensitivity gain provided by indirect detection via protons allows their acquisition in natural abundance using conventional NMR [215,364]. Similar approaches have been used to probe proximities between protons and other spin-1/2 isotopes, such as ^{15}N[195,216], ^{19}F[365], ^{29}Si[90] and ^{195}Pt[227], near surfaces (see Figure 18). Furthermore, through-space heteronuclear correlation experiments have also been applied to probe proximities between protons and half-integer quadrupolar nuclei, such as ^{11}B[116,366], ^{17}O[288,367] and ^{27}Al[292,368–373]. These experiments allow notably the selective observation of ^{11}B, ^{17}O and ^{27}Al nuclei located near the surface of oxide or nitride phases since their bulk region does not contain protons. In particular, 2D ^{27}Al{^{1}H} *D*-HMQC experiment has been employed to identify the hydroxyl groups at the surface of γ-alumina[292] and the preferential grafting sites of metal complexes on these surfaces (see Figure 31)[369] as well as the nature of Brønsted acid sites near the surface of amorphous silica alumina[368,373]. Furthermore, 2D ^{11}B{^{29}Si} and ^{27}Al{^{29}Si} *D*-HMQC experiments have been used to probe the anchoring of BN/B_2O_3 and Al_2O_3 phases on silica nanoparticles (see Figure 25b)[285,372].

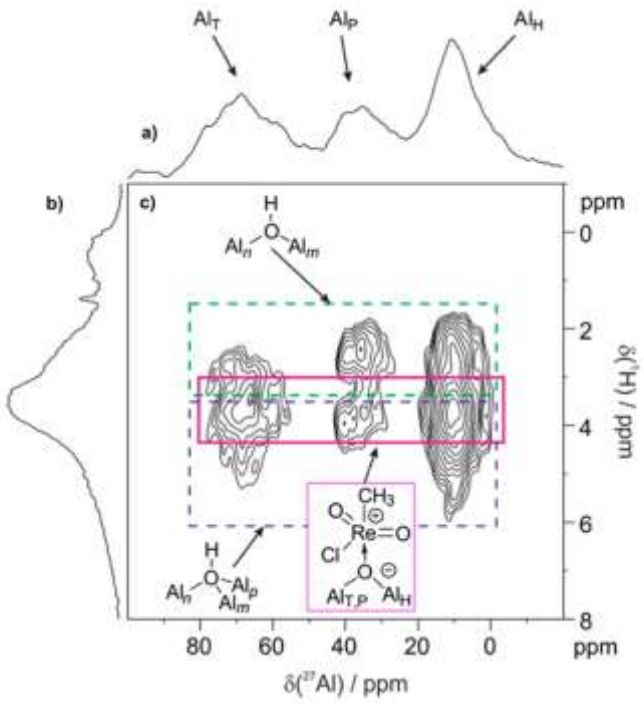

Figure 31. (a-c) 2D ^{27}Al{^{1}H} *D*-HMQC spectrum of methyltrioxorhenium MTO supported on chlorinated alumina together with (a) ^{27}Al projection and (b) 1D ^{1}H MAS spectrum acquired at B_0 = 18.8 T with ν_R = 20 kHz. Figure reprinted from ref. [369]. Copyright, 2016, American Chemical Society.

In addition, the sensitivity enhancement offered by DNP, which can exceed two orders of magnitude[83], has been leveraged to acquire 2D correlation spectra involving surface nuclei of low natural abundance, such as ^{13}C, ^{29}Si and ^{17}O. For instance, DNP-enhanced homonuclear correlation experiments have allowed the observation of ^{13}C-^{13}C and ^{29}Si-^{29}Si connectivities and proximities near surface, providing new insights into the structure of catalytic intermediates and products (see Figure 7f)[131,374] as well as the spatial distribution of silica-bound organic functional groups (see Figure 7d)[113,130]. Thanks to the sensitivity enhancement provided by DNP, some of these experiments were acquired in natural abundance, even if the probability of ^{13}C-^{13}C and ^{29}Si-^{29}Si pairs in that case is as low as 0.01 and 0.2%, respectively. The sensitivity enhancement offered by DNP has also permitted the observation of ^{1}H-^{17}O[248,375] and ^{17}O-^{29}Si[291] pairs with probability of 0.038 and 0.0017% in natural abundance, thus allowing the detection of silanol and siloxane groups at the surface of silica and amorphous silica alumina.

4.3 *Minerals and biomaterials*

Minerals make up both the surface and inner layers of the Earth's geological structure, and are also used in industry as, for example, cements, ceramics, glasses, fertilisers and heterogeneous catalysts [376–379]. Biomaterials are those materials interacting with biological systems. Modern applications of biomaterials include joint replacements, dental implants, tissue engineering (including bone repair) and the emerging field of "smart" biomaterials, that are capable of modifying their physicochemical and mechanical properties in response to external stimuli [380,381]. Inorganic biomaterials notably include calcium phosphates, such as hydroxyapatite ($Ca_{10}(PO_4)_6(OH)_2$) and tricalcium phosphate ($Ca_3(PO_4)_2$), which are present in natural bones but are also used in the fabrication of components for the repair and reconstruction of damaged parts of the musculoskeletal system, but also due to their presence in [382,383]. Minerals and inorganic biomaterials contain several NMR-active isotopes, such as ^{1}H, ^{17}O, ^{19}F, ^{29}Si, ^{31}P, ^{27}Al and ^{43}Ca. Hence, solid-state NMR spectroscopy, including 2D correlation experiments, is

largely employed to characterize atomic-level structures, and notably defects lacking long-range positional order, in minerals and biomaterials [376–379,384].

The proximities between hydrogen sites have notably been probed using 2D ^{1}H homonuclear correlation experiments [385–390]. These 2D spectra provided information about the location of hydrogen in hydrous wadsleyite (β-$(Mg,Fe)_2SiO_4$)[388], which has received interest as a potential reservoir for hydroxyls (water) in Earth's mantle (see Figure 32a), as well as the cation clustering in Mg/Al layered double hydroxides (LDH)[386,387]. Homonuclear correlation experiments have also been applied to probe ^{31}P-O-^{31}P connectivities in calcium phosphate phases[391,392] and ^{29}Si-^{29}Si proximities in a feldspar mineral [393]. Furthermore, the sensitivity gain offered by DNP allowed to record 2D ^{13}C 2Q-1Q homonuclear correlation of isotopically unmodified carbonated hydroxyapatite nanoparticles[394]. This spectrum demonstrated the clustering of carbonate anions. Proximities between Al sites in minerals were also probed by 2D ^{27}Al 2Q-1Q homonuclear correlation [151,393,395].

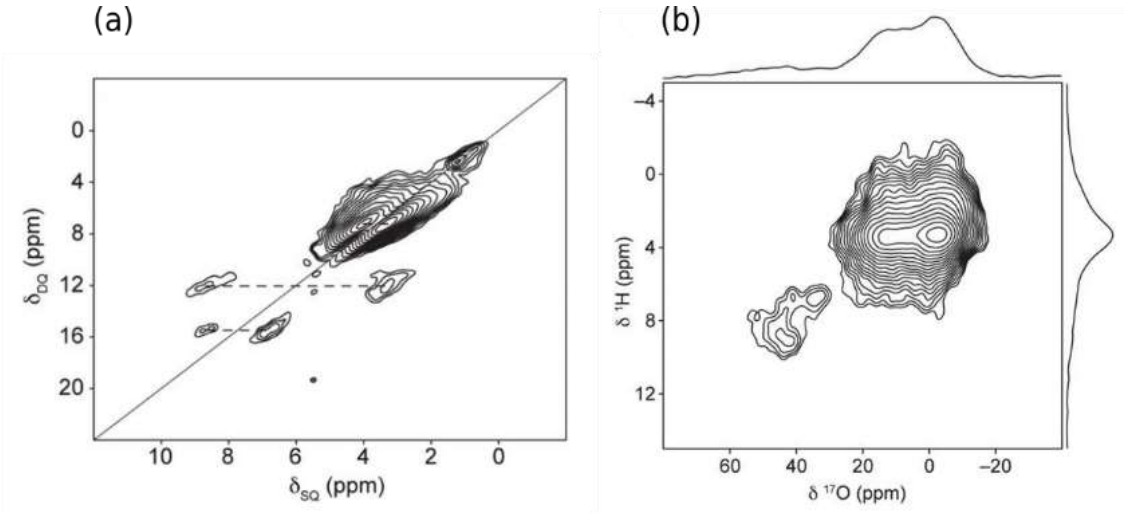

Figure 32. (a) 2D ^{1}H 2Q-1Q homonuclear correlation spectrum of hydrous wadsleyite recorded using the BABA recoupling sequence. 2Q correlations are indicated by dashed lines and the solid line denotes the autocorrelation diagonal. The spectrum was acquired at B_0 = 14.1 T with ν_R = 30 kHz. (b)) 2D ^{17}O{^{1}H} CP-HETCOR spectrum of ^{17}O-enriched hydrous wadsleyite recorded at B_0 = 20 T with ν_R = 30 kHz. Figure adapted from ref. [388]. Copyright, 2013, Royal Society of Chemistry.

Regarding heteronuclear correlation, 2D ^{31}P{^{1}H} CP-HETCOR experiment has widely used to investigate the nature of calcium phosphate phases in bones [197,396–399] as well as the interaction of calcium phosphate surfaces with other compounds [400–402]. This experiment as well as 2D ^{13}C{^{1}H} CP-HETCOR and more recently, DNP-enhanced ^{13}C{^{31}P} CP-HETCOR experiments have provided information about the location of anionic substituents in calcium phosphate phases [394,403,404]. Heteronuclear correlation between protons and ^{43}Ca isotope, which is low-γ quadrupolar nucleus (I = 7/2 and $|\gamma(^{43}Ca)/\gamma(^{1}H)|$ = 6.7%), has also been reported, first for ^{43}Ca-enriched hydroxyapatite and oxy-hydroxyapatite [287] and more recently, in natural abundance (0.14%) using DNP for carbonated hydroxyapatite (see Figure 33b). S{^{1}H} CP-HETCOR experiments with S = ^{13}C[196,405,406], ^{19}F[196] and ^{29}Si[405,407,406,408,409] have also been applied to study clay minerals and notably their interactions with organic cations and molecules. Correlation between ^{1}H and ^{29}Si nuclei as well as ^{17}O{^{1}H} CP-HETCOR experiment has also provided information about the location of protons in magnesium silicate phases (see Figure 32b) [385,388,410]. In addition, correlation experiments between ^{27}Al isotope and spin-1/2 nuclei, such as ^{1}H[411,412], ^{19}F[412] and ^{29}Si[187,293,393], have been employed to gain insight into the location of cations, anions and vacancies in minerals and to identify impurities (see Figure 16).

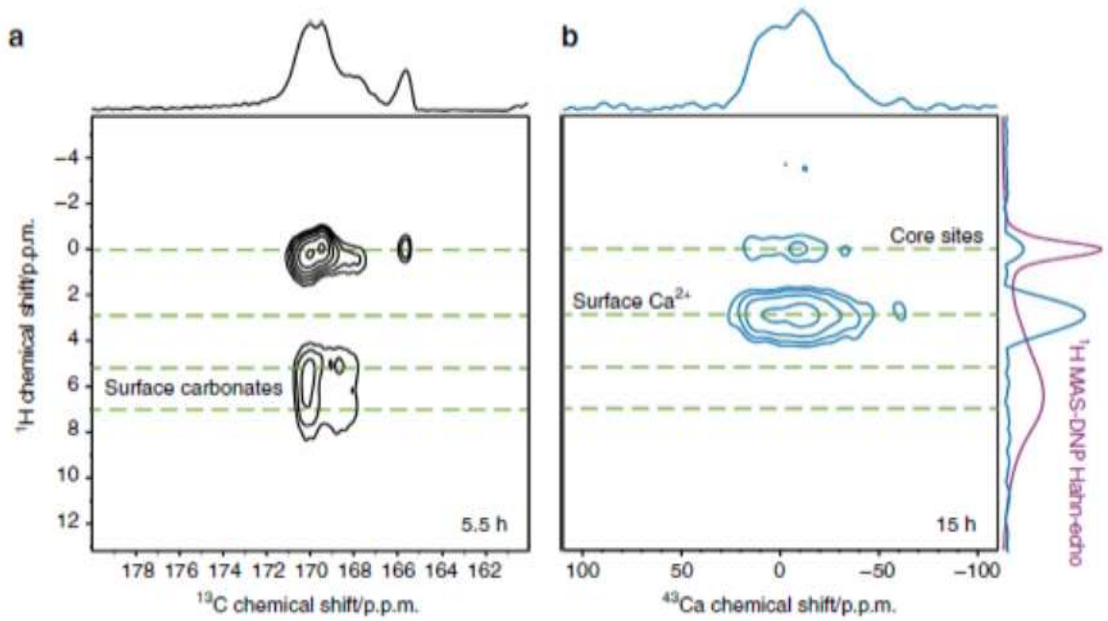

Figure 33. DNP-enhanced solid state NMR spectra of carbonated hydroxyapatite nanoparticles recorded at B_0 = 9.4 T and ~100 K with ν_R = 8.5 kHz. (a) 2D $^{13}C\{^1H\}$ CP HETCOR spectrum with associated ^{13}C skyline projection (top). (b) 2D $^{43}Ca\{^1H\}$ CP-HETCOR spectrum with associated ^{43}Ca (top) and ^1H (right) skyline projections. Both 2D spectra were recorded using ^1H FSLG homonuclear and SPINAL-64 heteronuclear decoupling. Also shown for comparison is the DNP-enhanced ^1H Hahn-echo MAS NMR spectrum (far right, purple). Figure adapted from ref. [250]. Copyright, 2017, American Chemical Society.

4.4 *Glasses*

Glasses are amorphous solids produced by the disequilibrium cooling of a liquid. These materials have a wide range of applications, including windows, containers, optical devices, nuclear waste storage and protective coatings. The characterization of atomic-level structures of glasses is challenging owing to their lack of long-range positional order. As a local characterization technique, solid-state NMR is particularly useful for investigating the structure glasses [49–52]. Glasses contains several NMR active nuclei, such as ^{11}B, ^{29}Si, ^{27}Al, ^{31}P, ^{71}Ga and ^{77}Se. Correlation NMR experiments provide unique insight into the medium-range structure of glasses, i.e. the linkage between structural units, such as SiO_4, BO_4, BO_3, AlO_4 and PO_4 groups.

The P−O−P and Si−O−Si connectivities have been probed using 2D ^{31}P[61,74,76] and ^{29}Si[87,413] through-bond homonuclear correlation experiments, and notably the refocused INADEQUATE sequence[74,76,87]. The ^{31}P 3Q-1Q variant has been employed to observe trimers of phosphate units in lead phosphate glasses [61]. Furthermore, through-space ^{31}P[99,414–417] and ^{29}Si[418] homonuclear correlation experiments have provide information on the proximities between these units. The homonuclear correlation experiments for ^{29}Si isotope have been recorded on ^{29}Si-enriched silicate glasses, given the low natural abundance of this isotope. Although 1Q-1Q homonuclear correlation spectra were recorded in the 1990s[99,413,414], their 2Q-1Q variants[415–418] are usually preferred since they allow to probe connectivities and proximities between nuclei with close resonance frequencies. The proximities between hydrogen sites in weathered surface of phosphate was investigated using ^1H 2Q-1Q homonuclear correlation and 1Q-1Q spin diffusion experiments [419]. The 2Q-1Q homonuclear correlation experiments have also been employed to probe ^{11}B-^{11}B[151] and ^{27}Al-^{27}Al[420,421] proximities in glasses.

J-HMQC experiments have been applied to study connectivities between spin-1/2 and quadrupolar isotopes (^{19}F–^{11}B[176], ^{29}Si–O–^{27}Al[179], ^{31}P–O–^{11}B[180], ^{31}P–O–^{27}Al[77]) as well as distinct half-integer quadrupolar isotopes ^{17}O-^{27}Al[19]. The Se-Ga bonds in gallium selenide glass have also been probed using *J*-HMQC and *J*-RINEPT experiments[170]. Furthermore, 2D through-space heteronuclear correlation

experiments have been used to reveal the proximities between ^{31}P nuclei and various spin-1/2 (^{1}H[198], ^{29}Si[422]) and half-integer quadrupolar (^{11}B[253,423], ^{27}Al[236,256], ^{51}V[424]) isotopes. Similar experiments have been applied to probe the proximities between ^{29}Si isotope and ^{11}B[46,252] and ^{17}O[254] quadrupolar nuclei. The 2D ^{29}Si{^{17}O} CP-HETCOR spectra were acquired on ^{17}O-enriched samples. The heteronuclear correlation between spin-1/2 and quadrupolar isotopes were initially acquired using CP-HETCOR sequence[252,253,256]. Nevertheless, as explained in section 3.2.2.1, the *D*-HMQC sequence for that purpose is currently preferred owing to its higher robustness (see Figure 34)[46,236]. Proximities between distinct half-integer quadrupolar nuclei, ^{11}B and ^{27}Al, have also been observed in glasses using CP-HETCOR experiments [18,301].

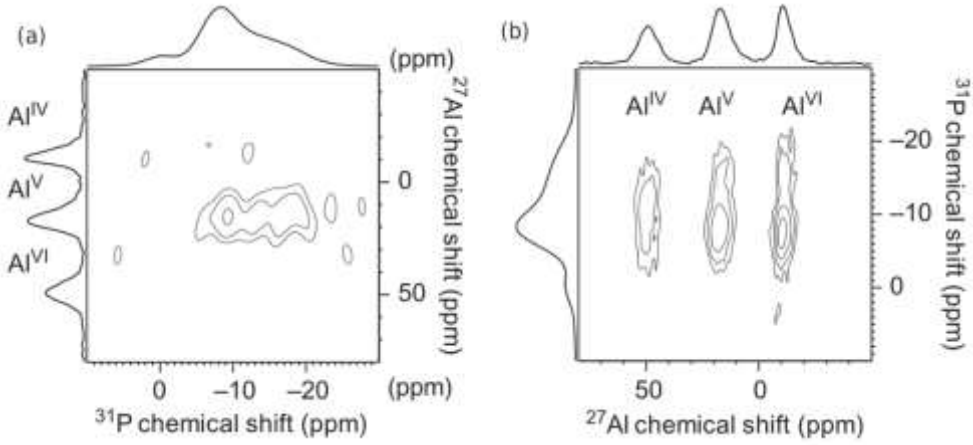

Figure 34 Comparison of (a) 2D ^{31}P{^{27}Al} CP-HETCOR and (b) 2D ^{27}Al{^{31}P} *D*-HMQC-SFAM-1 spectra of $50K_2O–10Al_2O_3–P_2O_5$ glass recorded at B_0 = 18.8 T with ν_R = 20 kHz. Figure adapted from ref. [52]. Copyright, 2018, Elsevier.

5. Conclusion

We have presented here the through-bond and through-space homo- and hetero-nuclear experiments, which have been developed and applied to probe connectivities and proximities in inorganic and hybrid solids. We have notably highlighted the state-of-the-art pulse sequences for each class of experiments. We also have shown how these correlation NMR experiments provide unique information on the atomic-level structure of a wide range of materials, including microporous materials, metal oxide catalysts, minerals, biomaterials and glasses. These experiments have also been employed for other types of materials, including cements[425–429], nanomaterials[80,91,167,201] and energy materials[129,430–436].

The recent advent of ultra-high field NMR magnet with B_0 = 28 T or even 35.2 T [437,438] improves the sensitivity and the resolution of solid-state NMR, notably for quadrupolar nuclei and hence, will expand the application range of correlation NMR experiments by allowing their use for insensitive isotopes (with low gyromagnetic ratio or low natural abundance) as well as for nuclei subject to large quadrupolar interaction. Further gains in sensitivity are expected from the development of cryogenic MAS probes [439] and MAS DNP [83,440], which will facilitate the acquisition of correlation experiments for isotopes of low receptivity but also for diluted species (surfaces, interfaces, defects) or limited-volume materials (thin-films or cultural heritage samples).

Furthermore, the increased availability of fast MAS probes reaching MAS frequencies of 150 kHz or above combined with high magnetic fields[441,442] is expected to promote the use of detection via protons in correlation experiments.

At the same time, correlation experiments at ultra-high fields are a challenge owing to increased electronic shielding as well as the need to develop performant double- and triple-resonance probes at such high fields. Therefore, further methodological and instrumental developments will be required to apply correlation experiments at ultra-high fields.

Acknowledgements

Chevreul Institute (FR 2638), Ministère de l'Enseignement Supérieur, de la Recherche et de l'Innovation, Hauts-de-France Region, and FEDER are acknowledged for supporting and funding partially this work. Financial support from the IR INFRANALYTICS FR2054 CNRS for conducting the research is gratefully acknowledged. This project has received funding from the European Union's Horizon 2020 research and innovation program under the Skłodowska-Curie agreement No. 847568. OL acknowledges financial support contract ANR-18-CE08-0015-01 (ThinGlass).

References

(1) Cavadini, S.; Lupulescu, A.; Antonijevic, S.; Bodenhausen, G. Nitrogen-14 NMR Spectroscopy Using Residual Dipolar Splittings in Solids. *J. Am. Chem. Soc.* **2006**, *128* (24), 7706–7707. https://doi.org/10.1021/ja0618898.

(2) Gan, Z. Measuring Amide Nitrogen Quadrupolar Coupling by High-Resolution $^{14}N/^{13}C$ NMR Correlation under Magic-Angle Spinning. *Journal of the American Chemical Society* **2006**, *128* (18), 6040–6041. https://doi.org/10.1021/ja0578597.

(3) Aue, W. P.; Bartholdi, E.; Ernst, R. R. Two-dimensional Spectroscopy. Application to Nuclear Magnetic Resonance. *J. Chem. Phys.* **1976**, *64* (5), 2229–2246. https://doi.org/10.1063/1.432450.

(4) Bodenhausen, G.; Ruben, D. J. Natural Abundance Nitrogen-15 NMR by Enhanced Heteronuclear Spectroscopy. *Chem. Phys. Lett.* **1980**, *69* (1), 185–189.

(5) Caravatti, P.; Bodenhausen, G.; Ernst, R. R. Heteronuclear Solid-State Correlation Spectroscopy. *Chem. Phys. Lett.* **1982**, *89* (5), 363–367.

(6) Zumbulyadis, N. Hydrogen-Silicon Nuclear Spin Correlations in α-Si:H: A Two-Dimensional NMR Study. *Phys. Rev. B* **1986**, *33* (9), 6495–6496. https://doi.org/10.1103/PhysRevB.33.6495.

(7) Early, T. A.; John, B. K.; Johnson, L. F. Observation of Homonuclear Double-Quantum Correlations in Plastic Crystals Using Cross Polarization and Magic-Angle Spinning. *Journal of Magnetic Resonance* **1987**, *75* (1), 134–138. https://doi.org/10.1016/0022-2364(87)90321-0.

(8) Benn, R.; Grondey, H.; Brevard, C.; Pagelot, A. The Detection of Connectivities of Rare Spin-½ Nuclei in the Solid State Using Natural Abundance Samples: ^{13}C and ^{29}Si INADEQUATE and COSY Type Experiments. *J. Chem. Soc., Chem. Commun.* **1988**, No. 2, 102–103. https://doi.org/10.1039/C39880000102.

(9) Allman, T. The Observation of Two-Dimensional NMR Spectra of Crystalline Solids. The ^{31}P CP-MAS COSY and J-Resolved Spectra of a Phosphine Complex of Hg(II). *Journal of Magnetic Resonance (1969)* **1989**, *83* (3), 637–642. https://doi.org/10.1016/0022-2364(89)90359-4.

(10) Fyfe, C. A.; Gies, H.; Feng, Y. Demonstration of Three-Dimensional Lattice Connectivities in Zeolites by Two-Dimensional High Resolution Solid State n.m.r. Spectroscopy. *J. Chem. Soc., Chem. Commun.* **1989**, No. 17, 1240–1242. https://doi.org/10.1039/C39890001240.

(11) Franke, D.; Hudalla, C.; Eckert, H. Heteronuclear X-Y Double Quantum MAS NMR in Crystalline Inorganic Solids Applications for Indirect Detection and Spectral Editing of Rare-Spin Resonances. *Solid State Nuclear Magnetic Resonance* **1992**, *1* (1), 33–40. https://doi.org/10.1016/0926-2040(92)90007-V.

(12) Lesage, A.; Sakellariou, D.; Steuernagel, S.; Emsley, L. Carbon−Proton Chemical Shift Correlation in Solid-State NMR by Through-Bond Multiple-Quantum Spectroscopy. *J. Am. Chem. Soc.* **1998**, *120* (50), 13194–13201. https://doi.org/10.1021/ja983048+.

(13) Bennett, A. E.; Ok, J. H.; Griffin, R. G.; Vega, S. Chemical Shift Correlation Spectroscopy in Rotating Solids : Radiofrequency Dipolar Recoupling and Dipolar Exchange. *J. Chem. Phys.* **1992**, *96*, 8624–8627.

(14) Feike, M.; Demco, D. E.; Graf, R.; Gottwald, J.; Hafner, S.; Spiess, H. W. Broadband Multiple-Quantum NMR Spectroscopy. *Journal of Magnetic Resonance, Series A* **1996**, *122* (2), 214–221. https://doi.org/10.1006/jmra.1996.0197.

(15) Fyfe, C. A.; Grondey, H.; Mueller, K. T.; Wong-Moon, K. C.; Markus, T. Coherence Transfer Involving Quadrupolar Nuclei in Solids: Aluminum-27 - Phosphorus-31 Cross-Polarization NMR in the Molecular Sieve VPI-5. *J. Am. Chem. Soc.* **1992**, *114* (14), 5876–5878. https://doi.org/10.1021/ja00040a069.

(16) Fyfe, C. A.; Mueller, K. T.; Grondey, H.; Wong-Moon, K. C. Dipolar Dephasing between Quadrupolar and Spin-1/2 Nuclei. REDOR and TEDOR NMR Experiments on VPI-5. *Chemical Physics Letters* **1992**, *199* (1–2), 198–204. https://doi.org/10.1016/0009-2614(92)80069-N.

(17) Fyfe, C. A.; Meyer zu Altenschildesche, H.; Wong-Moon, K. C.; Grondey, H.; Chezeau, J. M. 1D and 2D Solid State NMR Investigations of the Framework Structure of As-Synthesized $AlPO_4$-14. *Solid state nuclear magnetic resonance* **1997**, *9* (2–4), 97–106.

(18) Chan, J. C. C.; Bertmer, M.; Eckert, H. Double-Quantum Cross-Polarization between Half-Integer Quadrupolar Spin Systems : ^{11}B-^{23}Na and ^{11}B-^{27}Al. *Chem. Phys. Lett.* **1998**, *292* (July), 154–160.

(19) Iuga, D.; Morais, C.; Gan, Z.; Neuville, D. R.; Cormier, L.; Massiot, D. NMR Heteronuclear Correlation between Quadrupolar Nuclei in Solids. *Journal of the American Chemical Society* **2005**, *127* (33), 11540–11541. https://doi.org/10.1021/ja052452n.

(20) Wang, S.; Paul, S. D.; Bull, L. High-Resolution Heteronuclear Correlation between Quadrupolar and Spin-1/2 Nuclei Using Multiple-Quantum Magic-Angle Spinning. *Journal of Magnetic Resonance* **1997**, *368* (125), 364–368.

(21) Wiench, J. W.; Pruski, M. Probing through Bond Connectivities with MQMAS NMR. *Solid State Nuclear Magnetic Resonance* **2004**, *26* (1), 51–55. https://doi.org/10.1016/j.ssnmr.2003.10.004.

(22) Duer, M. J.; Painter, A. J. Correlating Quadrupolar Nuclear Spins : A Multiple-Quantum NMR Approach. *Chem. Phys. Lett.* **1999**, *313* (November), 763–770.

(23) Hartmann, P.; Jäger, C.; Zwanziger, J. W. Off-Angle Correlation Spectroscopy Applied to Spin-1/2 and Quadrupolar Nuclei. *Solid state nuclear magnetic resonance* **1999**, *13* (4), 245–254.

(24) Rossini, A. J.; Hanrahan, M. P.; Thuo, M. Rapid Acquisition of Wideline MAS Solid-State NMR Spectra with Fast MAS, Proton Detection, and Dipolar HMQC Pulse Sequences. *Phys. Chem. Chem. Phys.* **2016**, *18* (36), 25284–25295. https://doi.org/10.1039/C6CP04279A.

(25) Lee, Y. K.; Kurur, N. D.; Helmle, M.; Johannessen, O. G.; Nielsen, N. C.; Levitt, M. H. Efficient Dipolar Recoupling in the NMR of Rotating Solids. A Sevenfold Symmetric Radiofrequency Pulse Sequence. *Chem. Phys. Lett.* **1995**, *242*, 304–309.

(26) Hohwy, M.; Jakobsen, H. J.; Edén, M.; Levitt, M. H.; Nielsen, N. C. Broadband Dipolar Recoupling in the Nuclear Magnetic Resonance of Rotating Solids: A Compensated C7 Pulse Sequence. *J. Chem. Phys.* **1998**, *108*, 2686–2694.

(27) Heise, B.; Leppert, J.; Ramachandran, R. REDOR with Adiabatic Dephasing Pulses. *Journal of Magnetic Resonance* **2000**, *146* (1), 181–187. https://doi.org/10.1006/jmre.2000.2129.

(28) Takegoshi, K.; Nakamura, S.; Terao, T. ^{13}C-^{1}H Dipolar-Assisted Rotational Resonance in Magic-Angle Spinning NMR. **2001**, *344* (August), 631–637.

(29) Ernst, M.; Meier, M. A.; Tuherm, T.; Samoson, A.; Meier, B. H. Low-Power High-Resolution Solid-State NMR of Peptides and Proteins. *Journal of the American Chemical Society* **2004**, *126* (15), 4764–4765. https://doi.org/10.1021/ja0494510.

(30) Robertson, A. J.; Pandey, M. K.; Marsh, A.; Nishiyama, Y.; Brown, S. P. The Use of a Selective Saturation Pulse to Suppress t_1 Noise in Two-Dimensional ^{1}H Fast Magic Angle Spinning Solid-State NMR Spectroscopy. *Journal of Magnetic Resonance* **2015**, *260*, 89–97. https://doi.org/10.1016/j.jmr.2015.09.005.

(31) Nagashima, H.; Lilly Thankamony, A. S.; Trébosc, J.; Pourpoint, F.; Lafon, O.; Amoureux, J. P. γ-Independent through-Space Hetero-Nuclear Correlation between Spin-1/2 and Quadrupolar Nuclei in Solids. *Solid State Nuclear Magnetic Resonance* **2017**, *84*, 216–226. https://doi.org/10.1016/j.ssnmr.2017.06.002.
(32) Ishii, Y.; Tycko, R. Sensitivity Enhancement in Solid State ^{15}N NMR by Indirect Detection with High-Speed Magic Angle Spinning. *Journal of Magnetic Resonance* **2000**, *142* (1), 199–204. https://doi.org/10.1006/jmre.1999.1976.
(33) Dusold, S.; Sebald, A. Dipolar Recoupling under Magic-Angle Spinning Conditions. *Annual Reports on NMR Spectroscopy* **2000**, *41* (185–264).
(34) Levitt, M. H. Symmetry-Based Pulse Sequences in Magic-Angle Spinning Solid-State NMR Symmetry-Based Pulse Sequences in Magic-Angle Spinning Solid-State NMR. In *Encyclopedia of Nuclear Magnetic Resonance*; Harris, R. K., Wasylishen, R. E., Eds.; Wiley: Chichester, 2002; Vol. 9, pp 165–196.
(35) Schnell, I. Dipolar Recoupling in Fast-MAS Solid-State NMR Spectroscopy. *Progress in Nuclear Magnetic Resonance Spectroscopy* **2004**, *45* (1–2), 145–207. https://doi.org/10.1016/j.pnmrs.2004.06.003.
(36) Jaroniec, C. P.; Harris, R. K.; Wasylishen, R. E. Dipolar Recoupling: Heteronuclear. In *Encyclopedia of Magnetic Resonance*; John Wiley & Sons, Ltd: Chichester, 2009. https://doi.org/10.1002/9780470034590.emrstm1011.
(37) Tycko, R.; Harris, R. K.; Wasylishen, R. E. Dipolar Recoupling: Homonuclear Experiments. In *Encyclopedia of Magnetic Resonance*; John Wiley & Sons, Ltd: Chichester, 2009. https://doi.org/10.1002/9780470034590.emrstm1070.
(38) De Paëpe, G. Dipolar Recoupling in Magic Angle Spinning Solid-State Nuclear Magnetic Resonance. *Annual Review of Physical Chemistry* **2012**, *63* (1), 661–684. https://doi.org/10.1146/annurev-physchem-032511-143726.
(39) Edén, M. Advances in Symmetry-Based Pulse Sequences in Magic-Angle Spinning Solid-State NMR. In *eMagRes*; John Wiley & Sons, Ltd, 2013; Vol. 2, pp 351–364. https://doi.org/10.1002/9780470034590.emrstm1326.
(40) Liang, L.; Ji, Y.; Chen, K.; Gao, P.; Zhao, Z.; Hou, G. Solid-State NMR Dipolar and Chemical Shift Anisotropy Recoupling Techniques for Structural and Dynamical Studies in Biological Systems. *Chem. Rev.* **2022**, *122* (10), 9880–9942. https://doi.org/10.1021/acs.chemrev.1c00779.
(41) Ahlawat, S.; Mote, K. R.; Lakomek, N.-A.; Agarwal, V. Solid-State NMR: Methods for Biological Solids. *Chem. Rev.* **2022**, *122* (10), 9643–9737. https://doi.org/10.1021/acs.chemrev.1c00852.
(42) Sakellariou, D.; Emsley, L. Through-Bond Experiments in Solids. In *Encyclopedia of Magnetic Resonance*; Harris, R. K., Wasylishen, R. E., Eds.; John Wiley & Sons, Ltd: Chichester, 2007. https://doi.org/10.1002/9780470034590.emrstm0566.
(43) Lesage, A. Indirect Coupling and Connectivity. In *Encyclopedia of Magnetic Resonance*; Harris, R. K., Wasylishen, R. E., Eds.; John Wiley & Sons, Ltd: Chichester, 2008. https://doi.org/10.1002/9780470034590.emrstm1012.
(44) Amoureux, J. P.; Trébosc, J.; Delevoye, L.; Lafon, O.; Hu, B.; Wang, Q. Correlation NMR Spectroscopy Involving Quadrupolar Nuclei. *Solid State Nuclear Magnetic Resonance* **2009**, *35* (1), 12–18. https://doi.org/10.1016/j.ssnmr.2008.11.004.
(45) Deschamps, M.; Massiot, D. Correlation Experiments Involving Half-Integer Quadrupolar Nuclei. In *Encyclopedia of Magnetic Resonance*; Harris, R. K., Wasylishen, R. E., Eds.; John Wiley & Sons, Ltd: Chichester, 2011. https://doi.org/10.1002/9780470034590.emrstm1207.
(46) Tricot, G.; Trébosc, J.; Pourpoint, F.; Gauvin, R.; Delevoye, L. The *D*-HMQC MAS-NMR Technique : An Efficient Tool for the Editing of Through-Space Correlation Spectra Between Quadrupolar and Spin-1/2. *Annual Reports on NMR Spectroscopy* **2014**, *81*, 145–184. https://doi.org/10.1016/B978-0-12-800185-1.00004-8.
(47) Edén, M. Recent Progress in Homonuclear Correlation Spectroscopy of Quadrupolar Nuclei. In *Modern Magnetic Resonance*; Webb, G. A., Ed.; Springer International Publishing: Cham, 2017; pp 1–33. https://doi.org/10.1007/978-3-319-28275-6_104-1.

(48) Pourpoint, F.; Lafon, O.; Gauvin, R.; Amoureux, J.-P.; Delevoye, L. Chapter 4:Two-Dimensional Methods for Half-Integer Quadrupolar Nuclei. In *Modern Methods in Solid-state NMR*; 2018; pp 97–133. https://doi.org/10.1039/9781788010467-00097.
(49) Edén, M. NMR Studies of Oxide-Based Glasses. *Annu. Rep. Prog. Chem., Sect. C: Phys. Chem.* **2012**, *108* (1), 177–221. https://doi.org/10.1039/C2PC90006H.
(50) Tricot, G. Chapter Two - Mixed Network Phosphate Glasses: Seeing Beyond the 1D ^{31}P MAS-NMR Spectra With 2D X/^{31}P NMR Correlation Maps. In *Annual Reports on NMR Spectroscopy*; Webb, G. A., Ed.; Academic Press, 2019; Vol. 96, pp 35–75. https://doi.org/10.1016/bs.arnmr.2018.08.003.
(51) Edén, M. Chapter Four - Update on ^{27}Al NMR Studies of Aluminosilicate Glasses. In *Annual Reports on NMR Spectroscopy*; Atta-ur-Rahman, Ed.; Academic Press, 2020; Vol. 101, pp 285–410. https://doi.org/10.1016/bs.arnmr.2020.07.002.
(52) Nagashima, H.; Martineau-Corcos, C.; Tricot, G.; Trébosc, J.; Pourpoint, F.; Amoureux, J.-P.; Lafon, O. Chapter Four - Recent Developments in NMR Studies of Aluminophosphates. In *Annual Reports on NMR Spectroscopy*; Webb, G. A., Ed.; Academic Press, 2018; Vol. 94, pp 113–185. https://doi.org/10.1016/bs.arnmr.2017.12.004.
(53) Blanc, F.; Copéret, C.; Lesage, A.; Emsley, L. High Resolution Solid State NMR Spectroscopy in Surface Organometallic Chemistry: Access to Molecular Understanding of Active Sites of Well-Defined Heterogeneous Catalysts. *Chemical Society reviews* **2008**, *37* (3), 518–526. https://doi.org/10.1039/b612793m.
(54) Grekov, D.; Vancompernolle, T.; Taoufik, M.; Delevoye, L.; Gauvin, R. M. Solid-State NMR of Quadrupolar Nuclei for Investigations into Supported Organometallic Catalysts: Scope and Frontiers. *Chem. Soc. Rev.* **2018**, *47* (8), 2572–2590. https://doi.org/10.1039/C7CS00682A.
(55) Kobayashi, T.; Pruski, M. Spatial Distribution of Silica-Bound Catalytic Organic Functional Groups Can Now Be Revealed by Conventional and DNP-Enhanced Solid-State NMR Methods. *ACS Catal.* **2019**, *9* (8), 7238–7249. https://doi.org/10.1021/acscatal.9b02017.
(56) Qi, G.; Wang, Q.; Xu, J.; Deng, F. Solid-State NMR Studies of Internuclear Correlations for Characterizing Catalytic Materials. *Chem. Soc. Rev.* **2021**, *50* (15), 8382–8399. https://doi.org/10.1039/D0CS01130D.
(57) Xu, J.; Wang, Q.; Deng, F. Metal Active Sites and Their Catalytic Functions in Zeolites: Insights from Solid-State NMR Spectroscopy. *Acc. Chem. Res.* **2019**, *52* (8), 2179–2189. https://doi.org/10.1021/acs.accounts.9b00125.
(58) Li, S.; Lafon, O.; Wang, W.; Wang, Q.; Wang, X.; Li, Y.; Xu, J.; Deng, F. Recent Advances of Solid-State NMR Spectroscopy for Microporous Materials. *Advanced Materials* **2020**, *32* (44), 2002879. https://doi.org/10.1002/adma.202002879.
(59) Wang, W.; Xu, J.; Deng, F. Recent Advances in Solid-State NMR of Zeolite Catalysts. *National Science Review* **2022**, nwac155. https://doi.org/10.1093/nsr/nwac155.
(60) He, C.; Li, S.; Xiao, Y.; Xu, J.; Deng, F. Application of Solid-State NMR Techniques for Structural Characterization of Metal-Organic Frameworks. *Solid State Nuclear Magnetic Resonance* **2022**, *117*, 101772. https://doi.org/10.1016/j.ssnmr.2022.101772.
(61) Fayon, F.; Roiland, C.; Emsley, L.; Massiot, D. Triple-Quantum Correlation NMR Experiments in Solids Using J-Couplings. *Journal of magnetic resonance (San Diego, Calif. : 1997)* **2006**, *179* (1), 49–57. https://doi.org/10.1016/j.jmr.2005.11.002.
(62) Fyfe, C. A.; Gies, H.; Feng, Y. Three-Dimensional Lattice Connectivities from Two-Dimensional High-Resolution Solid-State NMR. Silicon-29 Magic Angle Spinning NMR Investigation of the Silicate Lattice of Zeolite ZSM-39 (Dodecasil 3C). *J. Am. Chem. Soc.* **1989**, *111* (20), 7702–7707. https://doi.org/10.1021/ja00202a006.
(63) Baldus, M.; Meier, B. H. Total Correlation Spectroscopy in the Solid State. The Use of Scalar Couplings to Determine the Through-Bond Connectivity. *Journal of Magnetic Resonance, Series A* **1996**, *121* (1), 65–69. https://doi.org/10.1006/jmra.1996.0137.

(64) Chan, J. C. C.; Brunklaus, G. R Sequences for the Scalar-Coupling Mediated Homonuclear Correlation Spectroscopy under Fast Magic-Angle Spinning. *Chemical Physics Letters* **2001**, *349* (1), 104–112. https://doi.org/10.1016/S0009-2614(01)01132-0.

(65) Helluy, X.; Marichal, C.; Sebald, A. Through-Bond Indirect and Through-Space Direct Dipolar Coupling ^{31}P MAS NMR Constraints for Spectral Assignment in the Cubic 3 × 3 × 3 Superstructure of TiP_2O_7. *J. Phys. Chem. B* **2000**, *104* (13), 2836–2845. https://doi.org/10.1021/jp993626o.

(66) Bax, A.; Freeman, R.; Kempsell, S. P. Natural Abundance Carbon-13-Carbon-13 Coupling Observed via Double-Quantum Coherence. *J. Am. Chem. Soc.* **1980**, *102* (14), 4849–4851. https://doi.org/10.1021/ja00534a056.

(67) Bax, A.; Freeman, R.; Frenkiel, T. A. An NMR Technique for Tracing out the Carbon Skeleton of an Organic Molecule. *J. Am. Chem. Soc.* **1981**, *103* (8), 2102–2104. https://doi.org/10.1021/ja00398a044.

(68) Freeman, R.; Frenkiel, T.; Rubin, M. B. Structure of a Photodimer Determined by Natural-Abundance ^{13}C-^{13}C Coupling. *J. Am. Chem. Soc.* **1982**, *104* (20), 5545–5547. https://doi.org/10.1021/ja00384a072.

(69) Fyfe, C. A.; Feng, Y.; Gies, H.; Grondey, H.; Kokotailo, G. T. Natural-Abundance Two-Dimensional Solid-State Silicon-29 NMR Investigations of Three-Dimensional Lattice Connectivities in Zeolite Structures. *J. Am. Chem. Soc.* **1990**, *112* (9), 3264–3270. https://doi.org/10.1021/ja00165a002.

(70) Fyfe, C. A.; Feng, Y.; Grondey, H. Evaluation of Chemical Shift—Structure Correlations from a Combination of X-Ray Diffraction and 2D MAS NMR Data for Highly Siliceous Zeolite Frameworks. *Microporous Materials* **1993**, *1* (6), 401–411. https://doi.org/10.1016/0927-6513(93)80034-R.

(71) Lesage, A.; Bardet, M.; Emsley, L. Through-Bond Carbon−Carbon Connectivities in Disordered Solids by NMR. *J. Am. Chem. Soc.* **1999**, *121* (47), 10987–10993. https://doi.org/10.1021/ja992272b.

(72) Sakellariou, D.; Brown, S. P.; Lesage, A.; Hediger, S.; Bardet, M.; Meriles, C. A.; Pines, A.; Emsley, L.; Lyon, D.; Chimie, S. D.; Grenoble, C. E. A. High-Resolution NMR Correlation Spectra of Disordered Solids Areas of Chemistry over the Last 50 Years , and Today It Has. **2003**, No. 2, 4376–4380.

(73) Fayon, F.; Massiot, D.; Levitt, M. H.; Titman, J. J.; Gregory, D. H.; Duma, L.; Emsley, L.; Brown, S. P. Through-Space Contributions to Two-Dimensional Double-Quantum J Correlation NMR Spectra of Magic-Angle-Spinning Solids. *J. Chem. Phys.* **2005**, *122* (19), 194313. https://doi.org/10.1063/1.1898219.

(74) Fayon, F.; Le Saout, G.; Emsley, L.; Massiot, D. Through-Bond Phosphorus-Phosphorus Connectivities in Crystalline and Disordered Phosphates by Solid-State NMR. *Chemical communications (Cambridge, England)* **2002**, No. 16, 1702–1703.

(75) Fayon, F.; King, I. J.; Harris, R. K.; Gover, R. K. B.; Evans, J. S. O.; Massiot, D. Characterization of the Room-Temperature Structure of SnP_2O_7 by ^{31}P Through-Space and Through-Bond NMR Correlation Spectroscopy. *Chem. Mater.* **2003**, *15* (11), 2234–2239. https://doi.org/10.1021/cm031009d.

(76) Fayon, F.; King, I. J.; Harris, R. K.; Evans, J. S. O.; Massiot, D. Application of the Through-Bond Correlation NMR Experiment to the Characterization of Crystalline and Disordered Phosphates. *Comptes Rendus Chimie* **2004**, *7* (3), 351–361. https://doi.org/10.1016/j.crci.2003.10.019.

(77) van Wüllen, L.; Tricot, G.; Wegner, S. An Advanced NMR Protocol for the Structural Characterization of Aluminophosphate Glasses. *Solid State Nuclear Magnetic Resonance* **2007**, *32* (2), 44–52. https://doi.org/10.1016/j.ssnmr.2007.07.004.

(78) Florian, P.; Fayon, F.; Massiot, D. ^2JSi−O−Si Scalar Spin−Spin Coupling in the Solid State: Crystalline and Glassy Wollastonite $CaSiO_3$. *J. Phys. Chem. C* **2009**, *113* (6), 2562–2572. https://doi.org/10.1021/jp8078309.

(79) Hedin, N.; Graf, R.; Christiansen, S. C.; Gervais, C.; Hayward, R. C.; Eckert, J.; Chmelka, B. F. Structure of a Surfactant-Templated Silicate Framework in the Absence of 3D Crystallinity. *J. Am. Chem. Soc.* **2004**, *126* (30), 9425–9432. https://doi.org/10.1021/ja040030s.

(80) Lee, D.; Monin, G.; Duong, N. T.; Lopez, I. Z.; Bardet, M.; Mareau, V.; Gonon, L.; De Paëpe, G. Untangling the Condensation Network of Organosiloxanes on Nanoparticles Using 2D ^{29}Si–^{29}Si Solid-State NMR Enhanced by Dynamic Nuclear Polarization. *J. Am. Chem. Soc.* **2014**, *136*, 13781–13788. https://doi.org/10.1021/ja506688m.

(81) Rankin, A. G. M.; Webb, P. B.; Dawson, D. M.; Viger-Gravel, J.; Walder, B. J.; Emsley, L.; Ashbrook, S. E. Determining the Surface Structure of Silicated Alumina Catalysts via Isotopic Enrichment and Dynamic Nuclear Polarization Surface-Enhanced NMR Spectroscopy. *J. Phys. Chem. C* **2017**, *121* (41), 22977–22984. https://doi.org/10.1021/acs.jpcc.7b08137.

(82) Smeets, S.; Berkson, Z. J.; Xie, D.; Zones, S. I.; Wan, W.; Zou, X.; Hsieh, M.-F.; Chmelka, B. F.; McCusker, L. B.; Baerlocher, C. Well-Defined Silanols in the Structure of the Calcined High-Silica Zeolite SSZ-70: New Understanding of a Successful Catalytic Material. *J. Am. Chem. Soc.* **2017**, *139* (46), 16803–16812. https://doi.org/10.1021/jacs.7b08810.

(83) Rankin, A. G. M.; Trébosc, J.; Pourpoint, F.; Amoureux, J.-P.; Lafon, O. Recent Developments in MAS DNP-NMR of Materials. *Solid State Nuclear Magnetic Resonance* **2019**, *101*, 116–143. https://doi.org/10.1016/j.ssnmr.2019.05.009.

(84) Lesage, A.; Lelli, M.; Gajan, D.; Caporini, M. A.; Vitzthum, V.; Miéville, P.; Alauzun, J.; Roussey, A.; Thieuleux, C.; Mehdi, A.; Bodenhausen, G.; Copéret, C.; Emsley, L. Surface Enhanced NMR Spectroscopy by Dynamic Nuclear Polarization. *J. Am. Chem. Soc.* **2010**, *132* (44), 15459–15461. https://doi.org/10.1021/ja104771z.

(85) Lafon, O.; Rosay, M.; Aussenac, F.; Lu, X.; Trébosc, J.; Cristini, O.; Kinowski, C.; Touati, N.; Vezin, H.; Amoureux, J.-P. Beyond the Silica Surface by Direct Silicon-29 Dynamic Nuclear Polarization. *Angew. Chem. Int. Ed.* **2011**, *50* (36), 8367–8370. https://doi.org/10.1002/anie.201101841.

(86) Carnahan, S. L.; Venkatesh, A.; Perras, F. A.; Wishart, J. F.; Rossini, A. J. High-Field Magic Angle Spinning Dynamic Nuclear Polarization Using Radicals Created by γ-Irradiation. *J. Phys. Chem. Lett.* **2019**, *10* (17), 4770–4776. https://doi.org/10.1021/acs.jpclett.9b01655.

(87) Malfait, W. J.; Halter, W. E.; Morizet, Y.; Meier, B. H.; Verel, R. Structural Control on Bulk Melt Properties: Single and Double Quantum ^{29}Si NMR Spectroscopy on Alkali-Silicate Glasses. *Geochimica et Cosmochimica Acta* **2007**, *71* (24), 6002–6018. https://doi.org/10.1016/j.gca.2007.09.011.

(88) Cadars, S.; Mifsud, N.; Lesage, A.; Epping, J. D.; Hedin, N.; Chmelka, B. F.; Emsley, L. Dynamics and Disorder in Surfactant-Templated Silicate Layers Studied by Solid-State NMR Dephasing Times and Correlated Line Shapes. *J. Phys. Chem. C* **2008**, *112* (25), 9145–9154. https://doi.org/10.1021/jp711398h.

(89) Cadars, S.; Sein, J.; Duma, L.; Lesage, A.; Pham, T. N.; Baltisberger, J. H.; Brown, S. P.; Emsley, L. The Refocused INADEQUATE MAS NMR Experiment in Multiple Spin-Systems: Interpreting Observed Correlation Peaks and Optimising Lineshapes. *Journal of magnetic resonance (San Diego, Calif. : 1997)* **2007**, *188* (1), 24–34. https://doi.org/10.1016/j.jmr.2007.05.016.

(90) Wiench, J. W.; Lin, V. S.-Y.; Pruski, M. ^{29}Si NMR in Solid State with CPMG Acquisition under MAS. *J Magn Reson* **2008**, *193* (2), 233–242. https://doi.org/10.1016/j.jmr.2008.05.007.

(91) Hanrahan, M. P.; Chen, Y.; Blome-Fernández, R.; Stein, J. L.; Pach, G. F.; Adamson, M. A. S.; Neale, N. R.; Cossairt, B. M.; Vela, J.; Rossini, A. J. Probing the Surface Structure of Semiconductor Nanoparticles by DNP SENS with Dielectric Support Materials. *J. Am. Chem. Soc.* **2019**, *141* (39), 15532–15546. https://doi.org/10.1021/jacs.9b05509.

(92) Deschamps, M.; Fayon, F.; Montouillout, V.; Massiot, D. Through-Bond Homonuclear Correlation Experiments in Solid-State NMR Applied to Quadrupolar Nuclei in Al-O-P-O-Al Chains. *Chemical communications (Cambridge, England)* **2006**, No. 18, 1924–1925. https://doi.org/10.1039/b600514d.

(93) Raleigh, D. P.; Levitt, M. H.; Griffin, R. G. Rotational Resonance in Solid State NMR. *Chemical Physics Letters* **1988**, *146* (1), 71–76. https://doi.org/10.1016/0009-2614(88)85051-6.
(94) Colombo, M. G.; Meier, B. H.; Ernst, R. R. Rotor-Driven Spin Diffusion in Natural-Abundance 13C Spin Systems. *Chemical Physics Letters* **1988**, *146* (3), 189–196. https://doi.org/10.1016/0009-2614(88)87429-3.
(95) Levitt, M. H.; Raleigh, D. P.; Creuzet, F.; Griffin, R. G. Theory and Simulations of Homonuclear Spin Pair Systems in Rotating Solids. *J. Chem. Phys.* **1990**, *92* (11), 6347–6364. https://doi.org/10.1063/1.458314.
(96) Jardón-Álvarez, D.; Kahn, N.; Houben, L.; Leskes, M. Oxygen Vacancy Distribution in Yttrium-Doped Ceria from 89Y–89Y Correlations via Dynamic Nuclear Polarization Solid-State NMR. *J. Phys. Chem. Lett.* **2021**, *12* (11), 2964–2969. https://doi.org/10.1021/acs.jpclett.1c00221.
(97) Bayro, M. J.; Huber, M.; Ramachandran, R.; Davenport, T. C.; Meier, B. H.; Ernst, M.; Griffin, R. G. Dipolar Truncation in Magic-Angle Spinning NMR Recoupling Experiments. *The Journal of chemical physics* **2009**, *130* (11), 114506. https://doi.org/10.1063/1.3089370.
(98) Ishii, Y. ^{13}C–^{13}C Dipolar Recoupling under Very Fast Magic Angle Spinning in Solid-State Nuclear Magnetic Resonance: Applications to Distance Measurements, Spectral Assignments, and High-Throughput Secondary-Structure Determination. *J. Chem. Phys.* **2001**, *114* (19), 8473–8483.
(99) Alam, T. M.; Brow, R. K. Local Structure and Connectivity in Lithium Phosphate Glasses: A Solid-State ^{31}P MAS NMR and 2D Exchange Investigation. *Journal of Non-Crystalline Solids* **1998**, *223* (1), 1–20. https://doi.org/10.1016/S0022-3093(97)00345-1.
(100) Trébosc, J.; Wiench, J. W.; Huh, S.; Lin, V. S.-Y.; Pruski, M. Solid-State NMR Study of MCM-41-Type Mesoporous Silica Nanoparticles. *Journal of the American Chemical Society* **2005**, *127* (9), 3057–3068. https://doi.org/10.1021/ja043567e.
(101) Dupke, S.; Langer, T.; Pöttgen, R.; Winter, M.; Eckert, H. Structural and Dynamic Characterization of Li₁₂Si$_7$ and Li₁₂Ge$_7$ using solid state NMR. *Solid State Nuclear Magnetic Resonance* **2012**, *42*, 17–25. https://doi.org/10.1016/j.ssnmr.2011.09.002.
(102) Saalwächter, K.; Lange, F.; Matyjaszewski, K.; Huang, C.-F.; Graf, R. BaBa-Xy16: Robust and Broadband Homonuclear DQ Recoupling for Applications in Rigid and Soft Solids up to the Highest MAS Frequencies. *Journal of magnetic resonance (San Diego, Calif. : 1997)* **2011**, *212* (1), 204–215. https://doi.org/10.1016/j.jmr.2011.07.001.
(103) Blanco, F. J.; Tycko, R. Determination of Polypeptide Backbone Dihedral Angles in Solid State NMR by Double Quantum ^{13}C Chemical Shift Anisotropy Measurements. *Journal of Magnetic Resonance* **2001**, *149* (1), 131–138. https://doi.org/10.1006/jmre.2000.2281.
(104) Tseng, Y.-H.; Mou, Y.; Mou, C.-Y.; Chan, J. C. C. Double-Quantum NMR Spectroscopy Based on Finite Pulse RFDR. *Solid state nuclear magnetic resonance* **2005**, *27* (4), 266–270. https://doi.org/10.1016/j.ssnmr.2005.02.005.
(105) Hohwy, M.; Rienstra, C. M.; Jaroniec, C. P.; Griffin, R. G. Fivefold Symmetric Homonuclear Dipolar Recoupling in Rotating Solids: Application to Double Quantum Spectroscopy. *J. Chem. Phys.* **1999**, *110*, 7983.
(106) Kristiansen, P. E.; Carravetta, M.; Lai, W. C.; Levitt, M. H. A Robust Pulse Sequence for the Determination of Small Homonuclear Dipolar Couplings in Magic-Angle Spinning NMR. *Chemical Physics Letters* **2004**, *390* (1–3), 1–7. https://doi.org/10.1016/j.cplett.2004.03.075.
(107) Brouwer, D. H.; Kristiansen, P. E.; Fyfe, C. A.; Levitt, M. H. Symmetry-Based ^{29}Si Dipolar Recoupling Magic Angle Spinning NMR Spectroscopy: A New Method for Investigating Three-Dimensional Structures of Zeolite Frameworks. *Journal of the American Chemical Society* **2005**, *127* (2), 542–543. https://doi.org/10.1021/ja043228l.
(108) Dorn, R. W.; Marro, E. A.; Hanrahan, M. P.; Klausen, R. S.; Rossini, A. J. Investigating the Microstructure of Poly(Cyclosilane) by ^{29}Si Solid-State NMR Spectroscopy and DFT Calculations. *Chem. Mater.* **2019**, *31* (21), 9168–9178. https://doi.org/10.1021/acs.chemmater.9b03606.

(109) Tischendorf, B.; Otaigbe, J. U.; Wiench, J. W.; Pruski, M.; Sales, B. C. A Study of Short and Intermediate Range Order in Zinc Phosphate Glasses. *Journal of Non-Crystalline Solids* **2001**, *282* (2), 147–158. https://doi.org/10.1016/S0022-3093(01)00350-7.

(110) Mafra, L.; Siegel, R.; Fernandez, C.; Schneider, D.; Aussenac, F.; Rocha, J. High-Resolution ^{1}H Homonuclear Dipolar Recoupling NMR Spectra of Biological Solids at MAS Rates up to 67 KHz. *Journal of magnetic resonance (San Diego, Calif. : 1997)* **2009**, *199* (1), 111–114. https://doi.org/10.1016/j.jmr.2009.04.004.

(111) Devautour-Vinot, S.; Maurin, G.; Serre, C.; Horcajada, P.; Paula da Cunha, D.; Guillerm, V.; de Souza Costa, E.; Taulelle, F.; Martineau, C. Structure and Dynamics of the Functionalized MOF Type UiO-66(Zr): NMR and Dielectric Relaxation Spectroscopies Coupled with DFT Calculations. *Chem. Mater.* **2012**, *24* (11), 2168–2177. https://doi.org/10.1021/cm300863c.

(112) Goswami, M.; Madhu, P. K.; Dittmer, J.; Nielsen, N. C.; Ganapathy, S. Sensitivity Enhancement of ^{29}Si Double-Quantum Dipolar Recoupling Spectroscopy by Carr–Purcell–Meiboom–Gill Acquisition Method. *Chemical Physics Letters* **2009**, *478* (4–6), 287–291. https://doi.org/10.1016/j.cplett.2009.07.066.

(113) Kobayashi, T.; Singappuli-Arachchige, D.; Wang, Z.; Slowing, I. I.; Pruski, M. Spatial Distribution of Organic Functional Groups Supported on Mesoporous Silica Nanoparticles: A Study by Conventional and DNP-Enhanced ^{29}Si Solid-State NMR. *Phys. Chem. Chem. Phys.* **2017**, *19* (3), 1781–1789. https://doi.org/10.1039/C6CP07642D.

(114) Hanrahan, M. P.; Stein, J. L.; Park, N.; Cossairt, B. M.; Rossini, A. J. Elucidating the Location of Cd^{2+} in Post-Synthetically Treated InP Quantum Dots Using Dynamic Nuclear Polarization ^{31}P and ^{113}Cd Solid-State NMR Spectroscopy. *The Journal of Physical Chemistry C* **2021**. https://doi.org/10.1021/acs.jpcc.0c09601.

(115) Martineau, C.; Fayon, F.; Legein, C.; Buzaré, J.-Y.; Goutenoire, F.; Suard, E. Neutron Powder Diffraction, Multinuclear, and Multidimensional NMR Structural Investigation of $Pb_5Ga_3F_{19}$. *Inorganic chemistry* **2008**, *47* (23), 10895–10905. https://doi.org/10.1021/ic801044j.

(116) Wiench, J. W.; Michon, C.; Ellern, A.; Hazendonk, P.; Iuga, A.; Angelici, R. J.; Pruski, M. Solid-State NMR Investigations of the Immobilization of a BF_4^- Salt of a Palladium(II) Complex on Silica. *Journal of the American Chemical Society* **2009**, *131* (33), 11801–11810. https://doi.org/10.1021/ja902982u.

(117) Wang, Q.; Hu, B.; Fayon, F.; Trébosc, J.; Legein, C.; Lafon, O.; Deng, F.; Amoureux, J.-P. Double-Quantum ^{19}F-^{19}F Dipolar Recoupling at Ultra-Fast Magic Angle Spinning NMR: Application to the Assignment of ^{19}F NMR Spectra of Inorganic Fluorides. *Physical chemistry chemical physics : PCCP* **2009**, *11* (44), 10391–10395. https://doi.org/10.1039/b914468d.

(118) Wang, Q.; Hu, B.; Lafon, O.; Trébosc, J.; Deng, F.; Amoureux, J.-P. Homonuclear Dipolar Recoupling under Ultra-Fast Magic-Angle Spinning: Probing ^{19}F–^{19}F Proximities by Solid-State NMR. *Journal of Magnetic Resonance* **2010**, *203* (1), 113–128. https://doi.org/10.1016/j.jmr.2009.12.009.

(119) Schnell, I.; Lupulescu, A.; Hafner, S.; Demco, D. E.; Spiess, H. W. Resolution Enhancement in Multiple-Quantum MAS NMR Spectroscopy. *Journal of Magnetic Resonance* **1998**, *133* (1), 61–69. https://doi.org/10.1006/jmre.1998.1432.

(120) Friedrich, U.; Schnell, I.; Demco, D. E.; Spiess, H. W. Triple-Quantum NMR Spectroscopy in Dipolar Solids. *Chemical Physics Letters* **1998**, *285* (1), 49–58. https://doi.org/10.1016/S0009-2614(97)01292-X.

(121) Shantz, D. F.; Schmedt auf der Günne, J.; Koller, H.; Lobo, R. F. Multiple-Quantum ^{1}H MAS NMR Studies of Defect Sites in As-Made All-Silica ZSM-12 Zeolite. *J. Am. Chem. Soc.* **2000**, *122* (28), 6659–6663. https://doi.org/10.1021/ja000374s.

(122) Caravatti, P.; Neuenschwander, P.; Ernst, R. R. Characterization of Heterogeneous Polymer Blends by Two-Dimensional Proton Spin Diffusion Spectroscopy. *Macromolecules* **1985**, *18* (1), 119–122. https://doi.org/10.1021/ma00143a020.

(123) Schwerk, U.; Michel, D. High Resolution NMR Spectroscopy on Adsorbed Molecules in One and Two Dimensions. *Zeitschrift für Physikalische Chemie* **1995**, *189* (1), 29–42. https://doi.org/10.1524/zpch.1995.189.Part_1.029.
(124) Schwerk, U.; Michel, D. ^{1}H NOESY NMR on Adsorbed Molecules. *J. Phys. Chem.* **1996**, *100* (1), 352–356. https://doi.org/10.1021/jp952125+.
(125) Du, L.-S.; Wang, F.; Grey, C. P. High-Resolution ^{19}F MAS and ^{19}F–^{113}Cd REDOR NMR Study of Oxygen/Fluorine Ordering in Oxyfluorides. *Journal of Solid State Chemistry* **1998**, *140* (2), 285–294. https://doi.org/10.1006/jssc.1998.7888.
(126) Du, L.-S.; Levitt, M. H.; Grey, C. P. High-Order Spin Diffusion Mechanisms in ^{19}F 2-D NMR of Oxyfluorides. *Journal of Magnetic Resonance* **1999**, *140* (1), 242–249. https://doi.org/10.1006/jmre.1999.1849.
(127) Deschamps, M.; Fayon, F.; Cadars, S.; Rollet, A.-L.; Massiot, D. ^{1}H and ^{19}F Ultra-Fast MAS Double-Quantum Single-Quantum NMR Correlation Experiments Using Three-Spin Terms of the Dipolar Homonuclear Hamiltonian. *Physical chemistry chemical physics : PCCP* **2011**, *13* (17), 8024–8030. https://doi.org/10.1039/c0cp02202k.
(128) Martineau, C.; Mellot-Draznieks, C.; Taulelle, F. NMR Crystallography of $AlPO_4$-CJ2: From the Topological Network to the Local (OH)/F Distribution. *Physical Chemistry Chemical Physics* **2011**, *13* (40), 18078–18087. https://doi.org/10.1039/c1cp22424g.
(129) Krishna, A.; Akhavan Kazemi, M. A.; Sliwa, M.; Reddy, G. N. M.; Delevoye, L.; Lafon, O.; Felten, A.; Do, M. T.; Gottis, S.; Sauvage, F. Defect Passivation via the Incorporation of Tetrapropylammonium Cation Leading to Stability Enhancement in Lead Halide Perovskite. *Advanced Functional Materials* **2020**, *30* (13), 1909737. https://doi.org/10.1002/adfm.201909737.
(130) Kobayashi, T.; Slowing, I. I.; Pruski, M. Measuring Long-Range ^{13}C–^{13}C Correlations on a Surface under Natural Abundance Using Dynamic Nuclear Polarization-Enhanced Solid-State Nuclear Magnetic Resonance. *J. Phys. Chem. C* **2017**, *121* (44), 24687–24691. https://doi.org/10.1021/acs.jpcc.7b08841.
(131) Johnson, R. L.; Perras, F. A.; Kobayashi, T.; Schwartz, T. J.; Dumesic, J. A.; Shanks, B. H.; Pruski, M. Identifying Low-Coverage Surface Species on Supported Noble Metal Nanoparticle Catalysts by DNP-NMR. *Chem. Commun.* **2016**, *52* (9), 1859–1862. https://doi.org/10.1039/C5CC06788J.
(132) Szeverenyi, N. M.; Sullivan, M. J.; Maciel, G. E. Observation of Spin Exchange by Two-Dimensional Fourier Transform ^{13}C Cross Polarization-Magic-Angle Spinning. *Journal of Magnetic Resonance (1969)* **1982**, *47* (3), 462–475. https://doi.org/10.1016/0022-2364(82)90213-X.
(133) Takegoshi, K.; Nakamura, S.; Terao, T. ^{13}C–^{1}H Dipolar-Driven ^{13}C–^{13}C Recoupling without ^{13}C Rf Irradiation in Nuclear Magnetic Resonance of Rotating Solids. *The Journal of Chemical Physics* **2003**, *118* (5), 2325. https://doi.org/10.1063/1.1534105.
(134) Morcombe, C. R.; Gaponenko, V.; Byrd, R. A.; Zilm, K. W. Diluting Abundant Spins by Isotope Edited Radio Frequency Field Assisted Diffusion. *Journal of the American Chemical Society* **2004**, *126* (23), 7196–7197. https://doi.org/10.1021/ja047919t.
(135) Weingarth, M.; Demco, D. E.; Bodenhausen, G.; Tekely, P. Improved Magnetization Transfer in Solid-State NMR with Fast Magic Angle Spinning. *Chemical Physics Letters* **2009**, *469* (4–6), 342–348. https://doi.org/10.1016/j.cplett.2008.12.084.
(136) Weingarth, M.; Bodenhausen, G.; Tekely, P. Broadband Magnetization Transfer Using Moderate Radio-Frequency Fields for NMR with Very High Static Fields and Spinning Speeds. *Chemical Physics Letters* **2010**, *488* (1–3), 10–16. https://doi.org/10.1016/j.cplett.2010.01.072.
(137) Chowdhury, A. D.; Houben, K.; Whiting, G. T.; Chung, S.-H.; Baldus, M.; Weckhuysen, B. M. Electrophilic Aromatic Substitution over Zeolites Generates Wheland-Type Reaction Intermediates. *Nat Catal* **2018**, *1* (1), 23–31. https://doi.org/10.1038/s41929-017-0002-4.

(138) Yi, X.; Ko, H.-H.; Deng, F.; Liu, S.-B.; Zheng, A. Solid-State ^{31}P NMR Mapping of Active Centers and Relevant Spatial Correlations in Solid Acid Catalysts. *Nat Protoc* **2020**, *15* (10), 3527–3555. https://doi.org/10.1038/s41596-020-0385-6.
(139) Edén, M. Homonuclear Dipolar Recoupling of Half-Integer Spin Quadrupolar Nuclei: Techniques and Applications. *Solid State Nuclear Magnetic Resonance* **2009**, *36* (1), 1–10. https://doi.org/10.1016/j.ssnmr.2009.06.005.
(140) Edén, M.; Grinshtein, J.; Frydman, L. High Resolution 3D Exchange NMR Spectroscopy and the Mapping of Connectivities between Half-Integer Quadrupolar Nuclei. *Journal of the American Chemical Society* **2002**, *124* (33), 9708–9709. https://doi.org/10.1021/ja020534v.
(141) Edén, M.; Frydman, L. Homonuclear NMR Correlations between Half-Integer Quadrupolar Nuclei Undergoing Magic-Angle Spinning. *The Journal of Physical Chemistry B* **2003**, *107* (51), 14598–14611. https://doi.org/10.1021/jp035794t.
(142) Ding, S. W.; Mcdowell, C. A. Theoretical Calculations of the CPMAS Spectral Lineshapes of Half-Integer Quadrupole Systems. *Journal of Magnetic Resonance, Series A* **1995**, *114* (1), 80–87. https://doi.org/10.1006/jmra.1995.1108.
(143) Dowell, N. G.; Ashbrook, S. E.; Wimperis, S. Relative Orientation of Quadrupole Tensors from High-Resolution NMR of Powdered Solids. *The Journal of Physical Chemistry A* **2002**, *106* (41), 9470–9478. https://doi.org/10.1021/jp021315z.
(144) Nijman, M.; Ernst, M.; Kentgens, A. P.; Meier, B. H. Rotational-Resonance NMR Experiments in Half-Integer Quadrupolar Spin Systems. *Molecular Physics* **2000**, *98* (3), 161–178. https://doi.org/10.1080/00268970009483280.
(145) Ajithkumar, T. G.; Kentgens, A. P. M. Homonuclear Correlation Experiments of Half-Integer Quadrupolar Nuclei Using Multiple-Quantum Techniques Spinning at a P(4) Magic Angle. *Journal of the American Chemical Society* **2003**, *125* (9), 2398–2399. https://doi.org/10.1021/ja0292647.
(146) Ajithkumar, T. G.; van Eck, E. R. H.; Kentgens, a P. M. Homonuclear Correlation Experiments for Quadrupolar Nuclei, Spinning Away from the Magic Angle. *Solid state nuclear magnetic resonance* **2004**, *26* (3–4), 180–186. https://doi.org/10.1016/j.ssnmr.2004.03.005.
(147) Baldus, M.; Rovnyak, D.; Griffin, R. G. Radio-Frequency-Mediated Dipolar Recoupling among Half-Integer Quadrupolar Spins. *The Journal of Chemical Physics* **2000**, *112* (13), 5902. https://doi.org/10.1063/1.481187.
(148) Painter, A. J.; Duer, M. J. Double-Quantum-Filtered Nuclear Magnetic Resonance Spectroscopy Applied to Quadrupolar Nuclei in Solids. *The Journal of Chemical Physics* **2002**, *116* (2), 710. https://doi.org/10.1063/1.1425831.
(149) Mali, G.; Fink, G.; Taulelle, F. Double-Quantum Homonuclear Correlation Magic Angle Sample Spinning Nuclear Magnetic Resonance Spectroscopy of Dipolar-Coupled Quadrupolar Nuclei. *The Journal of chemical physics* **2004**, *120* (6), 2835–2845. https://doi.org/10.1063/1.1638741.
(150) Edén, M.; Annersten, H.; Zazzi, \AAsa. Pulse-Assisted Homonuclear Dipolar Recoupling of Half-Integer Quadrupolar Spins in Magic-Angle Spinning NMR. *Chemical Physics Letters* **2005**, *410* (1–3), 24–30. https://doi.org/10.1016/j.cplett.2005.04.030.
(151) Edén, M.; Zhou, D.; Yu, J. Improved Double-Quantum NMR Correlation Spectroscopy of Dipolar-Coupled Quadrupolar Spins. *Chemical Physics Letters* **2006**, *431* (4–6), 397–403. https://doi.org/10.1016/j.cplett.2006.09.081.
(152) Wang, Q.; Hu, B.; Lafon, O.; Trébosc, J.; Deng, F.; Amoureux, J. P. Double-Quantum Homonuclear NMR Correlation Spectroscopy of Quadrupolar Nuclei Subjected to Magic-Angle Spinning and High Magnetic Field. *Journal of magnetic resonance* **2009**, *200* (2), 251–260. https://doi.org/10.1016/j.jmr.2009.07.009.
(153) Yu, Y.; Keil, P.; Stevensson, B.; Hansen, M. R.; Edén, M. Assessment of New Symmetry-Based Dipolar Recoupling Schemes for Homonuclear Magnetization Exchange between Quadrupolar Nuclei in Two-Dimensional Correlation MAS NMR. *Journal of Magnetic Resonance* **2020**, *316*, 106734. https://doi.org/10.1016/j.jmr.2020.106734.

(154) Yu, Y.; Keil, P.; Hansen, M. R.; Edén, M. Improved Magnetization Transfers among Quadrupolar Nuclei in Two-Dimensional Homonuclear Correlation NMR Experiments Applied to Inorganic Network Structures. *Molecules* **2020**, *25* (2), 337. https://doi.org/10.3390/molecules25020337.
(155) Duong, N. T.; Lee, D.; Mentink-Vigier, F.; Lafon, O.; De Paëpe, G. On the Use of Radio-Frequency Offsets for Improving Double-Quantum Homonuclear Dipolar Recoupling of Half-Integer-Spin Quadrupolar Nuclei. *Magnetic Resonance in Chemistry* **2021**, *59* (9–10), 991–1008. https://doi.org/10.1002/mrc.5142.
(156) Pandey, M. K.; Amoureux, J.-P.; Asakura, T.; Nishiyama, Y. Sensitivity Enhanced $^{14}N/^{14}N$ Correlations to Probe Inter-Beta-Sheet Interactions Using Fast Magic Angle Spinning Solid-State NMR in Biological Solids. *Phys. Chem. Chem. Phys.* **2016**, *18* (32), 22583–22589. https://doi.org/10.1039/C6CP03848D.
(157) Yu, Z.; Zheng, A.; Wang, Q.; Chen, L.; Xu, J.; Amoureux, J.-P.; Deng, F. Insights into the Dealumination of Zeolite HY Revealed by Sensitivity-Enhanced ^{27}Al DQ-MAS NMR Spectroscopy at High Field. *Angewandte Chemie International Edition* **2010**, *49* (46), 8657–8661. https://doi.org/10.1002/anie.201004007.
(158) Fyfe, C. A.; Wong-Moon, K. C.; Huang, Y.; Grondey, H. INEPT Experiments in Solid-State NMR. *J. Am. Chem. Soc.* **1995**, *117* (41), 10397–10398. https://doi.org/10.1021/ja00146a031.
(159) Coelho, C.; Azaïs, T.; Bonhomme-Coury, L.; Laurent, G.; Bonhomme, C. Efficiency of the Refocused $^{31}P–^{29}Si$ MAS-*J*-INEPT NMR Experiment for the Characterization of Silicophosphate Crystalline Phases and Amorphous Gels. *Inorg. Chem.* **2007**, *46* (4), 1379–1387. https://doi.org/10.1021/ic061964f.
(160) Massiot, D.; Fayon, F.; Alonso, B.; Trebosc, J.; Amoureux, J.-P. Chemical Bonding Differences Evidenced from J-Coupling in Solid State NMR Experiments Involving Quadrupolar Nuclei. *Journal of Magnetic Resonance* **2003**, *164* (1), 160–164. https://doi.org/10.1016/S1090-7807(03)00134-4.
(161) Coelho, C.; Azais, T.; Bonhomme-Coury, L.; Maquet, J.; Massiot, D.; Bonhomme, C. Application of the MAS-J-HMQC Experiment to a New Pair of Nuclei $\{^{29}Si,^{31}P\}$: $Si_5O(PO_4)_6$ and SiP_2O_7 Polymorphs. *Journal of Magnetic Resonance* **2006**, *179* (1), 114–119. https://doi.org/10.1016/j.jmr.2005.11.015.
(162) Alonso, B.; Massiot, D. Multi-Scale NMR Characterisation of Mesostructured Materials Using $^{1}H\rightarrow^{13}C$ through-Bond Polarisation Transfer, Fast MAS, and ^{1}H Spin Diffusion. *Journal of Magnetic Resonance* **2003**, *163* (2), 347–352. https://doi.org/10.1016/S1090-7807(03)00061-2.
(163) Elena, B.; Lesage, A.; Steuernagel, S.; Böckmann, A.; Emsley, L. Proton to Carbon-13 INEPT in Solid-State NMR Spectroscopy. *Journal of the American Chemical Society* **2005**, *127* (49), 17296–17302. https://doi.org/10.1021/ja054411x.
(164) Mao, K.; Wiench, J. W.; Lin, V. S.-Y.; Pruski, M. Indirectly Detected Through-Bond Chemical Shift Correlation NMR Spectroscopy in Solids under Fast MAS: Studies of Organic–Inorganic Hybrid Materials. *Journal of Magnetic Resonance* **2009**, *196* (1), 92–95. https://doi.org/10.1016/j.jmr.2008.10.010.
(165) Martineau, C.; Fayon, F.; Legein, C.; Buzaré, J.-Y.; Body, M.; Massiot, D.; Goutenoire, F. Structure Determination of β-Pb_2ZnF_6 by Coupling Multinuclear Solid State NMR, Powder XRD and Ab Initio Calculations. *Dalton transactions (Cambridge, England : 2003)* **2008**, No. 44, 6150–6158. https://doi.org/10.1039/b810863c.
(166) Yu, J.; Hu, L.; Shen, Y.; Ren, J. Phase Change of $NaYF_4$:Er Crystals in Oxyfluoride Phosphate Upconversion Luminescent Glass Ceramics: An Advanced Solid-State NMR Study. *Inorg. Chem.* **2021**, *60* (8), 5868–5881. https://doi.org/10.1021/acs.inorgchem.1c00283.
(167) Chen, Y.; Dorn, R. W.; Hanrahan, M. P.; Wei, L.; Blome-Fernández, R.; Medina-Gonzalez, A. M.; Adamson, M. A. S.; Flintgruber, A. H.; Vela, J.; Rossini, A. J. Revealing the Surface Structure of CdSe Nanocrystals by Dynamic Nuclear Polarization-Enhanced ^{77}Se and ^{113}Cd Solid-State NMR

Spectroscopy. *J. Am. Chem. Soc.* **2021**, *143* (23), 8747–8760. https://doi.org/10.1021/jacs.1c03162.
(168) Pourpoint, F.; Venel, F.; Giovine, R.; Trébosc, J.; Vancompernolle, T.; Taoufik, M.; Sarou-Kanian, V.; Gauvin, R. M.; Lafon, O. Probing ^{29}Si-^{17}O Connectivities and Proximities by Solid-State NMR. *Journal of Magnetic Resonance* **2021**, *330*, 107029. https://doi.org/10.1016/j.jmr.2021.107029.
(169) Larsen, F. H.; Jakobsen, H. J.; Ellis, P. D.; Nielsen, N. Chr. Sensitivity-Enhanced Quadrupolar-Echo NMR of Half-Integer Quadrupolar Nuclei. Magnitudes and Relative Orientation of Chemical Shielding and Quadrupolar Coupling Tensors. *The Journal of Physical Chemistry A* **1997**, *101* (46), 8597–8606.
(170) Nagashima, H.; Trébosc, J.; Calvez, L.; Pourpoint, F.; Mear, F.; Lafon, O.; Amoureux, J.-P. ^{71}Ga-^{77}Se Connectivities and Proximities in Gallium Selenide Crystal and Glass Probed by Solid-State NMR. *Journal of Magnetic Resonance* **2017**, *282*, 71–82. https://doi.org/10.1016/j.jmr.2017.07.009.
(171) Wang, Q.; Trébosc, J.; Li, Y.; Xu, J.; Hu, B.; Feng, N.; Chen, Q.; Lafon, O.; Amoureux, J.-P.; Deng, F. Signal Enhancement of J-HMQC Experiments in Solid-State NMR Involving Half-Integer Quadrupolar Nuclei. *Chem. Commun.* **2013**, *49* (59), 6653–6655. https://doi.org/10.1039/c3cc42961j.
(172) Wang, Q.; Li, Y.; Trébosc, J.; Lafon, O.; Xu, J.; Hu, B.; Feng, N.; Chen, Q.; Amoureux, J.-P.; Deng, F. Population Transfer HMQC for Half-Integer Quadrupolar Nuclei. *The Journal of Chemical Physics* **2015**, *142* (9), 094201. https://doi.org/10.1063/1.4913683.
(173) van Wüllen, L.; Koller, H.; Kalwei, M. Modern Solid State Double Resonance NMR Strategies for the Structural Characterization of Adsorbate Complexes Involved in the MTG Process. *Physical Chemistry Chemical Physics* **2002**, *4* (9), 1665–1674. https://doi.org/10.1039/b108999b.
(174) Pourpoint, F.; Morin, Y.; Gauvin, R. M.; Trébosc, J.; Capet, F.; Lafon, O.; Amoureux, J.-P. Advances in Structural Studies on Alkylaluminum Species in the Solid State via Challenging ^{27}Al–^{13}C NMR Spectroscopy and X-Ray Diffraction. *J. Phys. Chem. C* **2013**, *117* (35), 18091–18099. https://doi.org/10.1021/jp4055044.
(175) Mazoyer, E.; Trébosc, J.; Baudouin, A.; Boyron, O.; Pelletier, J.; Basset, J.-M.; Vitorino, M. J.; Nicholas, C. P.; Gauvin, R. M.; Taoufik, M.; Delevoye, L. Heteronuclear NMR Correlations To Probe the Local Structure of Catalytically Active Surface Aluminum Hydride Species on γ-Alumina. *Angewandte Chemie International Edition* **2010**, *49* (51), 9854–9858. https://doi.org/10.1002/anie.201004310.
(176) Zhang, X.; Hu, L.; Ren, J. Structural Studies of Rare Earth-Doped Fluoroborosilicate Glasses by Advanced Solid-State NMR. *J. Phys. Chem. C* **2020**, *124* (16), 8919–8929. https://doi.org/10.1021/acs.jpcc.0c00290.
(177) Vasconcelos, F.; Cristol, S.; Paul, J.-F.; Tricot, G.; Amoureux, J.-P.; Montagne, L.; Mauri, F.; Delevoye, L. ^{17}O Solid-State NMR and First-Principles Calculations of Sodium Trimetaphosphate ($Na_3P_3O_9$), Tripolyphosphate ($Na_5P_3O_{10}$), and Pyrophosphate ($Na_4P_2O_7$). *Inorganic chemistry* **2008**, *47* (16), 7327–7337. https://doi.org/10.1021/ic800637p.
(178) Garaga, M. N.; Hsieh, M.-F.; Nour, Z.; Deschamps, M.; Massiot, D.; Chmelka, B. F.; Cadars, S. Local Environments of Boron Heteroatoms in Non-Crystalline Layered Borosilicates. *Phys. Chem. Chem. Phys.* **2015**, *17* (33), 21664–21682. https://doi.org/10.1039/C5CP03448E.
(179) Morizet, Y.; Vuilleumier, R.; Paris, M. A NMR and Molecular Dynamics Study of CO_2-Bearing Basaltic Melts and Glasses. *Chemical Geology* **2015**, *418*, 89–103. https://doi.org/10.1016/j.chemgeo.2015.03.021.
(180) Tricot, G.; Raguenet, B.; Silly, G.; Ribes, M.; Pradel, A.; Eckert, H. P–O–B^3 Linkages in Borophosphate Glasses Evidenced by High Field ^{11}B/^{31}P Correlation NMR. *Chem. Commun.* **2015**, *51* (45), 9284–9286. https://doi.org/10.1039/C5CC01992C.

(181) Tricot, G.; Mentré, O.; Cristol, S.; Delevoye, L. Fine Hierarchy of the V–O Bonds by Advanced Solid State NMR: Novel $Pb_4(VO_2)(PO_4)_3$ Structure as a Textbook Case. *Inorg. Chem.* **2012**, *51* (24), 13108–13113. https://doi.org/10.1021/ic300966r.
(182) Montouillout, V.; Morais, C. M.; Douy, A.; Fayon, F.; Massiot, D. Toward a Better Description of Gallo-Phosphate Materials in Solid-State NMR: 1D and 2D Correlation Studies. *Magnetic Resonance in Chemistry* **2006**, *44* (8), 770–775. https://doi.org/10.1002/mrc.1846.
(183) Jerschow, A. From Nuclear Structure to the Quadrupolar NMR Interaction and High-Resolution Spectroscopy. *Progress in Nuclear Magnetic Resonance Spectroscopy* **2005**, *46* (1), 63–78. https://doi.org/10.1016/j.pnmrs.2004.12.001.
(184) Fernandez, C.; Pruski, M. Probing Quadrupolar Nuclei by Solid-State NMR Spectroscopy : Recent Advances. *Topics in current chemistry* **2012**, *306* (June 2011), 119–188. https://doi.org/10.1007/128.
(185) Frydman, L.; Harwood, J. S. Isotropic Spectra of Half-Integer Quadrupolar Spins from Bidimensional Magic-Angle Spinning NMR. *J. Am. Chem. Soc.* **1995**, *117* (19), 5367–5368. https://doi.org/10.1021/ja00124a023.
(186) Amoureux, J.-P.; Pruski, M. MQMAS NMR: Experimental Strategies and Applications. In *Encyclopedia of Magnetic Resonance*; Harris, R. K., Wasylishen, R. E., Eds.; John Wiley & Sons, Ltd, 2008. https://doi.org/10.1002/9780470034590.emrstm0319.pub2.
(187) Wiench, J. W.; Tricot, G.; Delevoye, L.; Trebosc, J.; Frye, J.; Montagne, L.; Amoureux, J.-P.; Pruski, M. SPAM-MQ-HETCOR: An Improved Method for Heteronuclear Correlation Spectroscopy between Quadrupolar and Spin-1/2 Nuclei in Solid-State NMR. *Phys. Chem. Chem. Phys.* **2006**, *8* (1), 144–150. https://doi.org/10.1039/B512246E.
(188) Morais, C. M.; Montouillout, V.; Deschamps, M.; Iuga, D.; Fayon, F.; Paz, F. A. A.; Rocha, J.; Fernandez, C.; Massiot, D. 1D to 3D NMR Study of Microporous Alumino-Phosphate AlPO(4)-40. *Magnetic resonance in chemistry* **2009**, *47* (11), 942–947. https://doi.org/10.1002/mrc.2492.
(189) Kwak, H.-T.; Srinivasan, P.; Quine, J.; Massiot, D.; Gan, Z. Satellite Transition Rotational Resonance of Homonuclear Quadrupolar Spins: Magic-Angle Effect on Spin-Echo Decay and Inversion Recovery. *Chemical Physics Letters* **2003**, *376* (1–2), 75–82. https://doi.org/10.1016/S0009-2614(03)00958-8.
(190) Stejskal, E.; Schaefer, J.; Waugh, J. S. Magic-Angle Spinning and Polarization Transfer in Proton-Enhanced NMR. *J. Magn. Reson.* **1977**, *28*, 105–112.
(191) Meier, B. H. Cross Polarization under Fast Magic Angle Spinning: Thermodynamical Considerations. *Chemical Physics Letters* **1992**, *188* (3–4), 201–207. https://doi.org/10.1016/0009-2614(92)90009-C.
(192) Wu, X. L.; Zilm, K. W. Cross Polarization with High-Speed Magic-Angle Spinning. *Journal of Magnetic Resonance, Series A* **1993**, *104* (2), 154–165. https://doi.org/10.1006/jmra.1993.1203.
(193) Trébosc, J.; Wiench, J. W.; Huh, S.; Lin, V. S.-Y.; Pruski, M. Studies of Organically Functionalized Mesoporous Silicas Using Heteronuclear Solid-State Correlation NMR Spectroscopy under Fast Magic Angle Spinning. *Journal of the American Chemical Society* **2005**, *127* (20), 7587–7593. https://doi.org/10.1021/ja0509127.
(194) Janicke, M. T.; Landry, C. C.; Christiansen, S. C.; Kumar, D.; Stucky, G. D.; Chmelka, B. F. Aluminum Incorporation and Interfacial Structures in MCM-41 Mesoporous Molecular Sieves. *J. Am. Chem. Soc.* **1998**, *120* (28), 6940–6951. https://doi.org/10.1021/ja972633s.
(195) Avenier, P.; Lesage, A.; Taoufik, M.; Baudouin, A.; De Mallmann, A.; Fiddy, S.; Vautier, M.; Veyre, L.; Basset, J.-M.; Emsley, L.; Quadrelli, E. A. Well-Defined Surface Imido Amido Tantalum(V) Species from Ammonia and Silica-Supported Tantalum Hydrides. *J. Am. Chem. Soc.* **2007**, *129* (1), 176–186. https://doi.org/10.1021/ja0666809.
(196) Keenan, C. D.; Herling, M. M.; Siegel, R.; Petzold, N.; Bowers, C. R.; Rössler, E. A.; Breu, J.; Senker, J. Porosity of Pillared Clays Studied by Hyperpolarized ^{129}Xe NMR Spectroscopy and Xe Adsorption Isotherms. *Langmuir* **2013**, *29* (2), 643–652. https://doi.org/10.1021/la304502r.

(197) Santos, R. A.; Wind, R. A.; Bronnimann, C. E. ^{1}H CRAMPS and ^{1}H-^{31}P HetCor Experiments on Bone, Bone Mineral, and Model Calcium Phosphate Phases. *Journal of Magnetic Resonance, Series B* **1994**, *105* (2), 183–187. https://doi.org/10.1006/jmrb.1994.1120.
(198) Wenslow, R. M.; Mueller, K. T. Structural Details of Aqueous Attack on a Phosphate Glass by ^{1}H/^{31}P Cross-Polarization NMR. *J. Phys. Chem. B* **1998**, *102* (45), 9033–9038. https://doi.org/10.1021/jp9824252.
(199) Blanc, F.; Sperrin, L.; Lee, D.; Dervisoglu, R.; Yamazaki, Y.; Haile, S. M.; De Paëpe, G.; Grey, C. P. Dynamic Nuclear Polarization NMR of Low-γ Nuclei: Structural Insights into Hydrated Yttrium-Doped $BaZrO_3$. *J. Phys. Chem. Lett.* **2014**, *5*, 2431–2436.
(200) Wang, Z.; Hanrahan, M. P.; Kobayashi, T.; Perras, F. A.; Chen, Y.; Engelke, F.; Reiter, C.; Purea, A.; Rossini, A. J.; Pruski, M. Combining Fast Magic Angle Spinning Dynamic Nuclear Polarization with Indirect Detection to Further Enhance the Sensitivity of Solid-State NMR Spectroscopy. *Solid State Nuclear Magnetic Resonance* **2020**, *109*, 101685. https://doi.org/10.1016/j.ssnmr.2020.101685.
(201) Protesescu, L.; Rossini, A. J.; Kriegner, D.; Valla, M.; de Kergommeaux, A.; Walter, M.; Kravchyk, K. V.; Nachtegaal, M.; Stangl, J.; Malaman, B.; Reiss, P.; Lesage, A.; Emsley, L.; Copéret, C.; Kovalenko, M. V. Unraveling the Core-Shell Structure of Ligand-Capped Sn/SnO_x Nanoparticles by Surface-Enhanced Nuclear Magnetic Resonance, Mössbauer, and X-Ray Absorption Spectroscopies. *ACS nano* **2014**, *8* (3), 2639–2648. https://doi.org/10.1021/nn406344n.
(202) Mao, K.; Kobayashi, T.; Wiench, J. W.; Chen, H.-T.; Tsai, C.-H.; Lin, V. S.-Y.; Pruski, M. Conformations of Silica-Bound (Pentafluorophenyl)Propyl Groups Determined by Solid-State NMR Spectroscopy and Theoretical Calculations. *J. Am. Chem. Soc.* **2010**, *132* (35), 12452–12457. https://doi.org/10.1021/ja105007b.
(203) Taulelle, F.; Pruski, M.; Amoureux, J. P.; Lang, D.; Bailly, A.; Huguenard, C.; Haouas, M.; Gérardin, C.; Loiseau, T.; Férey, G. Isomerization of the Prenucleation Building Unit during Crystallization of $AlPO_4$-CJ2: An MQMAS, CP-MQMAS, and HETCOR NMR Study. *J. Am. Chem. Soc.* **1999**, *121* (51), 12148–12153. https://doi.org/10.1021/ja991295n.
(204) Ziarelli, F.; Casciola, M.; Pica, M.; Donnadio, A.; Aussenac, F.; Sauvée, C.; Capitani, D.; Viel, S. Dynamic Nuclear Polarisation NMR of Nanosized Zirconium Phosphate Polymer Fillers. *Chem. Commun.* **2014**, 10137–10139. https://doi.org/10.1039/C4CC02723J.
(205) Lejeune, C.; Coelho, C.; Bonhomme-Coury, L.; Azaïs, T.; Maquet, J.; Bonhomme, C. Studies of Silicophosphate Derivatives by ^{31}P→^{29}Si CP MAS NMR. *Solid State Nuclear Magnetic Resonance* **2005**, *27* (4), 242–246. https://doi.org/10.1016/j.ssnmr.2005.02.001.
(206) van Rossum, B.-J.; De Groot, C. P.; Ladizhansky, V.; Vega, S.; De Groot, H. J. M. A Method for Measuring Heteronuclear (^{1}H-^{13}C) Distances in High Speed MAS NMR. *J. Am. Chem. Soc.* **2000**, *122* (10), 3465–3472.
(207) Ladizhansky, V.; Vega, S. Polarization Transfer Dynamics in Lee–Goldburg Cross Polarization Nuclear Magnetic Resonance Experiments on Rotating Solids. *J. Chem. Phys.* **2000**, *112* (16), 7158–7168. https://doi.org/10.1063/1.481281.
(208) Lin, K. S. K.; Tseng, Y.-H.; Mou, Y.; Hsu, Y.-C.; Yang, C.-M.; Chan, J. C. C. Mechanistic Study of Apatite Formation on Bioactive Glass Surface Using 31P Solid-State NMR Spectroscopy. *Chem. Mater.* **2005**, *17* (17), 4493–4501. https://doi.org/10.1021/cm050654c.
(209) Mafra, L.; Rocha, J.; Fernandez, C.; Almeida Paz, F. A. Characterization of Microporous Aluminophosphate IST-1 Using ^{1}H Lee-Goldburg Techniques. *Journal of magnetic resonance* **2006**, *180* (2), 236–244. https://doi.org/10.1016/j.jmr.2006.02.017.
(210) Hing, A. H.; Vega, S.; Schaefer, J. Transferred-Echo Double-Resonance NMR. *Journal of Magnetic Resonance* **1992**, *209*, 205–209.
(211) Gullion, T.; Schaefer, J. Rotational-Echo Double-Resonance NMR. *J. Magn. Reson.* **1989**, *81* (2), 196–200. https://doi.org/10.1016/j.jmr.2011.09.003.

(212) Hologne, M.; Bertani, P.; Bonhomme, C. $^{1}H/^{31}P$ Distance Determination by Solid-State NMR in Multiple-Spin Systems. *Solid State Nucl. Magn. Reson.* **2005**, *28* (1), 50–56. https://doi.org/10.1016/j.ssnmr.2005.04.003.
(213) van Rossum, B.-J.; Förster, H.; de Groot, H. J. M. High-Field and High-Speed CP-MAS ^{13}C NMR Heteronuclear Dipolar-Correlation Spectroscopy of Solids with Frequency-Switched Lee–Goldburg Homonuclear Decoupling. *Journal of Magnetic Resonance* **1997**, *124* (2), 516–519. https://doi.org/10.1006/jmre.1996.1089.
(214) Ishii, Y.; Yesinowski, J. P.; Tycko, R. Sensitivity Enhancement in Solid-State ^{13}C NMR of Synthetic Polymers and Biopolymers by ^{1}H NMR Detection with High-Speed Magic Angle Spinning. *Journal of the American Chemical Society* **2001**, *123* (12), 2921–2922.
(215) Wiench, J. W.; Bronnimann, C. E.; Lin, V. S.-Y.; Pruski, M. Chemical Shift Correlation NMR Spectroscopy with Indirect Detection in Fast Rotating Solids: Studies of Organically Functionalized Mesoporous Silicas. *J. Am. Chem. Soc.* **2007**, *129* (40), 12076–12077. https://doi.org/10.1021/ja074746+.
(216) Althaus, S. M.; Mao, K.; Stringer, J. A.; Kobayashi, T.; Pruski, M. Indirectly Detected Heteronuclear Correlation Solid-State NMR Spectroscopy of Naturally Abundant ^{15}N Nuclei. *Solid State Nuclear Magnetic Resonance* **2014**, *57–58*, 17–21. https://doi.org/10.1016/j.ssnmr.2013.11.001.
(217) Venkatesh, A.; Ryan, M. J.; Biswas, A.; Boteju, K. C.; Sadow, A. D.; Rossini, A. J. Enhancing the Sensitivity of Solid-State NMR Experiments with Very Low Gyromagnetic Ratio Nuclei with Fast Magic Angle Spinning and Proton Detection. *J. Phys. Chem. A* **2018**, *122* (25), 5635–5643. https://doi.org/10.1021/acs.jpca.8b05107.
(218) Malär, A. A.; Sun, Q.; Zehnder, J.; Kehr, G.; Erker, G.; Wiegand, T. Proton-Phosphorous Connectivities Revealed by High-Resolution Proton-Detected Solid-State NMR. *Phys. Chem. Chem. Phys.* **2022**, *24* (13), 7768–7778. https://doi.org/10.1039/D2CP00616B.
(219) Venkatesh, A.; Hung, I.; Boteju, K. C.; Sadow, A. D.; Gor'kov, P. L.; Gan, Z.; Rossini, A. J. Suppressing ^{1}H Spin Diffusion in Fast MAS Proton Detected Heteronuclear Correlation Solid-State NMR Experiments. *Solid State Nuclear Magnetic Resonance* **2020**, *105*, 101636. https://doi.org/10.1016/j.ssnmr.2019.101636.
(220) Brinkmann, A.; Kentgens, A. P. M. Proton-Selective ^{17}O-^{1}H Distance Measurements in Fast Magic-Angle-Spinning Solid-State NMR Spectroscopy for the Determination of Hydrogen Bond Lengths. *J. Am. Chem. Soc.* **2006**, *128*, 14758–14759.
(221) Lucier, B. E. G.; Johnston, K. E.; Xu, W.; Hanson, J. C.; Senanayake, S. D.; Yao, S.; Bourassa, M. W.; Srebro, M.; Autschbach, J.; Schurko, R. W. Unravelling the Structure of Magnus ' Pink Salt. *J. Am. Chem. Soc.* **2014**, *136*, 1333–1351.
(222) Paluch, P.; Rankin, A. G. M.; Trébosc, J.; Lafon, O.; Amoureux, J.-P. Analysis of HMQC Experiments Applied to a Spin ½ Nucleus Subject to Very Large CSA. *Solid State Nuclear Magnetic Resonance* **2019**, *100*, 11–25. https://doi.org/10.1016/j.ssnmr.2019.03.001.
(223) Perras, F. A.; Venkatesh, A.; Hanrahan, M. P.; Goh, T. W.; Huang, W.; Rossini, A. J.; Pruski, M. Indirect Detection of Infinite-Speed MAS Solid-State NMR Spectra. *Journal of Magnetic Resonance* **2017**, *276*, 95–102. https://doi.org/10.1016/j.jmr.2017.01.010.
(224) Piveteau, L.; Ong, T.-C.; Rossini, A. J.; Emsley, L.; Copéret, C.; Kovalenko, M. V. Structure of Colloidal Quantum Dots from Dynamic Nuclear Polarization Surface Enhanced NMR Spectroscopy. *J. Am. Chem. Soc.* **2015**, *137* (43), 13964–13971. https://doi.org/10.1021/jacs.5b09248.
(225) Venkatesh, A.; Luan, X.; Perras, F. A.; Hung, I.; Huang, W.; Rossini, A. J. T_1-Noise Eliminated Dipolar Heteronuclear Multiple-Quantum Coherence Solid-State NMR Spectroscopy. *Phys. Chem. Chem. Phys.* **2020**, *22* (36), 20815–20828. https://doi.org/10.1039/D0CP03511D.
(226) Kervern, G.; Pintacuda, G.; Emsley, L. Fast Adiabatic Pulses for Solid-State NMR of Paramagnetic Systems. *Chemical Physics Letters* **2007**, *435* (1–3), 157–162. https://doi.org/10.1016/j.cplett.2006.12.056.

(227) Venkatesh, A.; Lund, A.; Rochlitz, L.; Jabbour, R.; Gordon, C. P.; Menzildjian, G.; Viger-Gravel, J.; Berruyer, P.; Gajan, D.; Copéret, C.; Lesage, A.; Rossini, A. J. The Structure of Molecular and Surface Platinum Sites Determined by DNP-SENS and Fast MAS 195Pt Solid-State NMR Spectroscopy. *J. Am. Chem. Soc.* **2020**, *142* (44), 18936–18945. https://doi.org/10.1021/jacs.0c09101.

(228) Venkatesh, A.; Perras, F. A.; Rossini, A. J. Proton-Detected Solid-State NMR Spectroscopy of Spin-1/2 Nuclei with Large Chemical Shift Anisotropy. *Journal of Magnetic Resonance* **2021**, *327*, 106983. https://doi.org/10.1016/j.jmr.2021.106983.

(229) Bayzou, R.; Trébosc, J.; Hung, I.; Gan, Z.; Lafon, O.; Amoureux, J.-P. Indirect NMR Detection via Proton of Nuclei Subject to Large Anisotropic Interactions, Such as ^{14}N, ^{195}Pt, and ^{35}Cl, Using the T-HMQC Sequence. *J. Chem. Phys.* **2022**, *156* (6), 064202. https://doi.org/10.1063/5.0082700.

(230) Qi, G.; Wang, Q.; Xu, J.; Wu, Q.; Wang, C.; Zhao, X.; Meng, X.; Xiao, F.; Deng, F. Direct Observation of Tin Sites and Their Reversible Interconversion in Zeolites by Solid-State NMR Spectroscopy. *Commun Chem* **2018**, *1* (1), 1–7. https://doi.org/10.1038/s42004-018-0023-1.

(231) Vega, A. J. CP/MAS of Quadrupolar S = 3/2 Nuclei. *Solid state nuclear magnetic resonance* **1992**, *1* (1), 17–32.

(232) Amoureux, J.-P.; Pruski, M. Theoretical and Experimental Assessment of Single-and Multiple-Quantum Cross-Polarization in Solid State NMR. *Molecular Physics* **2002**, *100*, 1595–1613. https://doi.org/10.1080/00268970210125755.

(233) Barrie, P. J. Distorted Powder Lineshapes in ^{27}Al CP / MAS NMR Spectroscopy of Solids. *Chemical Physics Letters* **1993**, *208* (5), 486–490. https://doi.org/10.1016/0009-2614(93)87177-5.

(234) Hayashi, S.; Hayamizu, K. Line Shapes in CP/MAS NMR Spectra of Half-Integer Quadrupolar Nuclei. *Chemical Physics Letters* **1993**, *203* (4), 319–324. https://doi.org/10.1016/0009-2614(93)85575-9.

(235) Ashbrook, S. E.; Wimperis, S. Spin-Locking of Half-Integer Quadrupolar Nuclei in Nuclear Magnetic Resonance of Solids: Second-Order Quadrupolar and Resonance Offset Effects. *The Journal of Chemical Physics* **2009**, *131* (19), 194509. https://doi.org/10.1063/1.3263904.

(236) Tricot, G.; Lafon, O.; Trébosc, J.; Delevoye, L.; Méar, F.; Montagne, L.; Amoureux, J.-P. Structural Characterisation of Phosphate Materials: New Insights into the Spatial Proximities between Phosphorus and Quadrupolar Nuclei Using the D-HMQC MAS NMR Technique. *Phys. Chem. Chem. Phys.* **2011**, *13* (37), 16786–16794. https://doi.org/10.1039/C1CP20993K.

(237) Trebosc, J.; Hu, B.; Amoureux, J. P.; Gan, Z. Through-Space R^3-HETCOR Experiments between Spin-1/2 and Half-Integer Quadrupolar Nuclei in Solid-State NMR. *Journal of Magnetic Resonance* **2007**, *186* (2), 220–227. https://doi.org/10.1016/j.jmr.2007.02.015.

(238) Martineau, C.; Bouchevreau, B.; Taulelle, F.; Trébosc, J.; Lafon, O.; Paul Amoureux, J. High-Resolution through-Space Correlations between Spin-1/2 and Half-Integer Quadrupolar Nuclei Using the MQ-D-R-INEPT NMR Experiment. *Physical Chemistry Chemical Physics* **2012**, *14*, 7112–7119. https://doi.org/10.1039/c2cp40344g.

(239) Venkatesh, A.; Hanrahan, M. P.; Rossini, A. J. Proton Detection of MAS Solid-State NMR Spectra of Half-Integer Quadrupolar Nuclei. *Solid State Nuclear Magnetic Resonance* **2017**, *84*, 171–181. https://doi.org/10.1016/j.ssnmr.2017.03.005.

(240) Perras, F. A.; Kobayashi, T.; Pruski, M. Natural Abundance ^{17}O DNP Two-Dimensional and Surface-Enhanced NMR Spectroscopy. *J. Am. Chem. Soc.* **2015**, *137* (26), 8336–8339. https://doi.org/10.1021/jacs.5b03905.

(241) Perras, F. A.; Kobayashi, T.; Pruski, M. PRESTO Polarization Transfer to Quadrupolar Nuclei: Implications for Dynamic Nuclear Polarization. *Phys. Chem. Chem. Phys.* **2015**, *17* (35), 22616–22622. https://doi.org/10.1039/C5CP04145G.

(242) Zhao, X.; Hoffbauer, W.; Schmedt auf der Günne, J.; Levitt, M. H. Heteronuclear Polarization Transfer by Symmetry-Based Recoupling Sequences in Solid-State NMR. *Solid state nuclear magnetic resonance* **2004**, *26* (2), 57–64. https://doi.org/10.1016/j.ssnmr.2003.11.001.

(243) Sardo, M.; Siegel, R.; Santos, S. M.; Rocha, J.; Gomes, J. R. B.; Mafra, L. Combining Multinuclear High-Resolution Solid-State MAS NMR and Computational Methods for Resonance Assignment of Glutathione Tripeptide. *J. Phys. Chem. A* **2012**, *116* (25), 6711–6719. https://doi.org/10.1021/jp302128r.

(244) Giovine, R.; Trébosc, J.; Pourpoint, F.; Lafon, O.; Amoureux, J.-P. Magnetization Transfer from Protons to Quadrupolar Nuclei in Solid-State NMR Using PRESTO or Dipolar-Mediated Refocused INEPT Methods. *J. Magn. Reson.* **2019**, *299*, 109–123. https://doi.org/10.1016/j.jmr.2018.12.016.

(245) Gómez, J. S.; Rankin, A. G. M.; Trébosc, J.; Pourpoint, F.; Tsutsumi, Y.; Nagashima, H.; Lafon, O.; Amoureux, J.-P. Improved NMR Transfer of Magnetization from Protons to Half-Integer Spin Quadrupolar Nuclei at Moderate and High Magic-Angle Spinning Frequencies. *Magnetic Resonance* **2021**, *2* (1), 447–464. https://doi.org/10.5194/mr-2-447-2021.

(246) Nagashima, H.; Trébosc, J.; Kon, Y.; Sato, K.; Lafon, O.; Amoureux, J.-P. Observation of Low-γ Quadrupolar Nuclei by Surface-Enhanced NMR Spectroscopy. *J. Am. Chem. Soc.* **2020**, *142* (24), 10659–10672. https://doi.org/10.1021/jacs.9b13838.

(247) Nagashima, H.; Trébosc, J.; Kon, Y.; Lafon, O.; Amoureux, J.-P. Efficient Transfer of DNP-Enhanced ^{1}H Magnetization to Half-Integer Quadrupolar Nuclei in Solids at Moderate Spinning Rate. *Magnetic Resonance in Chemistry* **2021**, *59* (9–10), 920–939. https://doi.org/10.1002/mrc.5121.

(248) Perras, F. A.; Chaudhary, U.; Slowing, I. I.; Pruski, M. Probing Surface Hydrogen Bonding and Dynamics by Natural Abundance, Multidimensional, ^{17}O DNP-NMR Spectroscopy. *J. Phys. Chem. C* **2016**, *120* (21), 11535–11544. https://doi.org/10.1021/acs.jpcc.6b02579.

(249) Peng, L.; Huo, H.; Liu, Y.; Grey, C. P. ^{17}O Magic Angle Spinning NMR Studies of Brønsted Acid Sites in Zeolites HY and HZSM-5. *J. Am. Chem. Soc.* **2007**, *129* (2), 335–346. https://doi.org/10.1021/ja064922z.

(250) Lee, D.; Leroy, C.; Crevant, C.; Bonhomme-Coury, L.; Babonneau, F.; Laurencin, D.; Bonhomme, C.; Paëpe, G. D. Interfacial Ca^{2+} Environments in Nanocrystalline Apatites Revealed by Dynamic Nuclear Polarization Enhanced ^{43}Ca NMR Spectroscopy. *Nature Communications* **2017**, *8*, 14104. https://doi.org/10.1038/ncomms14104.

(251) Hwang, S.-J.; Chen, C.-Y.; Zones, S. I. Boron Sites in Borosilicate Zeolites at Various Stages of Hydration Studied by Solid State NMR Spectroscopy. *J. Phys. Chem. B* **2004**, *108* (48), 18535–18546. https://doi.org/10.1021/jp0476904.

(252) van Wüllen, L.; Schwering, G. ^{11}B-MQMAS and ^{29}Si–{^{11}B} Double-Resonance NMR Studies on the Structure of Binary B_2O_3–SiO_2 Glasses. *Solid State Nuclear Magnetic Resonance* **2002**, *21* (3), 134–144. https://doi.org/10.1006/snmr.2002.0054.

(253) Zeyer-Düsterer, M.; Montagne, L.; Palavit, G.; Jäger, C. Combined ^{17}O NMR and ^{11}B–^{31}P Double Resonance NMR Studies of Sodium Borophosphate Glasses. *Solid State Nuclear Magnetic Resonance* **2005**, *27* (1), 50–64. https://doi.org/10.1016/j.ssnmr.2004.06.009.

(254) Hung, I.; Gan, Z.; Gor'kov, P. L.; Kaseman, D. C.; Sen, S.; LaComb, M.; Stebbins, J. F. Detection of "Free" Oxide Ions in Low-Silica Ca/Mg Silicate Glasses: Results from ^{17}O→^{29}Si HETCOR NMR. *Journal of Non-Crystalline Solids* **2016**, *445–446*, 1–6. https://doi.org/10.1016/j.jnoncrysol.2016.04.042.

(255) Fyfe, C. A.; Wong-Moon, K. C.; Huang, Y.; Grondey, H.; Mueller, K. T. Dipolar-Based ^{27}Al-^{29}Si Solid-State NMR Connectivity Experiments in Zeolite Molecular Sieve Frameworks. *J. Phys. Chem.* **1995**, *99* (21), 8707–8716. https://doi.org/10.1021/j100021a041.

(256) Egan, J. M.; Wenslow, R. M.; Mueller, K. T. Mapping Aluminum/Phosphorus Connectivities in Aluminophosphate Glasses. *Journal of Non-Crystalline Solids* **2000**, *261* (1–3), 115–126. https://doi.org/10.1016/S0022-3093(99)00606-7.

(257) Edén, M.; Grins, J.; Shen, Z.; Weng, Z. Fast ^{29}Si Magic-Angle-Spinning NMR Acquisitions by RAPT-CP ^{27}Al→^{29}Si Polarization Transfer. *Journal of Magnetic Resonance* **2004**, *169* (2), 279–283. https://doi.org/10.1016/j.jmr.2004.05.009.

(258) van der Wel, P. C. A.; Hu, K.-N.; Lewandowski, J.; Griffin, R. G. Dynamic Nuclear Polarization of Amyloidogenic Peptide Nanocrystals: GNNQQNY, a Core Segment of the Yeast Prion Protein Sup35p. *Journal of the American Chemical Society* **2006**, *128* (33), 10840–10846. https://doi.org/10.1021/ja0626685.
(259) Lafon, O.; Lilly Thankamony, A. S.; Kobayashi, T.; Carnevale, D.; Vitzthum, V.; Slowing, I. I.; Kandel, K.; Vezin, H.; Amoureux, J.-P.; Bodenhausen, G.; Pruski, M. Mesoporous Silica Nanoparticles Loaded with Surfactant: Low Temperature Magic Angle Spinning ^{13}C and ^{29}Si NMR Enhanced by Dynamic Nuclear Polarization. *J. Phys. Chem. C* **2013**, *117* (3), 1375–1382. https://doi.org/10.1021/jp310109s.
(260) Rossini, A. J.; Emsley, L.; O'Dell, L. A. Dynamic Nuclear Polarisation Enhanced ^{14}N Overtone MAS NMR Spectroscopy. *Phys. Chem. Chem. Phys.* **2014**, *16* (25), 12890–12899. https://doi.org/10.1039/C4CP00590B.
(261) Haies, I.; Jarvis, J. A.; Bentley, H.; Kuprov, I.; Williamson, P. T. F.; Carravetta, M. ^{14}N Overtone NMR under MAS: Signal Enhancement Using Symmetry-Based Sequences and Novel Simulation Strategies. *Phys. Chem. Chem. Phys.* **2015**, *17*, 6577–6587. https://doi.org/10.1039/C4CP03994G.
(262) Cavadini, S.; Antonijevic, S.; Lupulescu, A.; Bodenhausen, G. Indirect Detection of Nitrogen-14 in Solids via Protons by Nuclear Magnetic Resonance Spectroscopy. *Journal of magnetic resonance (San Diego, Calif. : 1997)* **2006**, *182* (1), 168–172. https://doi.org/10.1016/j.jmr.2006.06.003.
(263) Cavadini, S.; Abraham, A.; Bodenhausen, G. Proton-Detected Nitrogen-14 NMR by Recoupling of Heteronuclear Dipolar Interactions Using Symmetry-Based Sequences. *Chemical Physics Letters* **2007**, *445* (1–3), 1–5. https://doi.org/10.1016/j.cplett.2007.07.060.
(264) Shen, M.; Trébosc, J.; Lafon, O.; Gan, Z.; Pourpoint, F.; Hu, B.; Chen, Q.; Amoureux, J.-P. Solid-State NMR Indirect Detection of Nuclei Experiencing Large Anisotropic Interactions Using Spinning Sideband-Selective Pulses. *Solid State Nuclear Magnetic Resonance* **2015**, *72*, 104–117. https://doi.org/10.1016/j.ssnmr.2015.09.003.
(265) Shen, M.; Trébosc, J.; O'Dell, L. A.; Lafon, O.; Pourpoint, F.; Hu, B.; Chen, Q.; Amoureux, J.-P. Comparison of Various NMR Methods for the Indirect Detection of Nitrogen-14 Nuclei via Protons in Solids. *Journal of Magnetic Resonance* **2015**, *258*, 86–95. https://doi.org/10.1016/j.jmr.2015.06.008.
(266) Rankin, A. G. M.; Trébosc, J.; Paluch, P.; Lafon, O.; Amoureux, J.-P. Evaluation of Excitation Schemes for Indirect Detection of ^{14}N via Solid-State HMQC NMR Experiments. *Journal of Magnetic Resonance* **2019**, *303*, 28–41. https://doi.org/10.1016/j.jmr.2019.04.004.
(267) Gan, Z.; Amoureux, J.-P.; Trébosc, J. Proton-Detected ^{14}N MAS NMR Using Homonuclear Decoupled Rotary Resonance. *Chemical Physics Letters* **2007**, *435* (1–3), 163–169. https://doi.org/10.1016/j.cplett.2006.12.066.
(268) Gan, Z. $^{13}C/^{14}N$ Heteronuclear Multiple-Quantum Correlation with Rotary Resonance and REDOR Dipolar Recoupling. *Journal of Magnetic Resonance* **2007**, *184* (1), 39–43. https://doi.org/10.1016/j.jmr.2006.09.016.
(269) Nishiyama, Y.; Endo, Y.; Nemoto, T.; Utsumi, H.; Yamauchi, K.; Hioka, K.; Asakura, T. Very Fast Magic Angle Spinning (1)H-(14)N 2D Solid-State NMR: Sub-Micro-Liter Sample Data Collection in a Few Minutes. *Journal of magnetic resonance (San Diego, Calif. : 1997)* **2011**, *208* (1), 44–48. https://doi.org/10.1016/j.jmr.2010.10.001.
(270) Cavadini, S.; Abraham, A.; Bodenhausen, G. Coherence Transfer between Spy Nuclei and Nitrogen-14 in Solids. *Journal of magnetic resonance (San Diego, Calif. : 1997)* **2008**, *190* (1), 160–164. https://doi.org/10.1016/j.jmr.2007.10.008.
(271) Wack, J.; Ahnfeldt, T.; Stock, N.; Senker, J. Identifying Selective Host − Guest Interactions Based on Hydrogen Bond Donor − Acceptor Pattern in Functionalized Al-MIL-53 Metal − Organic Frameworks. *J. Phys. Chem. C* **2013**, *117*, 11991–20001.
(272) Bouchevreau, B.; Martineau, C.; Mellot-Draznieks, C.; Tuel, A.; Suchomel, M. R.; Trébosc, J.; Lafon, O.; Amoureux, J.; Taulelle, F. High-Resolution Structural Characterization of Two

Layered Aluminophosphates by Synchrotron Powder Diffraction and NMR Crystallographies. *Chem. Mater.* **2013**, *25*, 2227–2242.
(273) Shen, M.; Trébosc, J.; Lafon, O.; Pourpoint, F.; Hu, B.; Chen, Q.; Amoureux, J.-P. Improving the Resolution in Proton-Detected through-Space Heteronuclear Multiple Quantum Correlation NMR Spectroscopy. *Journal of magnetic resonance (San Diego, Calif. : 1997)* **2014**, *245*, 38–49. https://doi.org/10.1016/j.jmr.2014.05.006.
(274) van Eck, E. R. H.; Janssen, R.; Maas, W. E. J. R.; Veeman, W. S. A Novel Application of Nuclear Spin-Echo Double-Resonance to Aluminophosphates and Aluminosilicates. *Chemical Physics Letters* **1990**, *174* (5), 428–432. https://doi.org/10.1016/S0009-2614(90)87174-P.
(275) Grey, C. P.; Vega, A. J. Determination of the Quadrupole Coupling Constant of the Invisible Aluminum Spins in Zeolite HY with ^{1}H-^{27}Al TRAPDOR NMR. *J. Am. Chem. Soc* **1995**, *117*, 8232–8242.
(276) Jarvis, J. A.; Haies, I. M.; Williamson, P. T. F.; Carravetta, M. An Efficient NMR Method for the Characterisation of ^{14}N Sites through Indirect ^{13}C Detection. *Physical chemistry chemical physics : PCCP* **2013**, *15* (20), 7613–7620. https://doi.org/10.1039/c3cp50787d.
(277) Jarvis, J. A.; Haies, I.; Lelli, M.; Rossini, A. J.; Kuprov, I.; Carravetta, M.; Williamson, P. T. F. Measurement of ^{14}N Quadrupole Couplings in Biomolecular Solids Using Indirect-Detection ^{14}N Solid-State NMR with DNP. *Chem. Commun.* **2017**, *53* (89), 12116–12119. https://doi.org/10.1039/C7CC03462H.
(278) Jarvis, J. A.; Concistre, M.; Haies, I. M.; Bounds, R. W.; Kuprov, I.; Carravetta, M.; Williamson, P. T. F. Quantitative Analysis of ^{14}N Quadrupolar Coupling Using ^{1}H Detected ^{14}N Solid-State NMR. *Phys. Chem. Chem. Phys.* **2019**, *21* (11), 5941–5949. https://doi.org/10.1039/C8CP06276E.
(279) Hung, I.; Gor'kov, P.; Gan, Z. Efficient and Sideband-Free ^{1}H-Detected ^{14}N Magic-Angle Spinning NMR. *J. Chem. Phys.* **2019**, *151* (15), 154202. https://doi.org/10.1063/1.5126599.
(280) Lu, X.; Lafon, O.; Trébosc, J.; Tricot, G.; Delevoye, L.; Méar, F.; Montagne, L.; Amoureux, J. P. Observation of Proximities between Spin-1/2 and Quadrupolar Nuclei: Which Heteronuclear Dipolar Recoupling Method Is Preferable? *The Journal of chemical physics* **2012**, *137* (14), 144201. https://doi.org/10.1063/1.4753987.
(281) Lafon, O.; Wang, Q.; Hu, B.; Vasconcelos, F.; Trébosc, J.; Cristol, S.; Deng, F.; Amoureux, J.-P. Indirect Detection via Spin-1/2 Nuclei in Solid State NMR Spectroscopy: Application to the Observation of Proximities between Protons and Quadrupolar Nuclei. *J. Phys. Chem. A* **2009**, *113* (46), 12864–12878. https://doi.org/10.1021/jp906099k.
(282) Fu, R.; Smith, S. A.; Bodenhausen, G. Recoupling of Heteronuclear Dipolar Interactions in Solid State Magic-Angle Spinning NMR by Simultaneous Frequency and Amplitude Modulation. *Chemical Physics Letters* **1997**, *272* (5), 361–369. https://doi.org/10.1016/S0009-2614(97)00537-X.
(283) Hu, B.; Trébosc, J.; Amoureux, J.-P. Comparison of Several Hetero-Nuclear Dipolar Recoupling NMR Methods to Be Used in MAS HMQC/HSQC. *Journal of magnetic resonance* **2008**, *192* (1), 112–122. https://doi.org/10.1016/j.jmr.2008.02.004.
(284) Nagashima, H.; Lilly Thankamony, A. S.; Trébosc, J.; Montagne, L.; Kerven, G.; Amoureux, J.-P.; Lafon, O. Observation of Proximities between Spin-1/2 and Quadrupolar Nuclei in Solids: Improved Robustness to Chemical Shielding Using Adiabatic Symmetry-Based Recoupling. *Solid State Nuclear Magnetic Resonance* **2018**, *94*, 7–19. https://doi.org/10.1016/j.ssnmr.2018.07.001.
(285) Belgamwar, R.; Rankin, A. G. M.; Maity, A.; Mishra, A. K.; Gómez, J. S.; Trébosc, J.; Vinod, C. P.; Lafon, O.; Polshettiwar, V. Boron Nitride and Oxide Supported on Dendritic Fibrous Nanosilica for Catalytic Oxidative Dehydrogenation of Propane. *ACS Sustainable Chem. Eng.* **2020**, *8* (43), 16124–16135. https://doi.org/10.1021/acssuschemeng.0c04148.
(286) Hung, I.; Gan, Z. High-Resolution NMR of *S* = 3/2 Quadrupole Nuclei by Detection of Double-Quantum Satellite Transitions via Protons. *J. Phys. Chem. Lett.* **2020**, 4734–4740. https://doi.org/10.1021/acs.jpclett.0c01236.

(287) Wong, A.; Laurencin, D.; Dupree, R.; Smith, M. E. Two-Dimensional ^{43}Ca–^{1}H Correlation Solid-State NMR Spectroscopy. *Solid State Nuclear Magnetic Resonance* **2009**, *35* (1), 32–36. https://doi.org/10.1016/j.ssnmr.2008.11.002.

(288) Merle, N.; Trébosc, J.; Baudouin, A.; Rosal, I. D.; Maron, L.; Szeto, K.; Genelot, M.; Mortreux, A.; Taoufik, M.; Delevoye, L.; Gauvin, R. M. ^{17}O NMR Gives Unprecedented Insights into the Structure of Supported Catalysts and Their Interaction with the Silica Carrier. *J. Am. Chem. Soc.* **2012**, *134* (22), 9263–9275. https://doi.org/10.1021/ja301085m.

(289) Bignami, G. P. M.; Dawson, D. M.; Seymour, V. R.; Wheatley, P. S.; Morris, R. E.; Ashbrook, S. E. Synthesis, Isotopic Enrichment, and Solid-State NMR Characterization of Zeolites Derived from the Assembly, Disassembly, Organization, Reassembly Process. *J. Am. Chem. Soc.* **2017**, *139* (14), 5140–5148. https://doi.org/10.1021/jacs.7b00386.

(290) Martel, L.; Cadars, S.; Véron, E.; Massiot, D.; Deschamps, M. Effects of the Orientation of the ^{23}Na-^{29}Si Dipolar Vector on the Dipolar Mediated Heteronuclear Solid State NMR Correlation Spectrum of Crystalline Sodium Silicates. *Solid state nuclear magnetic resonance* **2012**, *46*, 1–10. https://doi.org/10.1016/j.ssnmr.2012.04.001.

(291) Kobayashi, T.; Pruski, M. Indirectly Detected DNP-Enhanced ^{17}O NMR Spectroscopy: Observation of Non-Protonated Near-Surface Oxygen at Naturally Abundant Silica and Silica-Alumina. *ChemPhysChem* **2021**, *22* (14), 1441–1445. https://doi.org/10.1002/cphc.202100290.

(292) Taoufik, M.; Szeto, K. C.; Merle, N.; Rosal, I. D.; Maron, L.; Trébosc, J.; Tricot, G.; Gauvin, R. M.; Delevoye, L. Heteronuclear NMR Spectroscopy as a Surface-Selective Technique: A Unique Look at the Hydroxyl Groups of γ-Alumina. *Chemistry – A European Journal* **2014**, *20* (14), 4038–4046. https://doi.org/10.1002/chem.201304883.

(293) Cadars, S.; Guégan, R.; Garaga, M. N.; Bourrat, X.; Le Forestier, L.; Fayon, F.; Huynh, T. V.; Allier, T.; Nour, Z.; Massiot, D. New Insights into the Molecular Structures, Compositions, and Cation Distributions in Synthetic and Natural Montmorillonite Clays. *Chem. Mater.* **2012**, *24* (22), 4376–4389. https://doi.org/10.1021/cm302549k.

(294) Mellier, C.; Fayon, F.; Schnitzler, V.; Deniard, P.; Allix, M.; Quillard, S.; Massiot, D.; Bouler, J.-M.; Bujoli, B.; Janvier, P. Characterization and Properties of Novel Gallium-Doped Calcium Phosphate Ceramics. *Inorg. Chem.* **2011**, *50* (17), 8252–8260. https://doi.org/10.1021/ic2007777.

(295) Fernandez, C.; Morais, C.; Rocha, J.; Pruski, M. High-Resolution Heteronuclear Correlation Spectra between ^{31}P and ^{27}Al in Microporous Aluminophosphates. *Solid State Nuclear Magnetic Resonance* **2002**, *21* (1), 61–70. https://doi.org/10.1006/snmr.2001.0049.

(296) Sasaki, A.; Trébosc, J.; Amoureux, J.-P. A Comparison of Through-Space Population Transfers from Half-Integer Spin Quadrupolar Nuclei to ^{1}H Using MQ-HETCOR and MQ-SPAM-HETCOR under Fast MAS. *Journal of Magnetic Resonance* **2021**, *329*, 107028. https://doi.org/10.1016/j.jmr.2021.107028.

(297) Siegel, R.; Rocha, J.; Mafra, L. Combining STMAS and CRAMPS NMR Spectroscopy: High-Resolution HETCOR NMR Spectra of Quadrupolar and 1H Nuclei in Solids. *Chemical Physics Letters* **2009**, *470* (4–6), 337–341. https://doi.org/10.1016/j.cplett.2009.01.053.

(298) Sasaki, A.; Trébosc, J.; Amoureux, J.-P. Accelerating the Acquisition of High-Resolution Quadrupolar MQ/ST-HETCOR 2D Spectra under Fast MAS via ^{1}H Detection and through-Space Population Transfers. *Journal of Magnetic Resonance* **2021**, *333*, 107093. https://doi.org/10.1016/j.jmr.2021.107093.

(299) Trébosc, J.; Lafon, O.; Hu, B.; Amoureux, J.-P. Indirect High-Resolution Detection for Quadrupolar Spin-3/2 Nuclei in Dipolar HMQC Solid-State NMR Experiments. *Chemical Physics Letters* **2010**, *496* (1–3), 201–207. https://doi.org/10.1016/j.cplett.2010.07.037.

(300) Chan, J. C. C.; Bertmer, M.; Eckert, H. Site Connectivities in Amorphous Materials Studied by Double-Resonance NMR of Quadrupolar Nuclei: High-Resolution ^{11}B ↔ ^{27}Al Spectroscopy of Aluminoborate Glasses. *J. Am. Chem. Soc.* **1999**, *121* (22), 5238–5248. https://doi.org/10.1021/ja983385i.

(301) Lu, X.; Lilly Thankamony, A. S.; Trébosc, J.; Lafon, O.; Amoureux, J.-P. Probing Proximities between Different Quadrupolar Isotopes Using Multi-Pulse Cross-Polarization. *Journal of magnetic resonance (San Diego, Calif. : 1997)* **2013**, *228*, 148–158. https://doi.org/10.1016/j.jmr.2012.12.005.
(302) Xin, S.; Wang, Q.; Xu, J.; Feng, N.; Li, W.; Deng, F. Heteronuclear Correlation Experiments of ^{23}Na-^{27}Al in Rotating Solids. *Solid State Nuclear Magnetic Resonance* **2017**, *84*, 103–110. https://doi.org/10.1016/j.ssnmr.2017.01.002.
(303) Zheng, M.; Xin, S.; Wang, Q.; Trébosc, J.; Xu, J.; Qi, G.; Feng, N.; Lafon, O.; Deng, F. Through-Space ^{11}B–^{27}Al Correlation: Influence of the Recoupling Channel. *Magnetic Resonance in Chemistry* **2021**, *59* (9–10), 1062–1076. https://doi.org/10.1002/mrc.5163.
(304) Mafra, L.; Klinowski, J. Molecular Sieves: Crystalline Systems. In *eMagRes*; John Wiley & Sons, Ltd, 2013. https://doi.org/10.1002/9780470034590.emrstm0315.
(305) Mafra, L.; Klinowski, J. Advanced Solid-State NMR Techniques for the Study of Molecular Sieves. In *eMagRes*; John Wiley & Sons, Ltd, 2015. https://doi.org/10.1002/9780470034590.emrstm1307.
(306) Ashbrook, S. E.; Dawson, D. M.; Seymour, V. R. Recent Developments in Solid-State NMR Spectroscopy of Crystalline Microporous Materials. *Phys. Chem. Chem. Phys.* **2014**, *16* (18), 8223–8242. https://doi.org/10.1039/C4CP00578C.
(307) Roux, M.; Marichal, C.; Paillaud, J.-L.; Fernandez, C.; Baerlocher, C.; Chézeau, J.-M. Structural Investigation by Multinuclear Solid State NMR and X-Ray Diffraction of As-Synthesized, Dehydrated, and Calcined AlPO4-SOD. *J. Phys. Chem. B* **2001**, *105* (38), 9083–9092. https://doi.org/10.1021/jp010723k.
(308) Martineau, C.; Bouchevreau, B.; Tian, Z.; Lohmeier, S.-J.; Behrens, P.; Taulelle, F. Beyond the Limits of X-Ray Powder Diffraction: Description of the Nonperiodic Subnetworks in Aluminophosphate-Cloverite by NMR Crystallography. *Chemistry of Materials* **2011**, *23* (21), 4799–4809. https://doi.org/10.1021/cm2021033.
(309) Martineau, C.; Bouchevreau, B.; Siegel, R.; Senker, J.; Ristić, A.; Taulelle, F. Accurate Structural Description of the Two Nanoporous Fluorinated Aluminophosphates ULM-3(Al) and ULM-4(Al) by Solid-State NMR. *J. Phys. Chem. C* **2012**, *116* (40), 21489–21498. https://doi.org/10.1021/jp308056j.
(310) Amoureux, J.-P.; Trébosc, J.; Wiench, J. W.; Pruski, M. HMQC and Refocused-INEPT Experiments Involving Half-Integer Quadrupolar Nuclei in Solids. *Journal of magnetic resonance* **2007**, *184* (1), 1–14. https://doi.org/10.1016/j.jmr.2006.09.009.
(311) Ashbrook, S. E.; Cutajar, M.; Pickard, C. J.; Walton, R. I.; Wimperis, S. Structure and NMR Assignment in Calcined and As-Synthesized Forms of AlPO-14: A Combined Study by First-Principles Calculations and High-Resolution ^{27}Al-^{31}P MAS NMR Correlation. *Physical chemistry chemical physics : PCCP* **2008**, *10* (37), 5754–5764. https://doi.org/10.1039/b805681a.
(312) Castro, M.; Seymour, V. R.; Carnevale, D.; Griffin, J. M.; Ashbrook, S. E.; Wright, P. A.; Apperley, D. C.; Parker, J. E.; Thompson, S. P.; Fecant, A.; Bats, N. Molecular Modeling, Multinuclear NMR, and Diffraction Studies in the Templated Synthesis and Characterization of the Aluminophosphate Molecular Sieve STA-2. *J. Phys. Chem. C* **2010**, *114* (29), 12698–12710. https://doi.org/10.1021/jp104120y.
(313) Delevoye, L.; Fernandez, C.; Morais, C. M.; Amoureux, J.-P.; Montouillout, V.; Rocha, J. Double-Resonance Decoupling for Resolution Enhancement of ^{31}P Solid-State MAS and ^{27}Al → ^{31}P MQHETCOR NMR. *Solid state nuclear magnetic resonance* **2002**, *22* (4), 501–512. https://doi.org/10.1006/snmr.2002.0080.
(314) Afeworki, M.; Dorset, D. L.; Kennedy, G. J.; Strohmaier, K. G. Synthesis and Characterization of a New Microporous Material. 1. Structure of Aluminophosphate EMM-3. *Chem. Mater.* **2006**, *18* (6), 1697–1704. https://doi.org/10.1021/cm052174r.
(315) Bouchevreau, B.; Martineau, C.; Mellot-Draznieks, C.; Tuel, A.; Suchomel, M. R.; Trébosc, J.; Lafon, O.; Amoureux, J.-P.; Taulelle, F. An NMR-Driven Crystallography Strategy to Overcome the Computability Limit of Powder Structure Determination: A Layered Aluminophosphate

Case. *Chemistry – A European Journal* **2013**, *19* (16), 5009–5013. https://doi.org/10.1002/chem.201203767.
(316) Cadars, S.; Brouwer, D. H.; Chmelka, B. F. Probing Local Structures of Siliceous Zeolite Frameworks by Solid-State NMR and First-Principles Calculations of 29Si-O-29Si Scalar Couplings. *Physical chemistry chemical physics : PCCP* **2009**, *11* (11), 1825–1837. https://doi.org/10.1039/b815361b.
(317) Shayib, R. M.; George, N. C.; Seshadri, R.; Burton, A. W.; Zones, S. I.; Chmelka, B. F. Structure-Directing Roles and Interactions of Fluoride and Organocations with Siliceous Zeolite Frameworks. *Journal of the American Chemical Society* **2011**, *133* (46), 18728–18741. https://doi.org/10.1021/ja205164u.
(318) Brouwer, D. H.; Darton, R. J.; Morris, R. E.; Levitt, M. H. A Solid-State NMR Method for Solution of Zeolite Crystal Structures. *Journal of the American Chemical Society* **2005**, *127* (29), 10365–10370. https://doi.org/10.1021/ja052306h.
(319) Li, S.; Zheng, A.; Su, Y.; Zhang, H.; Chen, L.; Yang, J.; Ye, C.; Deng, F. Brønsted/Lewis Acid Synergy in Dealuminated HY Zeolite: A Combined Solid-State NMR and Theoretical Calculation Study. *Journal of the American Chemical Society* **2007**, *129* (36), 11161–11171. https://doi.org/10.1021/ja072767y.
(320) Li, S.; Huang, S.-J.; Shen, W.; Zhang, H.; Fang, H.; Zheng, A.; Liu, S.-B.; Deng, F. Probing the Spatial Proximities among Acid Sites in Dealuminated H-Y Zeolite by Solid-State NMR Spectroscopy. *J. Phys. Chem. C* **2008**, *112* (37), 14486–14494. https://doi.org/10.1021/jp803494n.
(321) Dib, E.; Grand, J.; Mintova, S.; Fernandez, C. Structure-Directing Agent Governs the Location of Silanol Defects in Zeolites. *Chem. Mater.* **2015**, *27* (22), 7577–7579. https://doi.org/10.1021/acs.chemmater.5b03668.
(322) Dib, E.; Grand, J.; Gedeon, A.; Mintova, S.; Fernandez, C. Control the Position of Framework Defects in Zeolites by Changing the Symmetry of Organic Structure Directing Agents. *Microporous and Mesoporous Materials* **2021**, *315*, 110899. https://doi.org/10.1016/j.micromeso.2021.110899.
(323) Schroeder, C.; Mück-Lichtenfeld, C.; Xu, L.; Grosso-Giordano, N. A.; Okrut, A.; Chen, C.-Y.; Zones, S. I.; Katz, A.; Hansen, M. R.; Koller, H. A Stable Silanol Triad in the Zeolite Catalyst SSZ-70. *Angewandte Chemie International Edition* **2020**, *59* (27), 10939–10943. https://doi.org/10.1002/anie.202001364.
(324) Chowdhury, A. D.; Paioni, A. L.; Houben, K.; Whiting, G. T.; Baldus, M.; Weckhuysen, B. M. Bridging the Gap between the Direct and Hydrocarbon Pool Mechanisms of the Methanol-to-Hydrocarbons Process. *Angewandte Chemie International Edition* **2018**, *57* (27), 8095–8099. https://doi.org/10.1002/anie.201803279.
(325) Chowdhury, A. D.; Lucini Paioni, A.; Whiting, G. T.; Fu, D.; Baldus, M.; Weckhuysen, B. M. Unraveling the Homologation Reaction Sequence of the Zeolite-Catalyzed Ethanol-to-Hydrocarbons Process. *Angewandte Chemie* **2019**, *131* (12), 3948–3952. https://doi.org/10.1002/ange.201814268.
(326) Wang, C.; Hu, M.; Chu, Y.; Zhou, X.; Wang, Q.; Qi, G.; Li, S.; Xu, J.; Deng, F. π-Interactions between Cyclic Carbocations and Aromatics Cause Zeolite Deactivation in Methanol-to-Hydrocarbon Conversion. *Angewandte Chemie International Edition* **2020**, *59* (18), 7198–7202. https://doi.org/10.1002/anie.202000637.
(327) Wang, C.; Chu, Y.; Hu, M.; Cai, W.; Wang, Q.; Qi, G.; Li, S.; Xu, J.; Deng, F. Insight into Carbocation-Induced Noncovalent Interactions in the Methanol-to-Olefins Reaction over ZSM-5 Zeolite by Solid-State NMR Spectroscopy. *Angewandte Chemie International Edition* **2021**, *60* (51), 26847–26854. https://doi.org/10.1002/anie.202112948.
(328) Wang, C.; Chu, Y.; Hu, M.; Cai, W.; Wang, Q.; Li, S.; Xu, J.; Deng, F. Influence of Zeolite Confinement Effects on Cation-π Interactions in Methanol-to-Hydrocarbons Conversion. *Chem. Commun.* **2022**. https://doi.org/10.1039/D2CC02216H.

(329) Li, S.; Pourpoint, F.; Trébosc, J.; Zhou, L.; Lafon, O.; Shen, M.; Zheng, A.; Wang, Q.; Amoureux, J.-P.; Deng, F. Host-Guest Interactions in Dealuminated HY Zeolite Probed by ^{13}C-^{27}Al Solid-State NMR Spectroscopy. *J. Phys. Chem. Lett.* **2014**, *5*, 3068–3072.
(330) Kennedy, G. J.; Wiench, J. W.; Pruski, M. Determination of ^{27}Al-^{29}Si Connectivities in Zeolites with 2D $^{27}Al \rightarrow ^{29}Si$ RAPT-CPMG-HETCOR NMR. *Solid state nuclear magnetic resonance* **2008**, *33* (4), 76–81. https://doi.org/10.1016/j.ssnmr.2008.04.002.
(331) Berkson, Z. J.; Hsieh, M.-F.; Smeets, S.; Gajan, D.; Lund, A.; Lesage, A.; Xie, D.; Zones, S. I.; McCusker, L. B.; Baerlocher, C.; Chmelka, B. F. Preferential Siting of Aluminum Heteroatoms in the Zeolite Catalyst Al-SSZ-70. *Angewandte Chemie International Edition* **2019**, *58* (19), 6255–6259. https://doi.org/10.1002/anie.201813533.
(332) Dib, E.; Mineva, T.; Veron, E.; Sarou-Kanian, V.; Fayon, F.; Alonso, B. ZSM-5 Zeolite: Complete Al Bond Connectivity and Implications on Structure Formation from Solid-State NMR and Quantum Chemistry Calculations. *J. Phys. Chem. Lett.* **2018**, *9* (1), 19–24. https://doi.org/10.1021/acs.jpclett.7b03050.
(333) Kumar, M.; Berkson, Z. J.; Clark, R. J.; Shen, Y.; Prisco, N. A.; Zheng, Q.; Zeng, Z.; Zheng, H.; McCusker, L. B.; Palmer, J. C.; Chmelka, B. F.; Rimer, J. D. Crystallization of Mordenite Platelets Using Cooperative Organic Structure-Directing Agents. *J. Am. Chem. Soc.* **2019**, *141* (51), 20155–20165. https://doi.org/10.1021/jacs.9b09697.
(334) Chen, K.; Gan, Z.; Horstmeier, S.; White, J. L. Distribution of Aluminum Species in Zeolite Catalysts: ^{27}Al NMR of Framework, Partially-Coordinated Framework, and Non-Framework Moieties. *J. Am. Chem. Soc.* **2021**, *143* (17), 6669–6680. https://doi.org/10.1021/jacs.1c02361.
(335) Lakiss, L.; Kouvatas, C.; Gilson, J.-P.; Valtchev, V.; Mintova, S.; Fernandez, C.; Bedard, R.; Abdo, S.; Bricker, J. Atomic-Insight into Zeolite Catalyst Forming—an Advanced NMR Study. *J. Phys. Chem. C* **2021**, *125* (36), 20028–20034. https://doi.org/10.1021/acs.jpcc.1c05501.
(336) Andreev, A. S.; Livadaris, V. Characterization of Catalytic Materials through a Facile Approach to Probe OH Groups by Solid-State NMR. *J. Phys. Chem. C* **2017**, *121* (26), 14108–14119. https://doi.org/10.1021/acs.jpcc.7b02283.
(337) Chen, K.; Horstmeier, S.; Nguyen, Vy. T.; Wang, B.; Crossley, S. P.; Pham, T.; Gan, Z.; Hung, I.; White, J. L. Structure and Catalytic Characterization of a Second Framework Al(IV) Site in Zeolite Catalysts Revealed by NMR at 35.2 T. *J. Am. Chem. Soc.* **2020**, *142* (16), 7514–7523. https://doi.org/10.1021/jacs.0c00590.
(338) Xin, S.; Wang, Q.; Xu, J.; Chu, Y.; Wang, P.; Feng, N.; Qi, G.; Trébosc, J.; Lafon, O.; Fan, W.; Deng, F. The Acidic Nature of "NMR-Invisible" Tri-Coordinated Framework Aluminum Species in Zeolites. *Chem. Sci.* **2019**, *10* (43), 10159–10169. https://doi.org/10.1039/C9SC02634G.
(339) Altvater, N. R.; Dorn, R. W.; Cendejas, M. C.; McDermott, W. P.; Thomas, B.; Rossini, A. J.; Hermans, I. B-MWW Zeolite: The Case Against Single-Site Catalysis. *Angewandte Chemie International Edition* **2020**, *59* (16), 6546–6550. https://doi.org/10.1002/anie.201914696.
(340) Devautour-Vinot, S.; Martineau, C.; Diaby, S.; Ben-Yahia, M.; Miller, S.; Serre, C.; Horcajada, P.; Cunha, D.; Taulelle, F.; Maurin, G. Caffeine Confinement into a Series of Functionalized Porous Zirconium MOFs: A Joint Experimental/Modeling Exploration. *J. Phys. Chem. C* **2013**, *117* (22), 11694–11704. https://doi.org/10.1021/jp402916y.
(341) Xu, J.; Terskikh, V. V.; Chu, Y.; Zheng, A.; Huang, Y. Mapping Out Chemically Similar, Crystallographically Nonequivalent Hydrogen Sites in Metal–Organic Frameworks by 1H Solid-State NMR Spectroscopy. *Chem. Mater.* **2015**, *27* (9), 3306–3316. https://doi.org/10.1021/acs.chemmater.5b00360.
(342) Krajnc, A.; Kos, T.; Zabukovec Logar, N.; Mali, G. A Simple NMR-Based Method for Studying the Spatial Distribution of Linkers within Mixed-Linker Metal–Organic Frameworks. *Angewandte Chemie International Edition* **2015**, *54* (36), 10535–10538. https://doi.org/10.1002/anie.201504426.
(343) Tang, J.; Li, S.; Su, Y.; Chu, Y.; Xu, J.; Deng, F. Quantitative Analysis of Linker Composition and Spatial Arrangement of Multivariate Metal–Organic Framework UiO-66 through 1H Fast MAS

NMR. *J. Phys. Chem. C* **2020**, *124* (32), 17640–17647. https://doi.org/10.1021/acs.jpcc.0c04244.
(344) Xiao, Y.; Chu, Y.; Li, S.; Chen, F.; Gao, W.; Xu, J.; Deng, F. Host-Guest Interaction in Ethylene and Ethane Separation on Zeolitic Imidazolate Frameworks as Revealed by Solid-State NMR Spectroscopy. *Chemistry – A European Journal* **2021**, *27* (44), 11303–11308. https://doi.org/10.1002/chem.202101779.
(345) Tang, J.; Chu, Y.; Li, S.; Xu, J.; Xiong, W.; Wang, Q.; Deng, F. Breathing Effect via Solvent Inclusions on the Linker Rotational Dynamics of Functionalized MIL-53. *Chemistry – A European Journal* **2021**, *27* (59), 14711–14720. https://doi.org/10.1002/chem.202102419.
(346) Krajnc, A.; Bueken, B.; De Vos, D.; Mali, G. Improved Resolution and Simplification of the Spin-Diffusion-Based NMR Method for the Structural Analysis of Mixed-Linker MOFs. *Journal of Magnetic Resonance* **2017**, *279*, 22–28. https://doi.org/10.1016/j.jmr.2017.04.008.
(347) Li, J.; Li, S.; Zheng, A.; Liu, X.; Yu, N.; Deng, F. Solid-State NMR Studies of Host–Guest Interaction between UiO-67 and Light Alkane at Room Temperature. *J. Phys. Chem. C* **2017**, *121* (26), 14261–14268. https://doi.org/10.1021/acs.jpcc.7b04611.
(348) Xiao, Y.; Chu, Y.; Li, S.; Su, Y.; Tang, J.; Xu, J.; Deng, F. Primary Adsorption Sites of Light Alkanes in Multivariate UiO-66 at Room Temperature as Revealed by Solid-State NMR. *J. Phys. Chem. C* **2020**, *124* (6), 3738–3746. https://doi.org/10.1021/acs.jpcc.0c00184.
(349) Mao, V. Y.; Milner, P. J.; Lee, J.-H.; Forse, A. C.; Kim, E. J.; Siegelman, R. L.; McGuirk, C. M.; Zasada, L. B.; Neaton, J. B.; Reimer, J. A.; Long, J. R. Cooperative Carbon Dioxide Adsorption in Alcoholamine- and Alkoxyalkylamine-Functionalized Metal–Organic Frameworks. *Angewandte Chemie International Edition* **2020**, *59* (44), 19468–19477. https://doi.org/10.1002/anie.201915561.
(350) Forse, A. C.; Milner, P. J.; Lee, J.-H.; Redfearn, H. N.; Oktawiec, J.; Siegelman, R. L.; Martell, J. D.; Dinakar, B.; Zasada, L. B.; Gonzalez, M. I.; Neaton, J. B.; Long, J. R.; Reimer, J. A. Elucidating CO_2 Chemisorption in Diamine-Appended Metal–Organic Frameworks. *J. Am. Chem. Soc.* **2018**, *140* (51), 18016–18031. https://doi.org/10.1021/jacs.8b10203.
(351) Pourpoint, F.; Lilly Thankamony, A. S.; Volkringer, C.; Loiseau, T.; Trébosc, J.; Aussenac, F.; Carnevale, D.; Bodenhausen, G.; Vezin, H.; Lafon, O.; Amoureux, J.-P. Probing ^{27}Al– ^{13}C Proximities in Metal–Organic Frameworks Using Dynamic Nuclear Polarization Enhanced NMR Spectroscopy. *Chem. Commun.* **2014**, *50* (8), 933–935. https://doi.org/10.1039/C3CC47208F.
(352) Giovine Raynald; Volkringer Christophe; Ashbrook Sharon E.; Trébosc Julien; McKay David; Loiseau Thierry; Amoureux Jean-Paul; Lafon Olivier; Pourpoint Frédérique. Solid-State NMR Spectroscopy Proves the Presence of Penta-coordinated Sc Sites in MIL-100(Sc). *Chemistry – A European Journal* **2017**, *23* (40), 9525–9534. https://doi.org/10.1002/chem.201700584.
(353) Copéret, C.; Liao, W.-C.; Gordon, C. P.; Ong, T.-C. Active Sites in Supported Single-Site Catalysts: An NMR Perspective. *J. Am. Chem. Soc.* **2017**, *139* (31), 10588–10596. https://doi.org/10.1021/jacs.6b12981.
(354) Gutmann, T.; Groszewicz, P. B.; Buntkowsky, G. Chapter One - Solid-State NMR of Nanocrystals. In *Annual Reports on NMR Spectroscopy*; Webb, G. A., Ed.; Academic Press, 2019; Vol. 97, pp 1–82. https://doi.org/10.1016/bs.arnmr.2018.12.001.
(355) Gordon, C. P.; Lätsch, L.; Copéret, C. Nuclear Magnetic Resonance: A Spectroscopic Probe to Understand the Electronic Structure and Reactivity of Molecules and Materials. *J. Phys. Chem. Lett.* **2021**, *12* (8), 2072–2085. https://doi.org/10.1021/acs.jpclett.0c03520.
(356) Rossini, A. J.; Zagdoun, A.; Lelli, M.; Lesage, A.; Copéret, C.; Emsley, L. Dynamic Nuclear Polarization Surface Enhanced NMR Spectroscopy. *Acc. Chem. Res.* **2013**, *46* (9), 1942–1951. https://doi.org/10.1021/ar300322x.
(357) Rataboul, F.; Baudouin, A.; Thieuleux, C.; Veyre, L.; Copéret, C.; Thivolle-Cazat, J.; Basset, J.-M.; Lesage, A.; Emsley, L. Molecular Understanding of the Formation of Surface Zirconium Hydrides upon Thermal Treatment under Hydrogen of [(⁝SiO)Zr(CH2tBu)3] by Using Advanced Solid-State NMR Techniques. *J. Am. Chem. Soc.* **2004**, *126* (39), 12541–12550. https://doi.org/10.1021/ja038486h.

(358) Kobayashi, T.; Mao, K.; Wang, S.-G.; Lin, V. S.-Y.; Pruski, M. Molecular Ordering of Mixed Surfactants in Mesoporous Silicas: A Solid-State NMR Study. *Solid State Nuclear Magnetic Resonance* **2011**, *39* (3), 65–71. https://doi.org/10.1016/j.ssnmr.2011.02.001.

(359) Kobayashi, T.; Singappuli-Arachchige, D.; Slowing, I. I.; Pruski, M. Spatial Distribution of Organic Functional Groups Supported on Mesoporous Silica Nanoparticles (2): A Study by 1H Triple-Quantum Fast-MAS Solid-State NMR. *Phys. Chem. Chem. Phys.* **2018**, *20* (34), 22203–22209. https://doi.org/10.1039/C8CP04425B.

(360) Wang, Z.; Li, T.; Jiang, Y.; Lafon, O.; Liu, Z.; Trébosc, J.; Baiker, A.; Amoureux, J.-P.; Huang, J. Acidity Enhancement through Synergy of Penta- and Tetra-Coordinated Aluminum Species in Amorphous Silica Networks. *Nature Communications* **2020**, *11* (1), 225. https://doi.org/10.1038/s41467-019-13907-7.

(361) Wang, Q.; Li, W.; Hung, I.; Mentink-Vigier, F.; Wang, X.; Qi, G.; Wang, X.; Gan, Z.; Xu, J.; Deng, F. Mapping the Oxygen Structure of γ-Al_2O_3 by High-Field Solid-State NMR Spectroscopy. *Nat Commun* **2020**, *11* (1), 3620. https://doi.org/10.1038/s41467-020-17470-4.

(362) Saint-Arroman, R. P.; Chabanas, M.; Baudouin, A.; Copéret, C.; Basset, J.-M.; Lesage, A.; Emsley, L. Characterization of Surface Organometallic Complexes Using High Resolution 2D Solid-State NMR Spectroscopy. Application to the Full Characterization of a Silica Supported Metal Carbyne: ⁝SiO−Mo(⁝C−Bu-t)(CH_2−Bu-t)$_2$. *J. Am. Chem. Soc.* **2001**, *123* (16), 3820–3821. https://doi.org/10.1021/ja002259n.

(363) Chabanas, M.; Baudouin, A.; Copéret, C.; Basset, J.-M.; Lukens, W.; Lesage, A.; Hediger, S.; Emsley, L. Perhydrocarbyl Re^{VII} Complexes: Comparison of Molecular and Surface Complexes. *J. Am. Chem. Soc.* **2003**, *125* (2), 492–504. https://doi.org/10.1021/ja020136s.

(364) Berkson, Z. J.; Bernhardt, M.; Schlapansky, S. L.; Benedikter, M. J.; Buchmeiser, M. R.; Price, G. A.; Sunley, G. J.; Copéret, C. Olefin-Surface Interactions: A Key Activity Parameter in Silica-Supported Olefin Metathesis Catalysts. *JACS Au* **2022**, *2* (3), 777–786. https://doi.org/10.1021/jacsau.2c00052.

(365) Gao, J.; Dorn, R. W.; Laurent, G. P.; Perras, F. A.; Rossini, A. J.; Conley, M. P. A Heterogeneous Palladium Catalyst for the Polymerization of Olefins Prepared by Halide Abstraction Using Surface R_3Si^+ Species. *Angewandte Chemie International Edition* **2022**, *61* (20), e202117279. https://doi.org/10.1002/anie.202117279.

(366) Wang, Z.; Patnaik, S.; Eedugurala, N.; Manzano, J. S.; Slowing, I. I.; Kobayashi, T.; Sadow, A. D.; Pruski, M. Silica-Supported Organolanthanum Catalysts for C–O Bond Cleavage in Epoxides. *J. Am. Chem. Soc.* **2020**, *142* (6), 2935–2947. https://doi.org/10.1021/jacs.9b11606.

(367) Bouhoute, Y.; Grekov, D.; Szeto, K. C.; Merle, N.; De Mallmann, A.; Lefebvre, F.; Raffa, G.; Del Rosal, I.; Maron, L.; Gauvin, R. M.; Delevoye, L.; Taoufik, M. Accessing Realistic Models for the WO_3–SiO_2 Industrial Catalyst through the Design of Organometallic Precursors. *ACS Catal.* **2016**, *6* (1), 1–18. https://doi.org/10.1021/acscatal.5b01744.

(368) Wang, Z.; Jiang, Y.; Lafon, O.; Trébosc, J.; Kim, K. D.; Stampfl, C.; Baiker, A.; Amoureux, J.-P.; Huang, J. Brønsted Acid Sites Based on Penta-Coordinated Aluminum Species. *Nature Communications* **2016**, *7*, 13820. https://doi.org/10.1038/ncomms13820.

(369) Alessandro Gallo; Fong, A.; Szeto, K. C.; Rieb, J.; Delevoye, L.; Gauvin, R. M.; Taoufik, M.; Peters, B.; Scott, S. L. Ligand Exchange-Mediated Activation and Stabilization of a Re-Based Olefin Metathesis Catalyst by Chlorinated Alumina. *J. Am. Chem. Soc.* **2016**, *138* (39), 12935–12947. https://doi.org/10.1021/jacs.6b06953.

(370) Szeto, K. C.; Jones, Z. R.; Merle, N.; Rios, C.; Gallo, A.; Le Quemener, F.; Delevoye, L.; Gauvin, R. M.; Scott, S. L.; Taoufik, M. A Strong Support Effect in Selective Propane Dehydrogenation Catalyzed by Ga(*i*-Bu)$_3$ Grafted onto γ-Alumina and Silica. *ACS Catal.* **2018**, *8* (8), 7566–7577. https://doi.org/10.1021/acscatal.8b00936.

(371) Zhang, F.; Szeto, K. C.; Taoufik, M.; Delevoye, L.; Gauvin, R. M.; Scott, S. L. Enhanced Metathesis Activity and Stability of Methyltrioxorhenium on a Mostly Amorphous Alumina: Role of the Local Grafting Environment. *J. Am. Chem. Soc.* **2018**, *140* (42), 13854–13868. https://doi.org/10.1021/jacs.8b08630.

(372) Kaushik, M.; Leroy, C.; Chen, Z.; Gajan, D.; Willinger, E.; Müller, C. R.; Fayon, F.; Massiot, D.; Fedorov, A.; Copéret, C.; Lesage, A.; Florian, P. Atomic-Scale Structure and Its Impact on Chemical Properties of Aluminum Oxide Layers Prepared by Atomic Layer Deposition on Silica. *Chem. Mater.* **2021**, *33* (9), 3335–3348. https://doi.org/10.1021/acs.chemmater.1c00516.
(373) Wang, Z.; Chen, K.; Jiang, Y.; Trébosc, J.; Yang, W.; Amoureux, J.-P.; Hung, I.; Gan, Z.; Baiker, A.; Lafon, O.; Huang, J. Revealing Brønsted Acidic Bridging SiOHAl Groups on Amorphous Silica–Alumina by Ultrahigh Field Solid-State NMR. *J. Phys. Chem. Lett.* **2021**, *12* (47), 11563–11572. https://doi.org/10.1021/acs.jpclett.1c02975.
(374) Ong, T.-C.; Liao, W.-C.; Mougel, V.; Gajan, D.; Lesage, A.; Emsley, L.; Copéret, C. Atomistic Description of Reaction Intermediates for Supported Metathesis Catalysts Enabled by DNP SENS. *Angewandte Chemie International Edition* **2016**, *55* (15), 4743–4747. https://doi.org/10.1002/anie.201510821.
(375) Perras, F. A.; Wang, Z.; Kobayashi, T.; Baiker, A.; Huang, J.; Pruski, M. Shedding Light on the Atomic-Scale Structure of Amorphous Silica–Alumina and Its Brønsted Acid Sites. *Phys. Chem. Chem. Phys.* **2019**, *21* (35), 19529–19537. https://doi.org/10.1039/C9CP04099D.
(376) Phillips, B. L. Crystallography and NMR: Applications to Geochemistry. In *Encyclopedia of Magnetic Resonance*; eds-in-chief R. K. Harris and R. Wasylishen, 2009. https://doi.org/10.1002/9780470034590.emrstm1045.
(377) Ashbrook, S. E.; Dawson, D. M. NMR Spectroscopy of Minerals and Allied Materials. In *Nuclear Magnetic Resonance*; 2016; pp 1–52. https://doi.org/10.1039/9781782624103-00001.
(378) Griffin, J. M.; Ashbrook, S. E. Chapter Five - Solid-State NMR of High-Pressure Silicates in the Earth's Mantle. In *Annual Reports on NMR Spectroscopy*; Webb, G. A., Ed.; Academic Press, 2013; Vol. 79, pp 241–332. https://doi.org/10.1016/B978-0-12-408098-0.00005-7.
(379) Mueller, K. T.; Sanders, R. L.; Washton, N. M. Clay Minerals. *eMagRes* **2014**, *3*, 13–28. https://doi.org/10.1002/9780470034590.emrstm1332.
(380) Todros, S.; Todesco, M.; Bagno, A. Biomaterials and Their Biomedical Applications: From Replacement to Regeneration. *Processes* **2021**, *9* (11), 1949. https://doi.org/10.3390/pr9111949.
(381) Montoya, C.; Du, Y.; Gianforcaro, A. L.; Orrego, S.; Yang, M.; Lelkes, P. I. On the Road to Smart Biomaterials for Bone Research: Definitions, Concepts, Advances, and Outlook. *Bone Res* **2021**, *9* (1), 1–16. https://doi.org/10.1038/s41413-020-00131-z.
(382) Hench, L. L. Bioceramics. *Journal of the American Ceramic Society* **1998**, *81* (7), 1705–1728. https://doi.org/10.1111/j.1151-2916.1998.tb02540.x.
(383) Kolodziejski, W. Solid-State NMR Studies of Bone. In *New Techniques in Solid-State NMR*; Klinowski, J., Ed.; Topics in Current Chemistry; Springer: Berlin, Heidelberg, 2005; pp 235–270. https://doi.org/10.1007/b98652.
(384) Gervais, C.; Bonhomme, C.; Laurencin, D. Recent Directions in the Solid-State NMR Study of Synthetic and Natural Calcium Phosphates. *Solid State Nuclear Magnetic Resonance* **2020**, *107*, 101663. https://doi.org/10.1016/j.ssnmr.2020.101663.
(385) Xue, X.; Kanzaki, M.; Shatskiy, A. Dense Hydrous Magnesium Silicates, Phase D, and Superhydrous B: New Structural Constraints from One- and Two-Dimensional ^{29}Si and ^{1}H NMR. *American Mineralogist* **2008**, *93* (7), 1099–1111. https://doi.org/10.2138/am.2008.2751.
(386) Cadars, S.; Layrac, G.; Gérardin, C.; Deschamps, M.; Yates, J. R.; Tichit, D.; Massiot, D. Identification and Quantification of Defects in the Cation Ordering in Mg/Al Layered Double Hydroxides. *Chem. Mater.* **2011**, *23* (11), 2821–2831. https://doi.org/10.1021/cm200029q.
(387) Sideris, P. J.; Blanc, F.; Gan, Z.; Grey, C. P. Identification of Cation Clustering in Mg–Al Layered Double Hydroxides Using Multinuclear Solid State Nuclear Magnetic Resonance Spectroscopy. *Chem. Mater.* **2012**, *24* (13), 2449–2461. https://doi.org/10.1021/cm300386d.
(388) Griffin, J. M.; Berry, A. J.; Frost, D. J.; Wimperis, S.; Ashbrook, S. E. Water in the Earth's Mantle: A Solid-State NMR Study of Hydrous Wadsleyite. *Chem. Sci.* **2013**, *4* (4), 1523–1538. https://doi.org/10.1039/C3SC21892A.

(389) Yu, Y.; Stevensson, B.; Pujari-Palmer, M.; Guo, H.; Engqvist, H.; Edén, M. The Monetite Structure Probed by Advanced Solid-State NMR Experimentation at Fast Magic-Angle Spinning. *International Journal of Molecular Sciences* **2019**, *20* (24), 6356. https://doi.org/10.3390/ijms20246356.
(390) Sorte, E. G.; Rimsza, J. M.; Alam, T. M. Computational and Experimental ^{1}H-NMR Study of Hydrated Mg-Based Minerals. *Molecules* **2020**, *25* (4), 933. https://doi.org/10.3390/molecules25040933.
(391) Pourpoint, F.; Gervais, C.; Bonhomme-Coury, L.; Azaïs, T.; Coelho, C.; Mauri, F.; Alonso, B.; Babonneau, F.; Bonhomme, C. Calcium Phosphates and Hydroxyapatite: Solid-State NMR Experiments and First-Principles Calculations. *Applied Magnetic Resonance* **2007**, *32* (4), 435–457. https://doi.org/10.1007/s00723-007-0040-1.
(392) Pourpoint, F.; Kolassiba, A.; Gervais, C.; Azaïs, T.; Bonhomme-Coury, L.; Bonhomme, C.; Mauri, F. First Principles Calculations of NMR Parameters in Biocompatible Materials Science: The Case Study of Calcium Phosphates, β- and γ-$Ca(PO_3)_2$. Combination with MAS-J Experiments. *Chem. Mater.* **2007**, *19* (26), 6367–6369. https://doi.org/10.1021/cm7028432.
(393) Lin, X.; Ideta, K.; Miyawaki, J.; Nishiyama, Y.; Mochida, I.; Yoon, S.-H. High Magnetic Field Solid-State NMR Analyses by Combining MAS, MQ-MAS, Homo-Nuclear and Hetero-Nuclear Correlation Experiments. *Magnetic Resonance in Chemistry* **2012**, *50* (4), 289–294. https://doi.org/10.1002/mrc.3804.
(394) Leroy, C.; Aussenac, F.; Bonhomme-Coury, L.; Osaka, A.; Hayakawa, S.; Babonneau, F.; Coelho-Diogo, C.; Bonhomme, C. Hydroxyapatites: Key Structural Questions and Answers from Dynamic Nuclear Polarization. *Anal. Chem.* **2017**, *89* (19), 10201–10207. https://doi.org/10.1021/acs.analchem.7b01332.
(395) Edén, M. Two-Dimensional MAS NMR Correlation Protocols Involving Double-Quantum Filtering of Quadrupolar Spin-Pairs. *Journal of Magnetic Resonance* **2010**, *204* (1), 99–110. https://doi.org/10.1016/j.jmr.2010.02.007.
(396) Cho, G.; Wu, Y.; Ackerman, J. L. Detection of Hydroxyl Ions in Bone Mineral by Solid-State NMR Spectroscopy. *Science* **2003**, *300* (5622), 1123–1127. https://doi.org/10.1126/science.1078470.
(397) Kaflak-Hachulska, A.; Samoson, A.; Kolodziejski, W. ^{1}H MAS and ^{1}H → ^{31}P CP/MAS NMR Study of Human Bone Mineral. *Calcif Tissue Int* **2003**, *73* (5), 476–486. https://doi.org/10.1007/s00223-002-2111-5.
(398) Pourpoint, F.; Diogo, C. C.; Gervais, C.; Bonhomme, C.; Fayon, F.; Dalicieux, S. L.; Gennero, I.; Salles, J.-P.; Howes, A. P.; Dupree, R.; Hanna, J. V.; Smith, M. E.; Mauri, F.; Guerrero, G.; Mutin, P. H.; Laurencin, D. High-Resolution Solid State NMR Experiments for the Characterization of Calcium Phosphate Biomaterials and Biominerals. *Journal of Materials Research* **2011**, *26* (18), 2355–2368. https://doi.org/10.1557/jmr.2011.250.
(399) Von Euw, S.; Ajili, W.; Chan-Chang, T.-H.-C.; Delices, A.; Laurent, G.; Babonneau, F.; Nassif, N.; Azaïs, T. Amorphous Surface Layer versus Transient Amorphous Precursor Phase in Bone – A Case Study Investigated by Solid-State NMR Spectroscopy. *Acta Biomaterialia* **2017**, *59*, 351–360. https://doi.org/10.1016/j.actbio.2017.06.040.
(400) Wu, Y.-J.; Tsai, T. W. T.; Huang, S.-J.; Mou, Y.; Lin, C.-J.; Chan, J. C. C. Hydrogen Bond Formation between Citrate and Phosphate Ions in Spherulites of Fluorapatite. *Langmuir* **2013**, *29* (37), 11681–11686. https://doi.org/10.1021/la402392b.
(401) De Sa Peixoto, P.; Silva, J. V. C.; Laurent, G.; Schmutz, M.; Thomas, D.; Bouchoux, A.; Gésan-Guiziou, G. How High Concentrations of Proteins Stabilize the Amorphous State of Calcium Orthophosphate: A Solid-State Nuclear Magnetic Resonance (NMR) Study of the Casein Case. *Langmuir* **2017**, *33* (5), 1256–1264. https://doi.org/10.1021/acs.langmuir.6b04235.
(402) Von Euw, S.; Chan-Chang, T.-H.-C.; Paquis, C.; Haye, B.; Pehau-Arnaudet, G.; Babonneau, F.; Azaïs, T.; Nassif, N. Organization of Bone Mineral: The Role of Mineral–Water Interactions. *Geosciences* **2018**, *8* (12), 466. https://doi.org/10.3390/geosciences8120466.

(403) Mason, H. E.; Kozlowski, A.; Phillips, B. L. Solid-State NMR Study of the Role of H and Na in AB-Type Carbonate Hydroxylapatite. *Chem. Mater.* **2008**, *20* (1), 294–302. https://doi.org/10.1021/cm0716598.
(404) Gomes, S.; Renaudin, G.; Mesbah, A.; Jallot, E.; Bonhomme, C.; Babonneau, F.; Nedelec, J.-M. Thorough Analysis of Silicon Substitution in Biphasic Calcium Phosphate Bioceramics: A Multi-Technique Study. *Acta Biomaterialia* **2010**, *6* (8), 3264–3274. https://doi.org/10.1016/j.actbio.2010.02.034.
(405) Sozzani, P.; Bracco, S.; Comotti, A.; Mauri, M.; Simonutti, R.; Valsesia, P. Nanoporosity of an Organo-Clay Shown by Hyperpolarized Xenon and 2D NMR Spectroscopy. *Chem. Commun.* **2006**, No. 18, 1921–1923. https://doi.org/10.1039/B602040B.
(406) Bracco, S.; Valsesia, P.; Ferretti, L.; Sozzani, P.; Mauri, M.; Comotti, A. Spectroscopic Observations of Hybrid Interfaces and Gas Storage in Organo-Clays. *Microporous and Mesoporous Materials* **2008**, *107* (1), 102–107. https://doi.org/10.1016/j.micromeso.2007.05.013.
(407) Gougeon, R. D.; Reinholdt, M.; Delmotte, L.; Miehé-Brendlé, J.; Jeandet, P. Solid-State NMR Investigation on the Interactions between a Synthetic Montmorillonite and Two Homopolypeptides. *Solid state nuclear magnetic resonance* **2006**, *29* (4), 322–329. https://doi.org/10.1016/j.ssnmr.2005.10.016.
(408) Borsacchi, S.; Geppi, M.; Ricci, L.; Ruggeri, G.; Veracini, C. A. Interactions at the Surface of Organophilic-Modified Laponites: A Multinuclear Solid-State NMR Study. *Langmuir* **2007**, *23* (7), 3953–3960.
(409) Raya, J.; Hirschinger, J.; Ovarlez, S.; Giulieri, F.; Chaze, A.-M.; Delamare, F. Insertion of Indigo Molecules in the Sepiolite Structure as Evidenced by ^{1}H–^{29}Si Heteronuclear Correlation Spectroscopy. *Phys. Chem. Chem. Phys.* **2010**, *12* (43), 14508–14514. https://doi.org/10.1039/C0CP00834F.
(410) Phillips, B. L.; Mason, H. E.; Guggenheim, S. Hydrogen Bonded Silanols in the 10 Å Phase: Evidence from NMR Spectroscopy. *American Mineralogist* **2007**, *92* (8–9), 1474–1485. https://doi.org/10.2138/am.2007.2417.
(411) Nielsen, U. G.; Majzlan, J.; Phillips, B.; Ziliox, M.; Grey, C. P. Characterization of Defects and the Local Structure in Natural and Synthetic Alunite (K, Na, H_3O)$Al_3(SO_4)_2(OH)_6$ by Multi-Nuclear Solid-State NMR Spectroscopy. *American Mineralogist* **2007**, *92* (4), 587–597. https://doi.org/10.2138/am.2007.2414.
(412) Fechtelkord, M.; Behrens, H.; Holtz, F.; Fyfe, C. A.; Groat, L. A.; Raudsepp, M. Influence of F Content on the Composition of Al-Rich Synthetic Phlogopite: Part I. New Information on Structure and Phase-Formation from ^{29}Si, ^{1}H, and ^{19}F MAS NMR Spectroscopies. *American Mineralogist* **2003**, *88* (1), 47–53. https://doi.org/10.2138/am-2003-0106.
(413) Knight, C. T. G.; Kirkpatrick, R. J.; Oldfield, E. The Connectivity of Silicon Sites in Silicate Glasses, as Determined by Two-Dimensional ^{29}Si Nuclear Magnetic Resonance Spectroscopy. *Journal of Non-Crystalline Solids* **1990**, *116* (2), 140–144. https://doi.org/10.1016/0022-3093(90)90685-F.
(414) Jäger, C.; Feike, M.; Born, R.; Spiess, H. W. Direct Detection of Connectivities in Glasses by 2D NMR. *Journal of Non-Crystalline Solids* **1994**, *180* (1), 91–95. https://doi.org/10.1016/0022-3093(94)90402-2.
(415) Olsen, K. K.; Zwanziger, J. W.; Hartmann, P.; Jäger, C. Short and Intermediate Range Order in Glass: Nuclear Magnetic Resonance Probes of Site Connectivities and Distances. *Journal of Non-Crystalline Solids* **1997**, *222*, 199–205. https://doi.org/10.1016/S0022-3093(97)90114-9.
(416) Witter, R.; Hartmann, P.; Vogel, J.; Jäger, C. Measurements of Chain Length Distributions in Calcium Phosphate Glasses Using 2D ^{31}P Double Quantum NMR. *Solid state nuclear magnetic resonance* **1998**, *13* (3), 189–200.
(417) Feike, M.; Jäger, C.; Spiess, H. W. Connectivities of Coordination Polyhedra in Phosphate Glasses from ^{31}P Double-Quantum NMR Spectroscopy. *Journal of Non-Crystalline Solids* **1998**, *223* (3), 200–206. https://doi.org/10.1016/S0022-3093(97)00439-0.

(418) Glock, K.; Hirsch, O.; Rehak, P.; Thomas, B.; Jäger, C. Novel Opportunities for Studying the Short and Medium Range Order of Glasses by MAS NMR, ^{29}Si Double Quantum NMR and IR Spectroscopies. *Journal of Non-Crystalline Solids* **1998**, *232–234*, 113–118. https://doi.org/10.1016/S0022-3093(98)00380-9.
(419) Alam, T. M.; Tischendorf, B. C.; Brow, R. K. High-Speed ^{1}H MAS NMR Investigations of the Weathered Surface of a Phosphate Glass. *Solid state nuclear magnetic resonance* **2005**, *27* (1–2), 99–111. https://doi.org/10.1016/j.ssnmr.2004.08.006.
(420) Lo, A. Y. H.; Edén, M. Efficient Symmetry-Based Homonuclear Dipolar Recoupling of Quadrupolar Spins: Double-Quantum NMR Correlations in Amorphous Solids. *Physical chemistry chemical physics* **2008**, *10* (44), 6635–6644. https://doi.org/10.1039/b808295b.
(421) Stevensson, B.; Edén, M. Exotic Structural Motifs in Aluminosilicate Glasses Quantified by Solid-State NMR and Molecular Dynamics Simulations. *Journal of Non-Crystalline Solids* **2021**, *569*, 120389. https://doi.org/10.1016/j.jnoncrysol.2020.120389.
(422) Venkatachalam, S.; Schröder, C.; Wegner, S.; van Wüllen, L. The Structure of a Borosilicate and Phosphosilicate Glasses and Its Evolution at Temperatures above the Glass Transition Temperature: Lessons from in Situ MAS NMR. *Physics and Chemistry of Glasses - European Journal of Glass Science andTechnology Part B* **2014**, *55* (6), 280–287.
(423) Raguenet, B.; Tricot, G.; Silly, G.; Ribes, M.; Pradel, A. Revisiting the 'Mixed Glass Former Effect' in Ultra-Fast Quenched Borophosphate Glasses by Advanced 1D/2D Solid State NMR. *J. Mater. Chem.* **2011**, *21* (44), 17693–17704. https://doi.org/10.1039/C1JM12350E.
(424) Tricot, G.; Vezin, H. Description of the Intermediate Length Scale Structural Motifs in Sodium Vanado-Phosphate Glasses by Magnetic Resonance Spectroscopies. *J. Phys. Chem. C* **2013**, *11*, 1421–1427.
(425) Rawal, A.; Smith, B. J.; Athens, G. L.; Edwards, C. L.; Roberts, L.; Gupta, V.; Chmelka, B. F. Molecular Silicate and Aluminate Species in Anhydrous and Hydrated Cements. *J. Am. Chem. Soc.* **2010**, *132* (21), 7321–7337. https://doi.org/10.1021/ja908146m.
(426) Smith, B. J.; Rawal, A.; Funkhouser, G. P.; Roberts, L. R.; Gupta, V.; Israelachvili, J. N.; Chmelka, B. F. Origins of Saccharide-Dependent Hydration at Aluminate, Silicate, and Aluminosilicate Surfaces. *Proceedings of the National Academy of Sciences* **2011**, *108* (22), 8949–8954. https://doi.org/10.1073/pnas.1104526108.
(427) Pustovgar, E.; Sangodkar, R. P.; Andreev, A. S.; Palacios, M.; Chmelka, B. F.; Flatt, R. J.; d'Espinose de Lacaillerie, J.-B. Understanding Silicate Hydration from Quantitative Analyses of Hydrating Tricalcium Silicates. *Nat Commun* **2016**, *7* (1), 10952. https://doi.org/10.1038/ncomms10952.
(428) Kumar, A.; Walder, B. J.; Kunhi Mohamed, A.; Hofstetter, A.; Srinivasan, B.; Rossini, A. J.; Scrivener, K.; Emsley, L.; Bowen, P. The Atomic-Level Structure of Cementitious Calcium Silicate Hydrate. *J. Phys. Chem. C* **2017**, *121* (32), 17188–17196. https://doi.org/10.1021/acs.jpcc.7b02439.
(429) Kunhi Mohamed, A.; Moutzouri, P.; Berruyer, P.; Walder, B. J.; Siramanont, J.; Harris, M.; Negroni, M.; Galmarini, S. C.; Parker, S. C.; Scrivener, K. L.; Emsley, L.; Bowen, P. The Atomic-Level Structure of Cementitious Calcium Aluminate Silicate Hydrate. *J. Am. Chem. Soc.* **2020**, *142* (25), 11060–11071. https://doi.org/10.1021/jacs.0c02988.
(430) Hanrahan, M. P.; Men, L.; Rosales, B. A.; Vela, J.; Rossini, A. J. Sensitivity-Enhanced <sup>207</sub>Pb Solid-State NMR Spectroscopy for the Rapid, Non-Destructive Characterization of Organolead Halide Perovskites. *Chem. Mater.* **2018**, *30* (20), 7005–7015. https://doi.org/10.1021/acs.chemmater.8b01899.
(431) Askar, A. M.; Karmakar, A.; Bernard, G. M.; Ha, M.; Terskikh, V. V.; Wiltshire, B. D.; Patel, S.; Fleet, J.; Shankar, K.; Michaelis, V. K. Composition-Tunable Formamidinium Lead Mixed Halide Perovskites via Solvent-Free Mechanochemical Synthesis: Decoding the Pb Environments Using Solid-State NMR Spectroscopy. *J. Phys. Chem. Lett.* **2018**, *9* (10), 2671–2677. https://doi.org/10.1021/acs.jpclett.8b01084.

(432) Karmakar, A.; Askar, A. M.; Bernard, G. M.; Terskikh, V. V.; Ha, M.; Patel, S.; Shankar, K.; Michaelis, V. K. Mechanochemical Synthesis of Methylammonium Lead Mixed–Halide Perovskites: Unraveling the Solid-Solution Behavior Using Solid-State NMR. *Chem. Mater.* **2018**, *30* (7), 2309–2321. https://doi.org/10.1021/acs.chemmater.7b05209.
(433) Alharbi, E. A.; Alyamani, A. Y.; Kubicki, D. J.; Uhl, A. R.; Walder, B. J.; Alanazi, A. Q.; Luo, J.; Burgos-Caminal, A.; Albadri, A.; Albrithen, H.; Alotaibi, M. H.; Moser, J.-E.; Zakeeruddin, S. M.; Giordano, F.; Emsley, L.; Grätzel, M. Atomic-Level Passivation Mechanism of Ammonium Salts Enabling Highly Efficient Perovskite Solar Cells. *Nat Commun* **2019**, *10* (1), 3008. https://doi.org/10.1038/s41467-019-10985-5.
(434) Ruiz-Preciado, M. A.; Kubicki, D. J.; Hofstetter, A.; McGovern, L.; Futscher, M. H.; Ummadisingu, A.; Gershoni-Poranne, R.; Zakeeruddin, S. M.; Ehrler, B.; Emsley, L.; Milić, J. V.; Grätzel, M. Supramolecular Modulation of Hybrid Perovskite Solar Cells via Bifunctional Halogen Bonding Revealed by Two-Dimensional 19F Solid-State NMR Spectroscopy. *J. Am. Chem. Soc.* **2020**, *142* (3), 1645–1654. https://doi.org/10.1021/jacs.9b13701.
(435) Lee, J.; Lee, W.; Kang, K.; Lee, T.; Lee, S. K. Layer-by-Layer Structural Identification of 2D Ruddlesden–Popper Hybrid Lead Iodide Perovskites by Solid-State NMR Spectroscopy. *Chem. Mater.* **2021**, *33* (1), 370–377. https://doi.org/10.1021/acs.chemmater.0c04078.
(436) Grüninger, H.; Bokdam, M.; Leupold, N.; Tinnemans, P.; Moos, R.; De Wijs, G. A.; Panzer, F.; Kentgens, A. P. M. Microscopic (Dis)Order and Dynamics of Cations in Mixed FA/MA Lead Halide Perovskites. *J. Phys. Chem. C* **2021**, *125* (3), 1742–1753. https://doi.org/10.1021/acs.jpcc.0c10042.
(437) Gan, Z.; Hung, I.; Wang, X.; Paulino, J.; Wu, G.; Litvak, I. M.; Gor'kov, P. L.; Brey, W. W.; Lendi, P.; Schiano, J. L.; Bird, M. D.; Dixon, I. R.; Toth, J.; Boebinger, G. S.; Cross, T. A. NMR Spectroscopy up to 35.2T Using a Series-Connected Hybrid Magnet. *Journal of Magnetic Resonance* **2017**, *284* (Supplement C), 125–136. https://doi.org/10.1016/j.jmr.2017.08.007.
(438) Nimerovsky, E.; Movellan, K. T.; Zhang, X. C.; Forster, M. C.; Najbauer, E.; Xue, K.; Dervişoğlu, R.; Giller, K.; Griesinger, C.; Becker, S.; Andreas, L. B. Proton Detected Solid-State NMR of Membrane Proteins at 28 Tesla (1.2 GHz) and 100 KHz Magic-Angle Spinning. *Biomolecules* **2021**, *11* (5), 752. https://doi.org/10.3390/biom11050752.
(439) Hassan, A.; Quinn, C. M.; Struppe, J.; Sergeyev, I. V.; Zhang, C.; Guo, C.; Runge, B.; Theint, T.; Dao, H. H.; Jaroniec, C. P.; Berbon, M.; Lends, A.; Habenstein, B.; Loquet, A.; Kuemmerle, R.; Perrone, B.; Gronenborn, A. M.; Polenova, T. Sensitivity Boosts by the CPMAS CryoProbe for Challenging Biological Assemblies. *Journal of Magnetic Resonance* **2020**, *311*, 106680. https://doi.org/10.1016/j.jmr.2019.106680.
(440) Berruyer, P.; Björgvinsdóttir, S.; Bertarello, A.; Stevanato, G.; Rao, Y.; Karthikeyan, G.; Casano, G.; Ouari, O.; Lelli, M.; Reiter, C.; Engelke, F.; Emsley, L. Dynamic Nuclear Polarization Enhancement of 200 at 21.15 T Enabled by 65 KHz Magic Angle Spinning. *J. Phys. Chem. Lett.* **2020**, *11* (19), 8386–8391. https://doi.org/10.1021/acs.jpclett.0c02493.
(441) Yuan, E. C.-Y.; Huang, S.-J.; Huang, H.-C.; Sinkkonen, J.; Oss, A.; Org, M.-L.; Samoson, A.; Tai, H.-C.; Chan, J. C. C. Faster Magic Angle Spinning Reveals Cellulose Conformations in Woods. *Chem. Commun.* **2021**, *57* (34), 4110–4113. https://doi.org/10.1039/D1CC01149A.
(442) Xue, K.; Sarkar, R.; Tošner, Z.; Reif, B. Field and Magic Angle Spinning Frequency Dependence of Proton Resonances in Rotating Solids. *Progress in Nuclear Magnetic Resonance Spectroscopy* **2022**, *130–131*, 45–59. https://doi.org/10.1016/j.pnmrs.2022.04.001.

Glossary

Chemical shift anisotropy (CSA): for a solid, the shielding of the static magnetic field B_0 depends on its orientation because of the anisotropy of the electron density around the nuclei.

Central transition (CT): transition between energy levels, m_I = +1/2 and −1/2, with m_I the magnetic quantum number, of a half-integer spin quadrupolar nucleus.

Connectivity: path of covalent bonds between two nuclei.

Correlation NMR experiments: 2D NMR experiment based on coherence transfer and allowing the observation of connectivities or proximities between identical or distinct isotopes.

Cross-polarization (CP): transfer of magnetization between distinct isotopes by irradiating simultaneously the transitions of these isotopes with rf fields satisfying the Hartmann-Hahn condition.

Dipolar interaction: magnetic interaction between the magnetic dipole moment of two nuclei.

Dipolar recoupling: NMR technique, usually a sequence of rf pulses, which reintroduces the dipolar interaction under MAS conditions.

Dipolar truncation: attenuation of the coherence transfer between distant nuclei by the large interaction between nearby nuclei.

Dynamic nuclear polarization (DNP): transfer of magnetization from unpaired electrons to nuclei used to enhance the sensitivity of NMR experiments.

Magic-angle spinning (MAS): rotation of the sample at 54.736° with respect to the static magnetic field B_0, which averages out the anisotropic NMR interactions, such as CSA and dipolar interaction, and hence, improves the resolution and the sensitivity of NMR spectra.

Multiple-quantum magic-angle spinning (MQMAS): 2D NMR experiments, which refocuses the second-order quadrupolar broadening of half-integer spin quadrupolar nuclei by correlating their triple-quantum coherences with the single-quantum coherences of their CT.

Quadrupolar interaction: interaction between the electric quadrupole moment of a quadrupolar nucleus and the surrounding electric field gradient.

Quadrupolar nucleus: nucleus with a spin $I \geq 1$.

Rotary resonance recoupling (R^3): reintroduction of anisotropic NMR interaction when the nutation of the coherences is equal to an integer multiple of the MAS frequency.

Rotational resonance (R^2): reintroduction under MAS of the homonuclear dipolar interaction occurring when the difference in resonance frequencies between two nuclei is equal to an integer multiple of the MAS frequency.

Satellite transitions (ST): transition between energy levels, m_I and m_I +1, of a half-integer spin quadrupolar nucleus.

Nomenclature

γ: gyromagnetic ratio.

t_1: indirect evolution period of a 2D NMR experiment.

t_2: acquisition period of a 2D NMR experiment. The FID is detected during this period.

T_2': time constant for the decay of transverse magnetization, which is not refocused by a 180° pulse.

τ_R: rotor period.

ν_1: rf field amplitude in Hz.

ν_R: MAS frequency.

Further reading

1. Ahlawat, S.; Mote, K. R.; Lakomek, N.-A.; Agarwal, V. Solid-State NMR: Methods for Biological Solids. *Chem. Rev.* **2022**, *122* (10), 9643–9737. https://doi.org/10.1021/acs.chemrev.1c00852.
2. Bayzou, R.; Trébosc, J.; Hung, I.; Gan, Z.; Lafon, O.; Amoureux, J.-P. Indirect NMR Detection via Proton of Nuclei Subject to Large Anisotropic Interactions, Such as ^{14}N, ^{195}Pt, and ^{35}Cl, Using the T-HMQC Sequence. *J. Chem. Phys.* **2022**, *156* (6), 064202. https://doi.org/10.1063/5.0082700.
3. Cadars, S.; Sein, J.; Duma, L.; Lesage, A.; Pham, T. N.; Baltisberger, J. H.; Brown, S. P.; Emsley, L. The Refocused INADEQUATE MAS NMR Experiment in Multiple Spin-Systems: Interpreting Observed Correlation Peaks and Optimising Lineshapes. *Journal of magnetic resonance (San Diego, Calif. : 1997)* **2007**, *188* (1), 24–34. https://doi.org/10.1016/j.jmr.2007.05.016.
4. Edén, M. NMR Studies of Oxide-Based Glasses. *Annu. Rep. Prog. Chem., Sect. C: Phys. Chem.* **2012**, *108* (1), 177–221. https://doi.org/10.1039/C2PC90006H.
5. Edén, M. Recent Progress in Homonuclear Correlation Spectroscopy of Quadrupolar Nuclei. In *Modern Magnetic Resonance*; Webb, G. A., Ed.; Springer International Publishing: Cham, 2017; pp 1–33. https://doi.org/10.1007/978-3-319-28275-6_104-1.
6. Gómez, J. S.; Rankin, A. G. M.; Trébosc, J.; Pourpoint, F.; Tsutsumi, Y.; Nagashima, H.; Lafon, O.; Amoureux, J.-P. Improved NMR Transfer of Magnetization from Protons to Half-Integer Spin Quadrupolar Nuclei at Moderate and High Magic-Angle Spinning Frequencies. *Magnetic Resonance* **2021**, *2* (1), 447–464. https://doi.org/10.5194/mr-2-447-2021.
7. Grekov, D.; Vancompernolle, T.; Taoufik, M.; Delevoye, L.; Gauvin, R. M. Solid-State NMR of Quadrupolar Nuclei for Investigations into Supported Organometallic Catalysts: Scope and Frontiers. *Chem. Soc. Rev.* **2018**, *47* (8), 2572–2590. https://doi.org/10.1039/C7CS00682A.
8. Hanrahan, M. P.; Chen, Y.; Blome-Fernández, R.; Stein, J. L.; Pach, G. F.; Adamson, M. A. S.; Neale, N. R.; Cossairt, B. M.; Vela, J.; Rossini, A. J. Probing the Surface Structure of Semiconductor Nanoparticles by DNP SENS with Dielectric Support Materials. *J. Am. Chem. Soc.* **2019**, *141* (39), 15532–15546. https://doi.org/10.1021/jacs.9b05509.
9. Ishii, Y.; Tycko, R. Sensitivity Enhancement in Solid State ^{15}N NMR by Indirect Detection with High-Speed Magic Angle Spinning. *Journal of Magnetic Resonance* **2000**, *142* (1), 199–204. https://doi.org/10.1006/jmre.1999.1976.
10. Jaroniec, C. P.; Harris, R. K.; Wasylishen, R. E. Dipolar Recoupling: Heteronuclear. In *Encyclopedia of Magnetic Resonance*; John Wiley & Sons, Ltd: Chichester, 2009. https://doi.org/10.1002/9780470034590.emrstm1011.
11. Kobayashi, T.; Pruski, M. Spatial Distribution of Silica-Bound Catalytic Organic Functional Groups Can Now Be Revealed by Conventional and DNP-Enhanced Solid-State NMR Methods. *ACS Catal.* **2019**, *9* (8), 7238–7249. https://doi.org/10.1021/acscatal.9b02017.
12. Lesage, A. Indirect Coupling and Connectivity. In *Encyclopedia of Magnetic Resonance*; Harris, R. K., Wasylishen, R. E., Eds.; John Wiley & Sons, Ltd: Chichester, 2008. https://doi.org/10.1002/9780470034590.emrstm1012.
13. Levitt, M. H. Symmetry-Based Pulse Sequences in Magic-Angle Spinning Solid-State NMR Symmetry-Based Pulse Sequences in Magic-Angle Spinning Solid-State NMR. In *Encyclopedia of Nuclear Magnetic Resonance*; Harris, R. K., Wasylishen, R. E., Eds.; Wiley: Chichester, 2002; Vol. 9, pp 165–196.
14. Li, S.; Lafon, O.; Wang, W.; Wang, Q.; Wang, X.; Li, Y.; Xu, J.; Deng, F. Recent Advances of Solid-State NMR Spectroscopy for Microporous Materials. *Advanced Materials* **2020**, *32* (44), 2002879. https://doi.org/10.1002/adma.202002879.

15. Liang, L.; Ji, Y.; Chen, K.; Gao, P.; Zhao, Z.; Hou, G. Solid-State NMR Dipolar and Chemical Shift Anisotropy Recoupling Techniques for Structural and Dynamical Studies in Biological Systems. *Chem. Rev.* **2022**, *122* (10), 9880–9942. https://doi.org/10.1021/acs.chemrev.1c00779.
16. Lu, X.; Lafon, O.; Trébosc, J.; Tricot, G.; Delevoye, L.; Méar, F.; Montagne, L.; Amoureux, J. P. Observation of Proximities between Spin-1/2 and Quadrupolar Nuclei: Which Heteronuclear Dipolar Recoupling Method Is Preferable? *The Journal of chemical physics* **2012**, *137* (14), 144201. https://doi.org/10.1063/1.4753987.
17. Mafra, L.; Siegel, R.; Fernandez, C.; Schneider, D.; Aussenac, F.; Rocha, J. High-Resolution ^{1}H Homonuclear Dipolar Recoupling NMR Spectra of Biological Solids at MAS Rates up to 67 KHz. *Journal of magnetic resonance (San Diego, Calif. : 1997)* **2009**, *199* (1), 111–114. https://doi.org/10.1016/j.jmr.2009.04.004.
18. Martineau, C.; Bouchevreau, B.; Taulelle, F.; Trébosc, J.; Lafon, O.; Paul Amoureux, J. High-Resolution through-Space Correlations between Spin-1/2 and Half-Integer Quadrupolar Nuclei Using the MQ-D-R-INEPT NMR Experiment. *Physical Chemistry Chemical Physics* **2012**, *14*, 7112–7119. https://doi.org/10.1039/c2cp40344g.
19. Nagashima, H.; Martineau-Corcos, C.; Tricot, G.; Trébosc, J.; Pourpoint, F.; Amoureux, J.-P.; Lafon, O. Chapter Four - Recent Developments in NMR Studies of Aluminophosphates. In *Annual Reports on NMR Spectroscopy*; Webb, G. A., Ed.; Academic Press, 2018; Vol. 94, pp 113–185. https://doi.org/10.1016/bs.arnmr.2017.12.004.
20. Nagashima, H.; Trébosc, J.; Kon, Y.; Sato, K.; Lafon, O.; Amoureux, J.-P. Observation of Low-γ Quadrupolar Nuclei by Surface-Enhanced NMR Spectroscopy. *J. Am. Chem. Soc.* **2020**, *142* (24), 10659–10672. https://doi.org/10.1021/jacs.9b13838.
21. Nagashima, H.; Trébosc, J.; Kon, Y.; Lafon, O.; Amoureux, J.-P. Efficient Transfer of DNP-Enhanced ^{1}H Magnetization to Half-Integer Quadrupolar Nuclei in Solids at Moderate Spinning Rate. *Magnetic Resonance in Chemistry* **2021**, *59* (9–10), 920–939. https://doi.org/10.1002/mrc.5121.
22. Perras, F. A.; Kobayashi, T.; Pruski, M. Natural Abundance ^{17}O DNP Two-Dimensional and Surface-Enhanced NMR Spectroscopy. *J. Am. Chem. Soc.* **2015**, *137* (26), 8336–8339. https://doi.org/10.1021/jacs.5b03905.
23. Pourpoint, F.; Lafon, O.; Gauvin, R.; Amoureux, J.-P.; Delevoye, L. Chapter 4:Two-Dimensional Methods for Half-Integer Quadrupolar Nuclei. In *Modern Methods in Solid-state NMR*; 2018; pp 97–133. https://doi.org/10.1039/9781788010467-00097.
24. Qi, G.; Wang, Q.; Xu, J.; Deng, F. Solid-State NMR Studies of Internuclear Correlations for Characterizing Catalytic Materials. *Chem. Soc. Rev.* **2021**, *50* (15), 8382–8399. https://doi.org/10.1039/D0CS01130D.
25. Rankin, A. G. M.; Trébosc, J.; Paluch, P.; Lafon, O.; Amoureux, J.-P. Evaluation of Excitation Schemes for Indirect Detection of ^{14}N via Solid-State HMQC NMR Experiments. *Journal of Magnetic Resonance* **2019**, *303*, 28–41. https://doi.org/10.1016/j.jmr.2019.04.004.
26. Rankin, A. G. M.; Trébosc, J.; Pourpoint, F.; Amoureux, J.-P.; Lafon, O. Recent Developments in MAS DNP-NMR of Materials. *Solid State Nuclear Magnetic Resonance* **2019**, *101*, 116–143. https://doi.org/10.1016/j.ssnmr.2019.05.009.
27. Sakellariou, D.; Emsley, L. Through-Bond Experiments in Solids. In *Encyclopedia of Magnetic Resonance*; Harris, R. K., Wasylishen, R. E., Eds.; John Wiley & Sons, Ltd: Chichester, 2007. https://doi.org/10.1002/9780470034590.emrstm0566.
28. Sasaki, A.; Trébosc, J.; Amoureux, J.-P. Accelerating the Acquisition of High-Resolution Quadrupolar MQ/ST-HETCOR 2D Spectra under Fast MAS via ^{1}H Detection and through-Space Population Transfers. *Journal of Magnetic Resonance* **2021**, *333*, 107093. https://doi.org/10.1016/j.jmr.2021.107093.
29. Tycko, R.; Harris, R. K.; Wasylishen, R. E. Dipolar Recoupling: Homonuclear Experiments. In *Encyclopedia of Magnetic Resonance*; John Wiley & Sons, Ltd: Chichester, 2009. https://doi.org/10.1002/9780470034590.emrstm1070.

30. Venkatesh, A.; Hanrahan, M. P.; Rossini, A. J. Proton Detection of MAS Solid-State NMR Spectra of Half-Integer Quadrupolar Nuclei. *Solid State Nuclear Magnetic Resonance* **2017**, *84*, 171–181. https://doi.org/10.1016/j.ssnmr.2017.03.005.
31. Venkatesh, A.; Ryan, M. J.; Biswas, A.; Boteju, K. C.; Sadow, A. D.; Rossini, A. J. Enhancing the Sensitivity of Solid-State NMR Experiments with Very Low Gyromagnetic Ratio Nuclei with Fast Magic Angle Spinning and Proton Detection. *J. Phys. Chem. A* **2018**, *122* (25), 5635–5643. https://doi.org/10.1021/acs.jpca.8b05107.
32. Venkatesh, A.; Luan, X.; Perras, F. A.; Hung, I.; Huang, W.; Rossini, A. J. T_1-Noise Eliminated Dipolar Heteronuclear Multiple-Quantum Coherence Solid-State NMR Spectroscopy. *Phys. Chem. Chem. Phys.* **2020**, *22* (36), 20815–20828. https://doi.org/10.1039/D0CP03511D.
33. Venkatesh, A.; Lund, A.; Rochlitz, L.; Jabbour, R.; Gordon, C. P.; Menzildjian, G.; Viger-Gravel, J.; Berruyer, P.; Gajan, D.; Copéret, C.; Lesage, A.; Rossini, A. J. The Structure of Molecular and Surface Platinum Sites Determined by DNP-SENS and Fast MAS ^{195}Pt Solid-State NMR Spectroscopy. *J. Am. Chem. Soc.* **2020**, *142* (44), 18936–18945. https://doi.org/10.1021/jacs.0c09101.
34. Wang, W.; Xu, J.; Deng, F. Recent Advances in Solid-State NMR of Zeolite Catalysts. *National Science Review* **2022**, nwac155. https://doi.org/10.1093/nsr/nwac155.
35. Wiench, J. W.; Tricot, G.; Delevoye, L.; Trebosc, J.; Frye, J.; Montagne, L.; Amoureux, J.-P.; Pruski, M. SPAM-MQ-HETCOR: An Improved Method for Heteronuclear Correlation Spectroscopy between Quadrupolar and Spin-1/2 Nuclei in Solid-State NMR. *Phys. Chem. Chem. Phys.* **2006**, *8* (1), 144–150. https://doi.org/10.1039/B512246E.
36. Wiench, J. W.; Bronnimann, C. E.; Lin, V. S.-Y.; Pruski, M. Chemical Shift Correlation NMR Spectroscopy with Indirect Detection in Fast Rotating Solids: Studies of Organically Functionalized Mesoporous Silicas. *J. Am. Chem. Soc.* **2007**, *129* (40), 12076–12077. https://doi.org/10.1021/ja074746+.
37. Wiench, J. W.; Lin, V. S.-Y.; Pruski, M. ^{29}Si NMR in Solid State with CPMG Acquisition under MAS. *J Magn Reson* **2008**, *193* (2), 233–242. https://doi.org/10.1016/j.jmr.2008.05.007.
38. Zheng, M.; Xin, S.; Wang, Q.; Trébosc, J.; Xu, J.; Qi, G.; Feng, N.; Lafon, O.; Deng, F. Through-Space ^{11}B–^{27}Al Correlation: Influence of the Recoupling Channel. *Magnetic Resonance in Chemistry* **2021**, *59* (9–10), 1062–1076. https://doi.org/10.1002/mrc.5163.